Design, Analysis, and Testing of Nanoparticle-Infused Thin Film Sensors for Low Skin Friction Applications

Brian Robert Leslie

Dissertation submitted to the Faculty of the
Virginia Polytechnic Institute and State University
in partial fulfillment of the requirements for the degree of

Doctor of Philosophy
in
Aerospace Engineering

Joseph A. Schetz, Chair
Richard O. Claus
Michael K. Philen
Gary D. Seidel

November 2, 2012
Blacksburg, Virginia

Design, Analysis, and Testing of Nanoparticle-Infused Thin Film Sensors for Low Skin Friction Applications

Brian Robert Leslie

(ABSTRACT)

Accurate measurement of skin friction in complex flows is important for: documentation and monitoring of fluid system performance, input information for flow control, development of turbulence models and CFD validation. The goal of this study was to explore using new materials to directly measure skin friction in a more convenient way than available devices. Conventional direct measurement skin friction sensors currently in use are intrusive, requiring movable surface elements with gaps surrounding that surface, or require optical access for measurements. Conventional direct measurement sensors are also difficult to apply in low shear environments, in the 1-10 Pa range. A new thin, flexible, nanoparticle infused, piezoresistive material called Metal Rubber$^{\text{TM}}$ was used to create sensors that can be applied to any surface. This was accomplished by using modern computerized finite element model multiphysics simulations of the material response to surface shear loads, in order to design a sensor configuration with a reduced footprint, minimal cross influence and increased sensitivity. These sensors were then built, calibrated in a fully-developed water channel flow and tested in both the NASA 20x28 inch Shear Flow Control Tunnel and a backwards facing step water flow. The results from these tests showed accurate responses, with no amplification to the sensor output, to shear levels in the range of 1-15 Pa. In addition, the computer model of these sensors was found to be useful for studying and developing refined sensor designs and for documenting sources of measurement uncertainty. These encouraging results demonstrate the potential of this material for skin friction sensor applications.

Acknowledgements

Contents

List of Figures

List of Tables

Chapter 1

Introduction

Drag is the retarding force of a fluid on a body parallel and opposite to the bodys relative motion. When designing or characterizing a vehicle that moves through any fluid, one of the most important features to determine is the drag on the body. Knowing the drag can help determine the amount of power required to move the vehicle and how fast the vehicle can travel, among other things. The drag force on a body can be defined as:

$$F_D = \frac{1}{2}\rho U^2 C_D A \tag{1.1}$$

where ρ is the density of the fluid, U is the velocity, C_D is the drag coefficient, and A is the reference area of the body[12]. There are a number of components that can contribute to the overall drag coefficient, including skin friction drag, pressure drag, and wave drag. Pressure drag is caused by pressure differences in the stream wise direction. Wave drag is caused by any shock waves that have formed on the body. Skin friction drag is due to the interaction of the fluid with the surface of the body. This interaction occurs in the viscous area very near to the body surface, called the boundary layer. The drag due to skin friction is often represented using the skin friction coefficient:

$$C_f \equiv \frac{\tau_w}{\frac{1}{2}\rho_e U_e^2} \tag{1.2}$$

where τ_w is the shear stress on the body surface and the subscript e indicates the value at the edge of the boundary layer[13]. In most situations it is assumed that at the surface of the body, the fluid velocity is zero. This assumption is called the no-slip condition. With this condition and continuum flow, the shear stress intensity at the wall can be found to be:

$$\tau_w = \mu \frac{\partial U}{\partial n}\big|_w \tag{1.3}$$

where μ is the dynamic viscosity of the fluid, and $\frac{\partial U}{\partial n}$ is the velocity gradient normal to the body surface[13]. Equation 1.3 is valid for both laminar and turbulent flows, due to the

1

laminar sublayer being present very near the wall in turbulent flows.

1.1   Measuring Skin Friction

Since skin friction is so important, there is a long history of attempts at accurate measurement. A number of review articles chronicling these efforts are available, including those by Nitsche[2], Winter[3], Schetz [14], and Naughton[15]. Skin Friction sensors were first invented by British Engineer William Froude in 1872[1]. Froude developed his law of skin friction similarity by towing streamlined catamaran planks through water at a variety of speeds. By varying the speed, length of the planks and the quality of the plank surface, Froude was able to systematically evaluate the effects of skin friction. The apparatus employed in this study is shown in Figure 1.1 and was used in an attempt to estimate the performance of ships. Since 1872 a number of methods have been developed in order to measure skin fric-
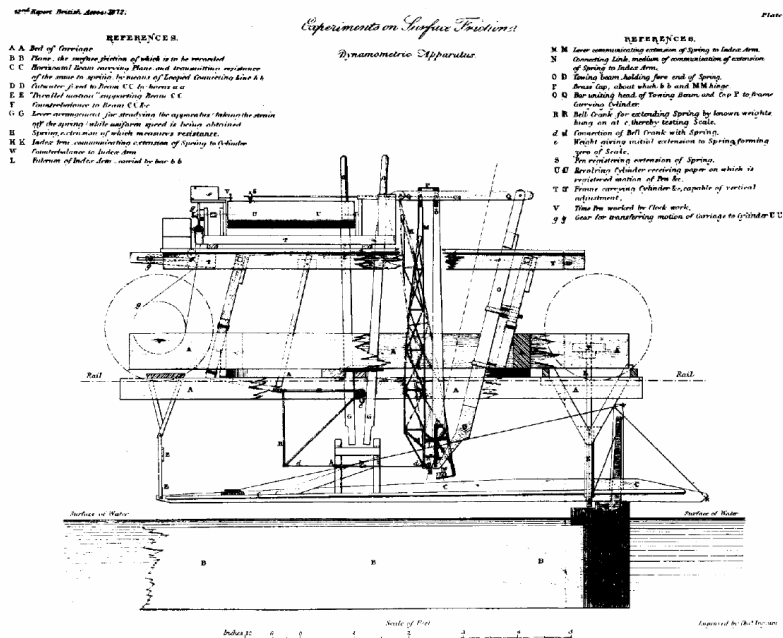
Figure 1.1: Skin Friction Measurement Apparatus from Froude[1]

tion. There are three types of methods used to measure skin friction, direct, semi-direct, and indirect. Direct methods measure the force exerted on a flat portion of the sensor that is exposed to the flow. Semi-direct methods will directly measure the shear stress, but are limited to certain flow conditions. Indirect methods require knowledge of some properties of the flow prior to running the experiment. The measured values are then related to the wall shear stress through analytical functions.

1.1.1 Indirect Methods

Indirect methods rely on the user having prior knowledge or assuming some flow conditions. Nitsche[2] compiled a list of the more popular indirect methods, shown in Figure 1.2. These methods are most effective when the flow is steady, two-dimensional, and incompressible. Such methods begin to fail when the flow is difficult to define, including flows with unsteadiness, compressibility, transition, separation, three-dimensionality, and temperature variations. Surface hot-film and hot-wire sensors, shown in Figure 1.2a, utilize heat transfer
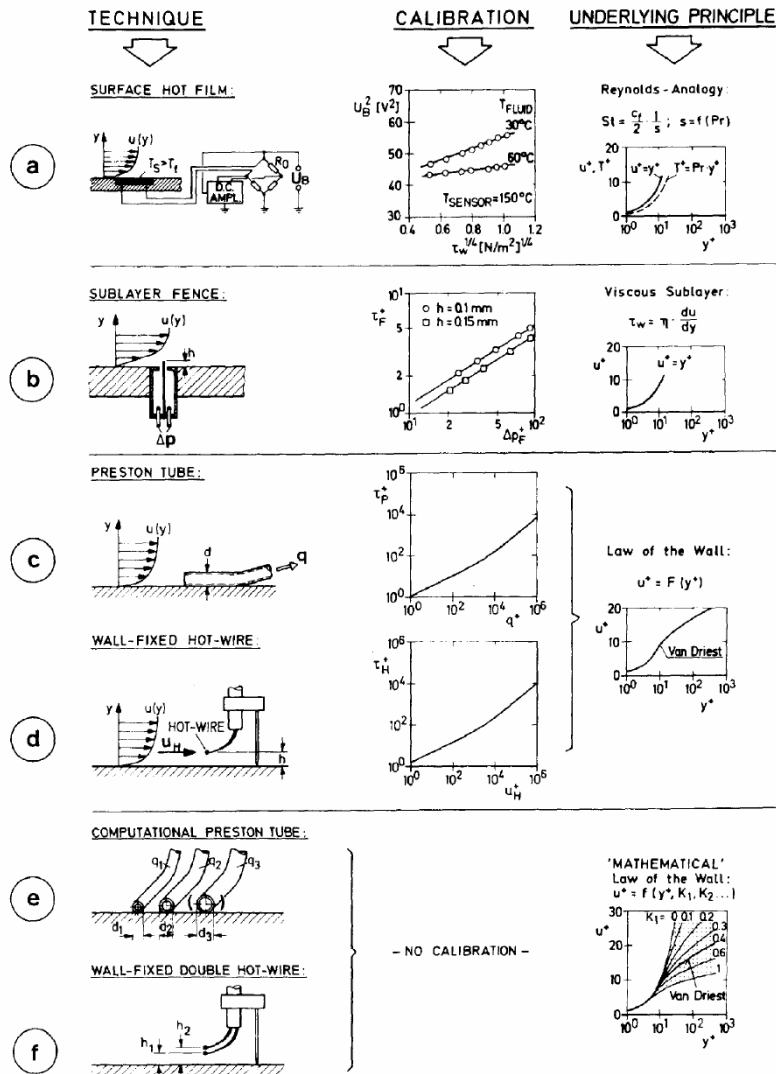
Figure 1.2: Compilation of Indirect Methods Including Calibration Procedures and Underlying Principles, Nitsche[2]

measurements to determine skin friction. This is done by utilizing Reynolds Analogy to

relate the heat transfer to skin friction. This analogy is given in Equation 1.4.

$$St * Pr^{\frac{2}{3}} = \frac{C_f}{2}$$ (1.4)

where St is the Stanton number, and Pr is the Prandtl number. Hot-wire sensors work by utilizing a very thin metal wire that is heated above the flow temperature. The wire will cool as the flow passes over it through convection. The measurement device can work in one of three ways, by keeping the current through the wire, voltage through the wire, or temperature of the wire constant and measuring the voltage change due to the flow. Hot-wire and hot-film methods are very sensitive to temperature variations, do not provide directionality, and lack precision when calculating skin friction. When used in well-known flow fields, these sensors are capable of uncertainties of around $\pm 5\%$.

Two techniques that utilize a small obstacle in the viscous sublayer include the sublayer fence and Stanton tube methods. The sublayer fence method, seen in Figure 1.2b and introduced by Konstantinov[16], uses a small vertical strip protruding into the laminar sublayer. The pressure difference in front and behind the strip is measured, and that can be related to the shear stress. The sensitivities of the sublayer fence and devices that work similarly to the sublayer fence, including the Preston tube, submerged step, razor blade, square ridge, forward step, and the block with a cut-out, are shown in Figure 1.3. These methods work
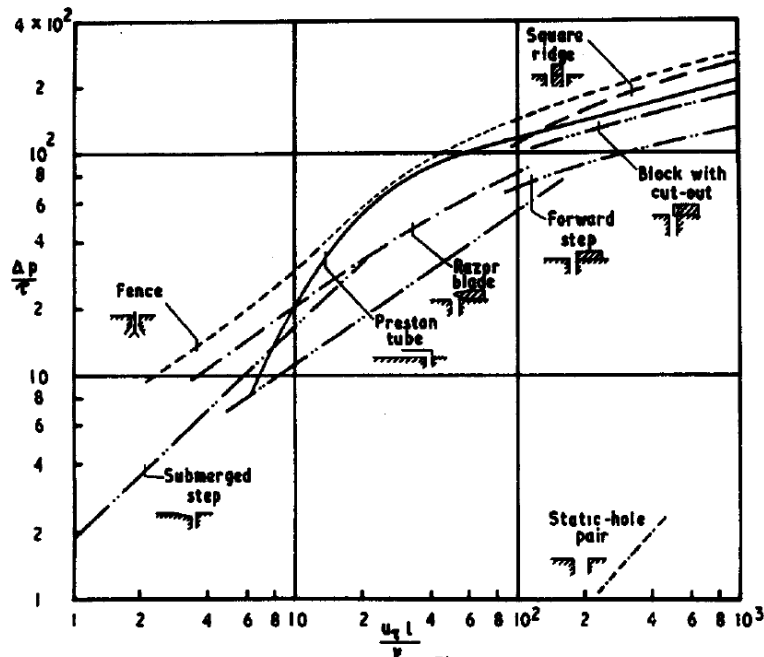
Figure 1.3: Sensitivities of Various Obstacles as Skin-Friction Meters, Winter[3]

well even in strong pressure gradients, and their small size allows them to work in compressible flows since they only protrude into the laminar sublayer. Due to the small size of the

components, they are hard to geometrically define and calibrate. These methods are also difficult to extend to three-dimensional flows.

The last indirect skin friction measurement method relies on velocity profile measurements in turbulent flows to determine skin friction, seen in Figure 1.2c-f. Clauser[17] asserted that most turbulent velocity profiles follow the law of the wall, as shown in Figure 1.4. The law of the wall refers specifically to the logarithmic region of the velocity profile, which can be seen in Figure 1.4. The wall shear stress can be determined by fitting the velocity profile to this law of the wall, which is scaled on the friction velocity u_τ and is defined as:

$$u_\tau \equiv \sqrt{\frac{\tau_w}{\rho}} \tag{1.5}$$

The logarithmic region is used, because usually the viscous sublayer is too thin for an accurate velocity profile to be measured. This method cannot be extended to three-dimensional flows. However, the shear force can be determined with the laminar sublayer using Equation 1.3, which can be used to extend a few of these methods to three dimensional flows. There are a number of ways to measure this velocity profile, including the Preston tube, hot-wire anemometry, and Laser Doppler Velocimetry (LDV)[18]. LDV measurements are usually the most accurate due to the small size of the measurement volume and the unobtrusive nature of the measurements, as long as the seeding particles are not significantly large. LDV methods can produce very low uncertainty results, on the order of less than $\pm 5\%$. LDV methods are the exception to the indirect measurement methods, in that they can be used in almost any flow and are not sensitive to pressure or temperature changes in the flow. The major problem associated with LDV measurements is the high cost of equipment needed for these measurements. Extending this method to three-dimensional flows requires even more complexity and cost.

1.1.2   Semi-Direct Methods

The two most common semi-direct skin friction measurement methods are Oil Film Interferometry, also called Laser Interferometer Skin Friction (LISF), and shear sensitive liquid crystals. Both of these methods require optical access and can only be used with gaseous fluids and in low-enthalpy flows. They do, however, provide good spatial resolutions, are non-intrusive to the flow, and can be applied to three-dimensional flows. LISF, developed by Tanner and Blows[19], utilizes lasers to determine the thickness of an oil film on the surface of a polished test surface. One laser component will reflect off the oil surface and the second will reflect off the test surface; fringe patterns from the reflected lasers are then used to determine the time rate of thinning of the oil on the test surface. The time rate of thinning of oil can be directly related to the shear stress on the test surface. Since the thinning of the oil is dependent on the viscosity of the oil, this measurement method is very sensitive to temperature variations. This method also assumes that there is no pressure gradient over
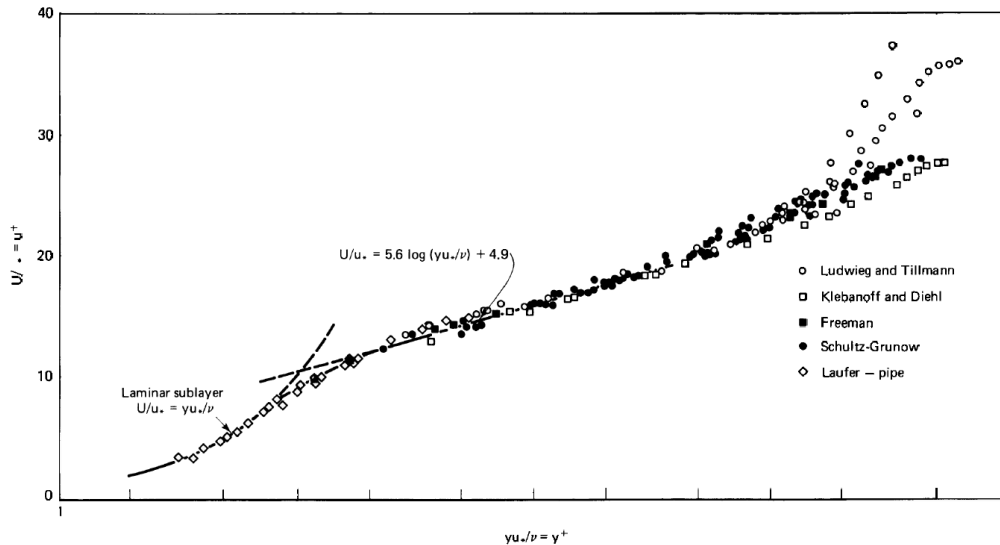
Figure 1.4: Universal Law of the Wall Plot for Turbulent Boundary Layers, Schetz[4]

the surface. While this method gives good spatial resolution, the accuracy of the results are hampered due to the large number of factors involved with the thinning of the oil. Studies have shown that the uncertainty in the rate of thinning of the oil film is around $\pm 10\%$, which will produce a higher uncertainty in skin friction.

Skin friction sensitive liquid crystals were first developed by Klein and Margozzi[20]. This method utilizes the highly optically active nature of the crystals. When arranged correctly on a surface and illuminated by an unpolarized white light, a three dimensional color spectrum can be captured. Through careful calibration, this color spectrum can be converted into a shear stress pattern on the test surface. This method requires a number of cameras at different angles to capture the light reflected off the liquid crystals and is very sensitive to temperature and pressure gradients. This makes the liquid crystal method very hard to calibrate accurately. Due to the difficulty in calibrating the liquid crystals, it has been used primarily as a tool for determining skin friction contours. The liquid crystals will also solidify over the course of a day, which removes their light scattering ability. Despite these downfalls, liquid crystals can produce a very detailed map of shear stress on a surface with no prior knowledge of the flow orientation.

1.1.3   Direct Methods

There are two types of direct skin friction measurement methods. The first is the nulling direct measurement method. This utilizes a small moveable plate in the wall, which is attached

to a restoring force mechanism that counteracts the shear force over the top of the small plate, keeping it stationary. Since the small plate does not move, the gaps required around the plate can be very small and there are no effects due to tilt of the plate. This method was first used by Dhawan[21], for which the setup can be seen in Figure 1.5a. While this method works very well in measuring total skin friction over a flat plate, it has a few disadvantages. Frequency response is hampered due to the feedback loop, the entire assembly is large and complicated, setting up and calibrating the sensor can be expensive, and it is hard to apply to three-dimensional flows. This type of sensor is mainly viable for incompressible or low-enthalpy compressible flows, and can produce measurements with uncertainties on the order of ± 5-10%.

The second type of direct skin friction measurement method is the non-nulling version of the movable plate method. Most non-nulling direct methods utilize a beam that is deflected due to the shear forces on the end of the beam, an example is shown in Figure 1.5b. A gap be-

(a) Nulling Plate Direct-Measurement, Dhawan[21]

(b) Beam Deflection Direct-Measurement, Schetz[13]
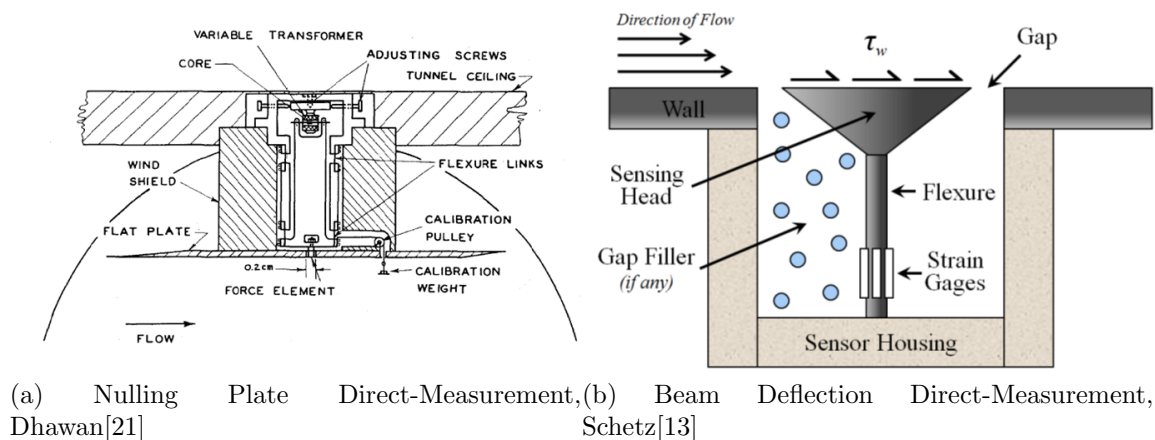
Figure 1.5: Direct Skin Friction Measurement Techniques

tween the beam and the surrounding wall allows the beam to deflect slightly. The deflection of the beam can be measured by using strain gages or optical methods. The presence of this gap and the deflection of the floating head can lead to increased uncertainties in the results due to slight interference with the flow, as shown by Allen[22]. Many variations of this type of sensor exist, including sensors with filler in the gap, a rubber sheet across the top surface covering the beam and gap, or sensors utilizing a bellows to isolate the strain gages for use in hot-flow environments. Filling or covering can lead to other problems, including loss in response time, decreased sensor response, and increased manufacturing difficulty. Provided that the beam deflection is very small, this method does not interfere with the flow and can be used to accurately determine skin friction, including directionality. Such devices have been successfully used in both three-dimensional and high-enthalpy, high-speed flows. However, these sensors can be prone to misalignment during calibration and flow testing.

Overall the uncertainties with this method can be fairly low, on the order of $\pm$5-10%, if proper calibration and alignment procedures are used.

1.2 Recent Methods

Most of the methods discussed to this point have been around for a relatively long time. Newer methods have been created which take advantage of new material development technology. One of these methods uses the deflection of micro pillars, with a height in the range of $y^+ = 5$, on a surface to determine shear[5]. Where y^+ is defined as:

$$y^+ \equiv \frac{y u_*}{\nu} \tag{1.6}$$

where y is the normal distance from the wall, $u_* \equiv \sqrt{\frac{\tau_w}{\rho}}$ is the friction velocity, and ν is the fluid kinematic viscosity. This method can produce skin friction measurements resolved in both space and time and can be used for directionality. A few problems exist with this method, the first being the need for optical access directly above the pillars in order to measure the displacement of each pillar. The second issue with this method is the difficulty of manufacturing, calibrating, and maintaining the integrity of the micro pillars. Each individual pillar must be calibrated in order to produce accurate results, due to non-uniformities in each pillar's flexural stiffness. A sample measurement from this type of sensor is shown in Figure 1.6.
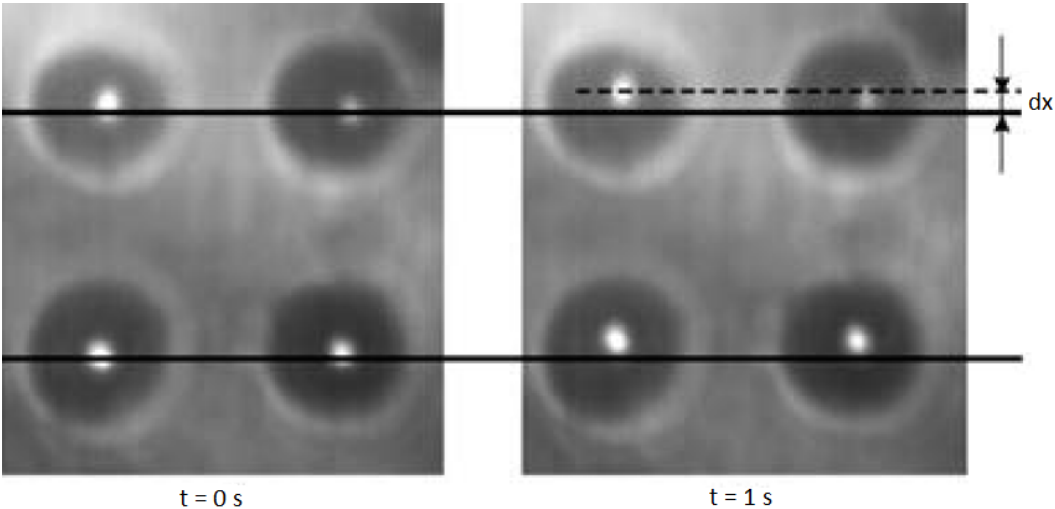
Figure 1.6: Sample Micro Pillar Measurement Images, Brucker[5]

Another newer method for measuring skin friction uses the deformation of a thin film polymer, as shown in Figure 1.7. An example of this method was used by Omid and Soria [6]. A

fluorescent molecule is dissolved into the thin film and used as a marker for optical tracking of the film. The tangential deformation is measured using a method similar to Particle Image Velocimetry (PIV)[23], where multiple images are taken and compared to determine the displacement of the florescent markers. This method also allows for tracking of the normal deformation of the thin film. The intensity of the florescence is proportional to the height of the thin film to the camera. This method works well for point measurements on any model, since the film is flexible and can be used to measure tangential and normal forces. The main problem associated with this type of design is the need for optical access in order to determine the deflection of the thin film.
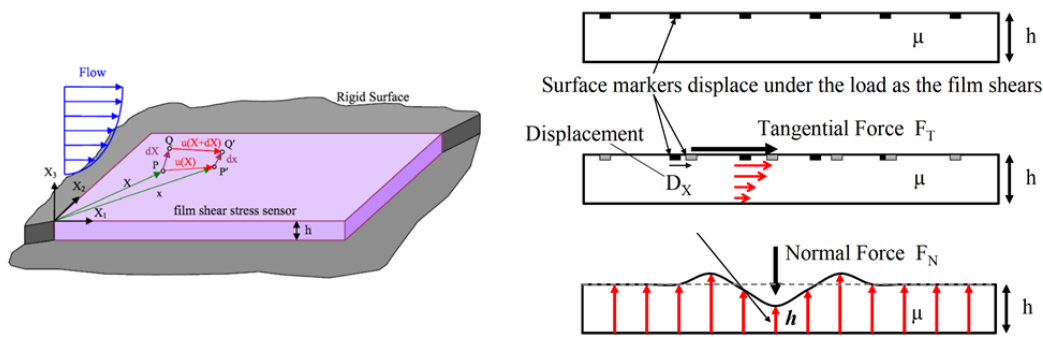
Figure 1.7: Thin Film Shear Stress Sensor, Omid[6]

1.3   Skin Friction Measurement Devices Overview

It can be seen from the comparisons in Table 1.1 that the current methods available have features that can be improved in order to provide a higher performance measurement system. Indirect measurement methods require knowledge of the flow conditions in order to determine skin friction. Most of these methods are intrusive to the flow. In the case of Laser Doppler Velocimetry, which is a very viable method for measuring skin friction, initial costs to set up can be high and optical access is needed. Semi-direct measurement methods are somewhat limited in terms of quantitative data, even though they have good spatial resolution. Both of the semi-direct measurement methods also require optical access. Out of the direct measurement methods, the non-nulling measurement method is the most viable. This method, however, has a few attributes that could be improved. The first is the size of these sensors, needing a large area beneath the surface for the deflecting beam and associated strain gages. This type of design is complicated, can be costly to build, and can be fragile. Most such sensors also utilize gaps around the floating element which can be prone to fouling. In addition, these sensors usually require a flat measurement surface, which is not always available in application. The more advanced methods forgo the need for this gap, but return to needing optical access in order to determine the displacement of the

sensor material. All of these methods are severely limited for wall shears on the order of 1 Pa.

A sensor is needed that is small, so it can fit in tight spaces; flexible, so it can conform to curved surfaces; and has a significant electrical response to shear, so measurements in the low skin friction regime can be made without requiring optical access or knowledge of the flow. This study aims to consider development of such a sensor employing a recently developed nano-particle infused material that fits this need. The research described here was a closely coordinated team effort between Virginia Tech and the material developer.

Table 1.1: Skin Friction Method Comparison

Measurement Technique		Advantages	Disadvantages
Direct Measurements			
Nulling Movable Wall Element		• Flow and fluid independent • Able to determine direction • Non-intrusive	• Small Force • High cost • Low Frequency Response • Complex and cumbersome in size
Non-Nulling Movable Wall Element		• Flow and fluid independent • Able to determine direction • Non-intrusive • High frequency response	• Small Force • High cost • Subject to misalignment
Semi-Direct Measurements			
Oil Film Interferometry		• Flow and fluid independent • Able to determine direction • Non-intrusive	• Temperature sensitive • Shear stress, shear gradient, time limited • Requires optical access
Liquid Crystals		• Flow and fluid independent • Able to determine direction • Non-intrusive	• Temperature and pressure sensitive • Requires optical access • Low sensitivity • Limited time window • Shear stress limited
Indirect Measurements			
Analogy	**Heat Transfer (Reynolds Analogy)**	• Dual purpose sensor • Low cost • High frequency response	• Low precision measurement • Not able to determine direction • Limited temperature range with high temperature sensitivity • Requires knowledge of the free stream
	Mass Transfer	• Low cost	• Calibration not available • Low precision measurement • Not able to determine direction • Limited temperature range with high temperature sensitivity • Requires knowledge of the free stream
Flow About Obstacles		• Simple • Low cost	• Calibration difficult • Subject to misalignment • Assumes law of the wall • Requires knowledge of the boundary layer conditions
Profile Measurement	**Preston Tube**	• Simple • Low cost	• Flow calibration required • Subject to misalignment • Assumes law of the wall • Boundary layer thickness limited • Requires knowledge of the boundary layer conditions
	Stanton Tube	• Simple • Low cost	• Subject to misalignment • Assumes law of the wall • Requires knowledge of the boundary layer conditions
	Hot-wire	• Simple • High frequency response	• Assumes law of the wall • Fragile and temperature limited • Requires knowledge of fluid viscosity
	Laser Doppler Anemometry	• Non-intrusive • High frequency response	• Requires optical access • Requires seed particles • Requires knowledge of fluid viscosity

Chapter 2

Sensor Material Description

The specific nanoparticle infused polymer material considered here for application to skin friction sensors is Metal Rubber$^{\text{TM}}$[24], a rubbery compound created by Nanosonic, Inc located in Pearisburg, VA. The Metal Rubber material exhibits the properties of rubber, but can be manufactured to have the conductivity of a metal. Metal Rubber describes an array of materials that can be made using the same process. The material is formed using a layer-by-layer self-assembly method, shown in Figure 2.1a. These layers can be arranged in various ways, as shown in Figure 2.1b, to give the material different properties. With changes to

(a) Self Assembly Process   (b) Layer Arrangements
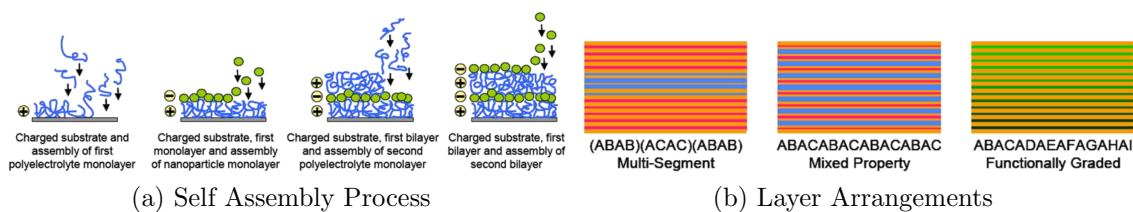
Figure 2.1: Metal Rubber Polymer Assembly

(a) UnPatterned   (b) Patterned
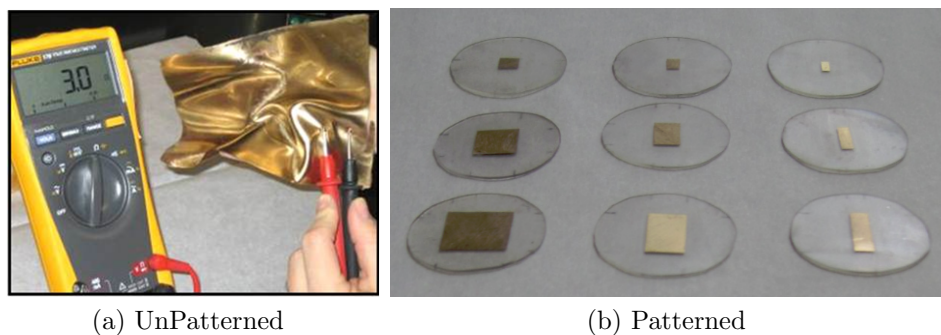
Figure 2.2: Metal Rubber Polymer Example

12

the chemical concentrations and the process during assembly the elastic modulus and the conductivity properties, in addition to several other properties, of the Metal Rubber can be modified. For the material used for skin friction sensors, nanoparticle gold is included in the manufacturing process and is functionally graded into one side of the polymer. This makes the material conductive, as seen in Figure 2.2a, and piezoresistive. In addition to this, the conductive area can be patterned to any shape as seen in Figure 2.2b, within certain size restrictions. Specific variations of Metal Rubber can be reproduced accurately, which is very important considering the innumerable variations of Metal Rubber that can be created.

This material is very useful in skin friction sensors for a number of reasons. Its flexible nature allows sensors to conform over curved bodies. The ability to pattern the conductive area allows for creative sensor designs. The piezoresistive nature of the conductive area can be used to determine the strain and, thus, the shear on the sensor, without the use of optical devices. The material is very thin, at only 0.5 mm in thickness, taking up much less room compared to other direct measurement skin friction devices.

2.1   Mechanical Properties

The specific material used for the skin friction sensors has changed slightly as knowledge of the properties needed for the optimum sensor became clear, but the overall make-up remains the same. In order to obtain the material properties, the material was tested in the Texture Technologies Corp universal testing machine TA.XTplus[25], shown in Figure 2.3. The TA.XTplus is capable of calibrated tensile testing of sensor material at loading rates of 0.01 - 40 $\frac{mm}{s}$. The load frame can be programmed for specialized cyclic testing at user-defined strain, cycles, load rates, and temperatures (if the thermal cabinet is attached). The TA.XTplus load frame is capable of controlled movements as small as 0.001 mm, which is sufficiently small for the levels of strain the sensor material is expected to experience for this application. A sample stress-strain curve for the specific Metal Rubber used here is shown in Figure 2.4.

Due to the strain magnitude on the sensors being very low, which will be analyzed in a subsequent section, only the linear elastic region of the stress-strain graph is needed to determine the properties relevant to the sensors. A Young's modulus of 2.0 MPa was determined by taking the slope of this linear region. Nanosonic, Inc. also determined the material has a Poisson's ratio of 0.45 from strain measurements perpendicular to the strain in Figure 2.4.

Figure 2.3: TA.XTplus Bench Top Load Frame (Thermal Cabinet not Shown)
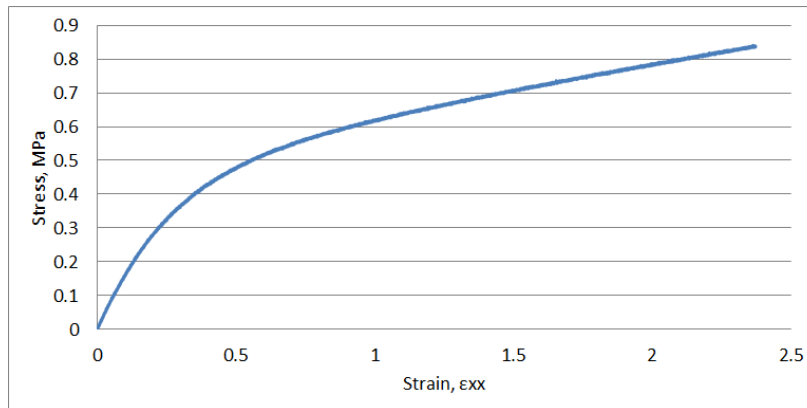
Figure 2.4: Metal Rubber Stress vs. Strain Curve

2.2 Electrical Properties

The most attractive aspect of Metal Rubber for use in sensors are its electrical properties. Not only is this variation of Metal Rubber conductive, but it is also piezoresistive. Piezoresistivity is the changing of a material's electrical resistivity when a mechanical load is applied[26]. This allows the user to directly measure the strains experienced by the sensor. Piezoresistivity is quantified using a piezoresistivity matrix. The piezoresistivity matrix relates either the stress or strain to the resistivity of the material; the strain version is shown in Equation 2.1:

$$\rho_{ij} = \rho_0 + m_{ij}\epsilon_{ij}\rho_0 \tag{2.1}$$

where ρ_0 is the unloaded resistivity, m_{ij} is the piezoresistivity matrix and ϵ_{ij} is the strain tensor. The strain version of this equation is used, since it is easier to determine the strain piezoresistive coefficients and this form can take into account strains due to temperature effects. For Metal Rubber, a few assumptions can be made in order to simplify this relationship. The main assumption is that there is no conduction through the thickness of the

material. This is due to the conductive area on a sheet of Metal Rubber being only $300nm$ thick on one side of the sheet, in addition to being graded through that $300nm$ thickness. This means that the through-thickness conduction is negligible compared to the conduction in the other directions. When this assumption is applied to the piezoresistivity matrix, any coefficient related to the conduction through the thickness becomes negligible. The second assumption that can be made is isotropy in the two remaining directions, the X and Y directions if the Z direction is through the thickness. This assumption can be made, because the material is homogeneous in the X and Y directions. This reduces the amount of testing needed to determine the piezoresistive coefficients. It was determined that four unique tests would provide all of the information needed in the piezoresistive matrix. These tests are shown in Figure 2.5. The first two tests are simply tensile tests, using an ASTM D638
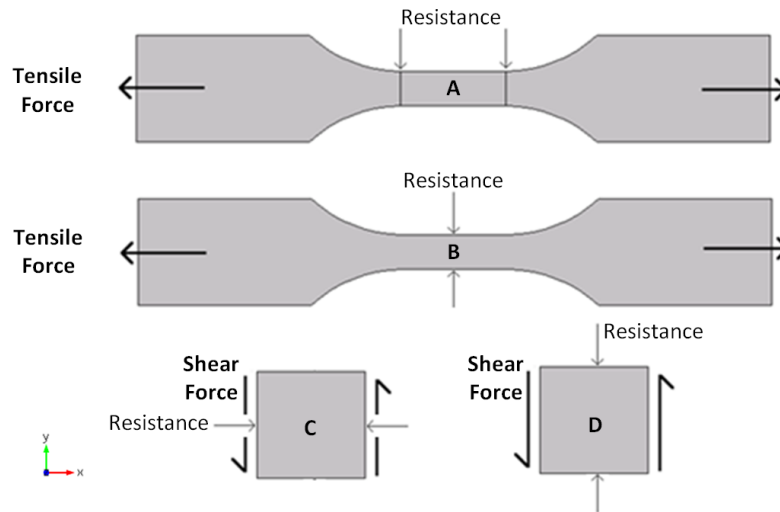
Figure 2.5: Piezoresistive Strain Matrix Tests A) X-Resistance Tensile Test B) Y-Resistance Tensile Test C) X-Resistance Shear Test D) Y-Resistance Shear Test

dogbone shape. The first test, Figure 2.5A, measures the resistance of the material parallel to the applied load on the sensor. The second repeats the same test, but with the resistance measured perpendicular to the applied load, shown in Figure 2.5B. The results from these two tests are shown in Figure 2.6, where the X-resistance test is plotted against the strain in the X direction and the Y-resistance test is plotted against the strain in the X direction. It can be seen from Figure 2.6 that there are slight non-linearities in the materials response. It can also be seen that the Y-resistance test has more noise than the X-resistance test. This is due to both the smaller magnitude of the strains in the Y-direction and the distance between the leads being smaller in this test.

Another test is needed to determine if the material reacts the same in compression as it does in tension. Unfortunately, this cannot be completed by using the same dogbone samples, just

(a) X-Resistance Tensile Test   (b) Y-Resistance Tensile Test
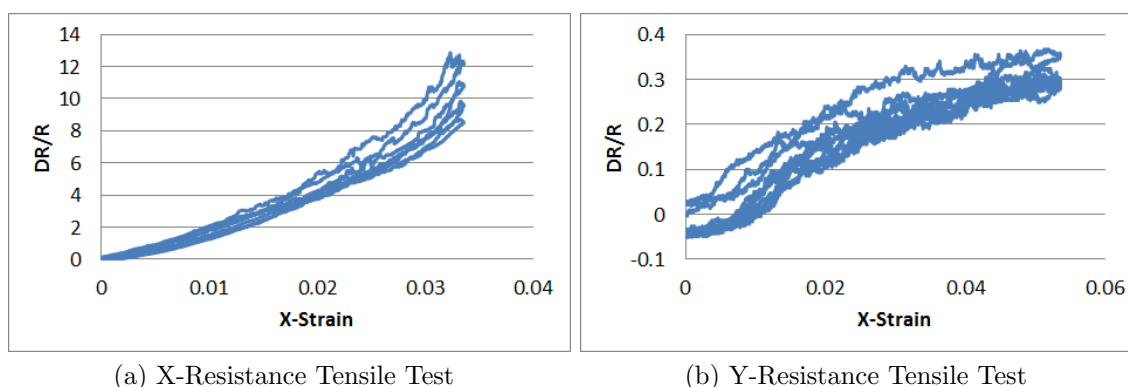
Figure 2.6: Resistance-Tensile Testing Results

in compression. Since the material is thin, a stiff backing is needed to prevent the samples from buckling. A hard rubber backing, cut to the same shape and with the same Poisson's ratio as Metal Rubber, is added to the back of the Metal Rubber dogbone. Since only the Poisson's ratios match, and not the Young's modulus, the stress data from these tests are not valid. The strain on the Metal Rubber, however, will match the strain on the entire assembly. This allows the resistance-strain relationship to be measured under compression. Figure 2.7 shows the compression test results along with the previous tensile test results.
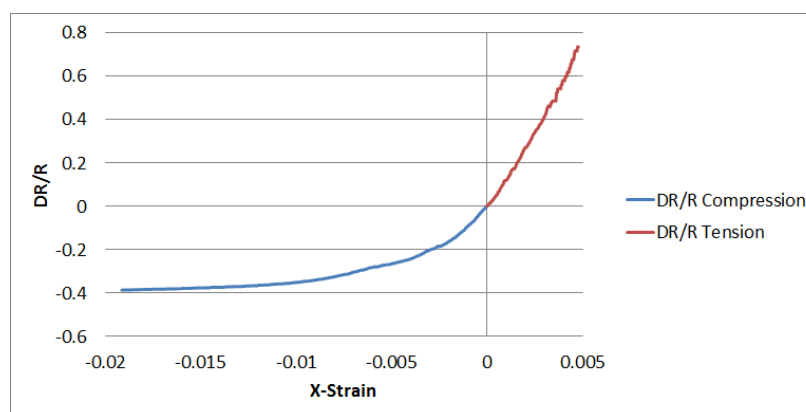
Figure 2.7: Compression Test Data Added to the Tensile Test Data

There is a smooth transition from the tensile results through zero to the compression results. Unlike in tension, the change in resistance in the compression test approaches a limit. This is due to the spacing between gold particles reaching a point where additional compression will not increase conductivity between the particles. Fortunately, this should not play a part in the response of the sensors to be considered here. It will be shown later that the magnitude of strain on the sensors is on the order of 10^{-4}, well below this nonlinear behavior. In order

to determine how the sensors respond, only data on the order of the strain on the sensor is used. At this level, the data can be approximated using a linear least-square best-fit line. Figure 2.8 shows the results of this analysis.

(a) X-Resistance Tensile Test   (b) Y-Resistance Tensile Test
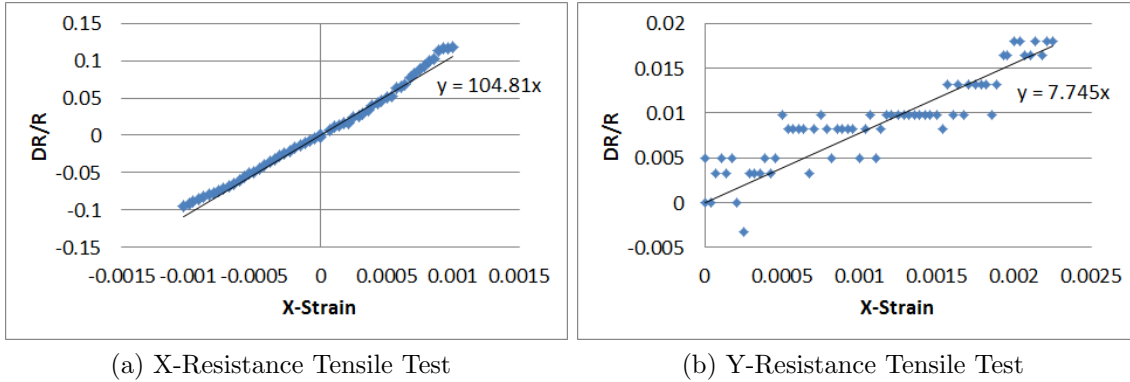
Figure 2.8: Tensile Testing Results

These two material tests are then used to determine the m_{11}, m_{12}, m_{21}, and m_{22} piezoresistivity coefficients. Using the slope of a root-mean-square fit line through these results and a modified form of Equation 2.1 results in the set of equations:

$$m_{11}\epsilon_x + m_{12}\epsilon_y = 104.81 \tag{2.2a}$$

$$m_{21}\epsilon_x + m_{22}\epsilon_y = 7.745 \tag{2.2b}$$

$$\epsilon_x = \frac{\epsilon_y}{-0.45} = 1 \tag{2.2c}$$

$$m_{11} = m_{22} \tag{2.2d}$$

$$m_{12} = m_{21} \tag{2.2e}$$

When these equations are solved, the piezoresistance coefficients are determined to be $m_{11} = m_{22} = 135.80$ and $m_{12} = m_{21} = 68.85$. One caveat of this analysis is that it ignores the piezoresistive effect from the geometry change of the material. In converting from resistivity change to resistance change, it was assumed that the area and length of the material was constant. It is assumed that this effect is small in comparison to the inherent piezoresistive properties present in the Metal Rubber material. This is shown to be the case in a subsequent section.

The last two tests are performed using the TA.XTplus again, but with a different sample arrangement. This test requires the sample to undergo shear strains in the XY plane, with minimal strain in the X and Y directions. This is done by mounting a square sample of material with a fixed clamp on one end and a clamp attached to the loading arm on the other. The sample is mounted such that the motion of the loading arm is perpendicular to the direction the sample is mounted, as seen in Figure 2.9. It can also be seen in this figure that the Metal Rubber sample is again attached to a hard rubber base, which is mounted to the TA.XTplus. This is done in order to prevent the sample from buckling during testing, due to the sample being so thin. The resistance is then measured in the X and Y directions, with the TA.XTplus applying shear strains up to around 4%. The results from these two tests are shown in Figure 2.10.
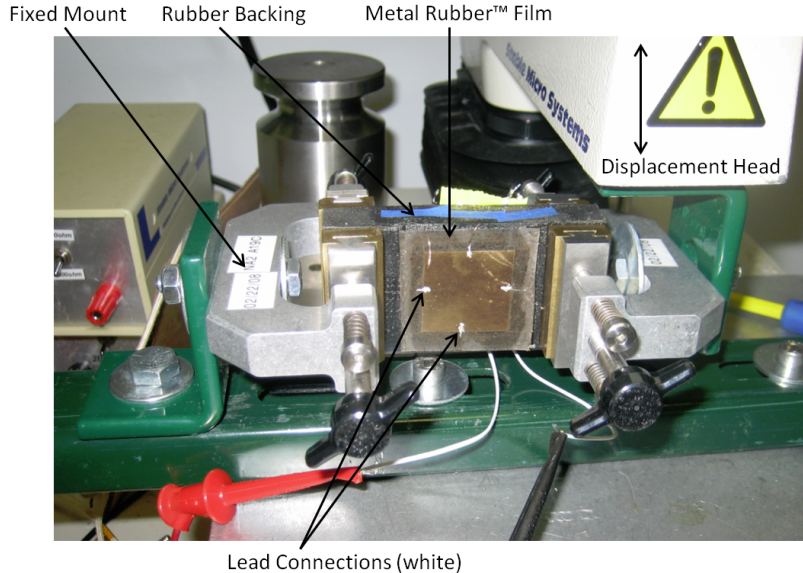
Figure 2.9: Shear Testing Apparatus

It is important to note that Figure 2.10 shows that the sign of the shear stress does not affect the results, only the magnitude of the shear stress. For an isotropic material the values of m_{14}, m_{24}, m_{41}, and m_{42} must be the same. Since there is only shear strain acting in the XY plane on the sample, only one of these tests was needed, making the second test redundant. The two test show slightly different results, but the main observation is that the piezoresistive coefficient that would result from either result is an order of magnitude lower than the piezoresistive coefficients in the longitudinal strain directions. The shear strain coefficients can thus be neglected in our subsequent analysis.
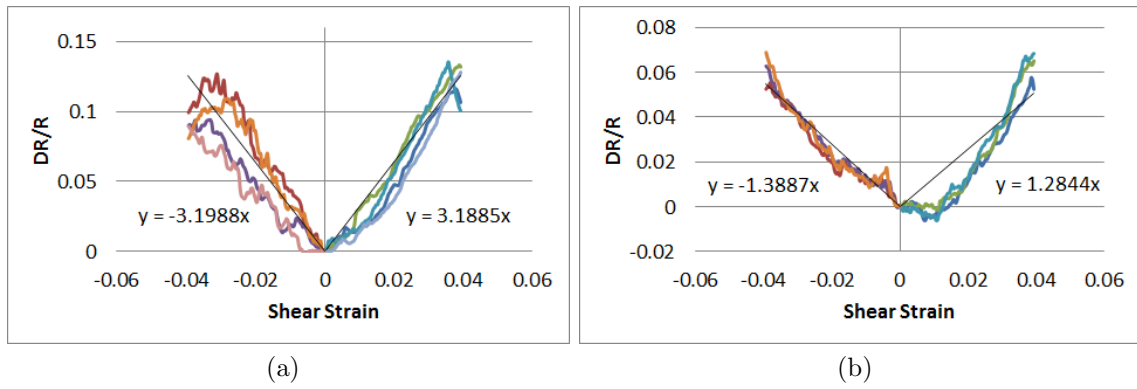
Figure 2.10: Shear Testing Results

Chapter 3

Sensor Configuration

How can one use Metal Rubber to create a skin friction sensor? In order to use the piezoresistive effect, a sensing area where the surface shear will lead to a resistance change is needed. In order to compare this resistance change at different shear levels and against other sensors the change in resistance, from the unloaded resistance of the sensor, normalized against this unloaded resistance will be used. This $\frac{\Delta R}{R}$ is very similar to what is used with most strain gages[26].

3.1   Early Sensor Trials

At the beginning of this research, little was known as to how sensors employing the Metal Rubber material worked in detail. The sensors were designed in a trial and error fashion, to see if they would respond to small shear forces. The basic design of these sensors has remained the same. The surface exposed to the flow is a sheet of the Metal Rubber thin film polymer. One side of the polymer is infused with a gold nanoparticle pattern to produce the piezoresistive sensing area. The polymer is then attached to either a piece of foam, in the original sensors, or directly to a mounting piece we have termed a "puck" to denote the shape. Leads are attached to the sensing area with either solder or conductive epoxy. Early crude tests showed a measurable response to water flow from a faucet and air flow from a hose.

In the early sensor designs, a foam layer was used to increase the strain on the Metal Rubber sheet, over epoxying the sheet directly to the mounting puck. The nanoparticle infused side of the material was oriented on the top surface, because the top surface was believed to have larger strains in this configuration. A cross section of this sensor design is shown in Figure 3.1a. In the later versions of the sensors, a section in the middle of the polymer sheet is left unattached to the mounting puck and a thin layer of oil is injected between the polymer sheet and the mounting puck. This is done to allow the sensing area of the sheet to flex more

easily under the small surface shear loads. At first, in this configuration, it was not known if having the nanoparticle infused side of the Metal Rubber sheet on the top surface or on the bottom surface would work better. A cross section of this general sensor design, with the nanoparticle infused side of the Metal Rubber sheet on the bottom, is shown in Figure 3.1b.

(a) Sensor Design 1
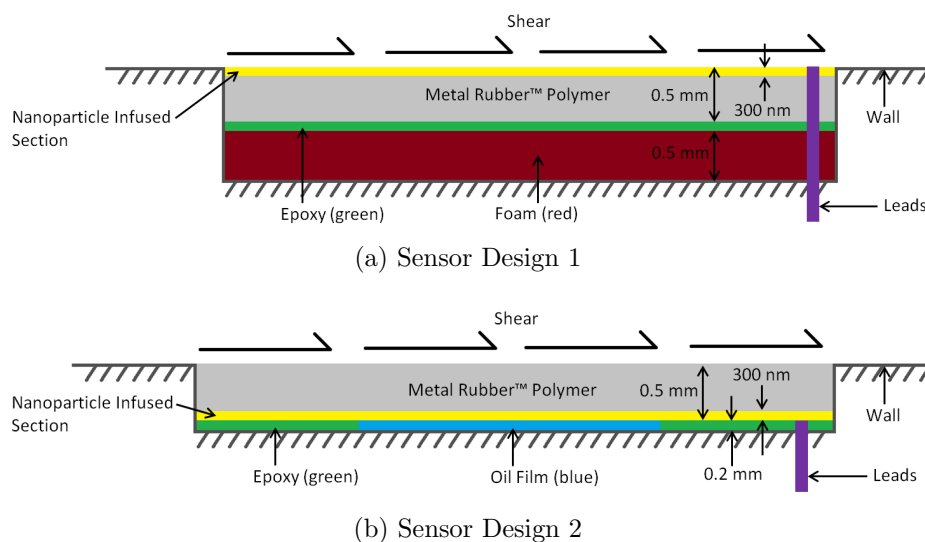
(b) Sensor Design 2

Figure 3.1: Sensor Design Cross Sections

3.1.1 Sensor Design 1

The initial sensor design had the Metal Rubber sheet glued to a piece of rigid foam, which was attached to a mounting puck, see Figure 3.1a. As seen in Figure 3.2, a strip of conductive Metal Rubber was patterned along the center line with leads on either end. Wires were soldered to the leads and fed through the mounting puck. A number of problems appeared while working with these sensors. The first was the presence of bumps at the lead attachment locations, causing unwanted flow disturbances. The second issue was sensor reliability. Often only one sensor, or even none, in a batch would work and even then, it may not produce usable data.

At this point it became obvious that in order to make a better sensor, much more detailed information on how the sensor worked was needed.
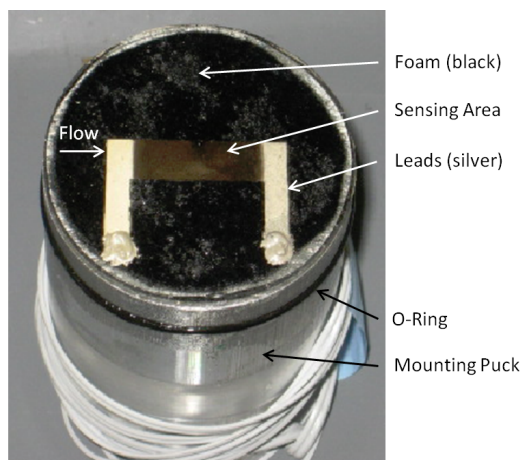
Figure 3.2: Sensor Design 1

3.1.2 Sensor Design 2

Since most of the mechanical testing had been completed prior to the Design 1 sensors, the team set out to perform additional tests to determine the electrical properties of the material. The tensile piezoresistivity tests, shown in Figures 2.5A and 2.5B, were conducted to determine how the resistance changes with strain. It was also learned that there would be little resistance change due to shear strain through the thickness, due to the conductive region being so thin. Since these sensors are being designed for low shear applications, a new design was needed to take advantage of tensile strains. The resulting design included an area of the polymer that was not glued down to the mounting puck, see Figure 3.1b. An example of this sensor is shown in Figure 3.3.
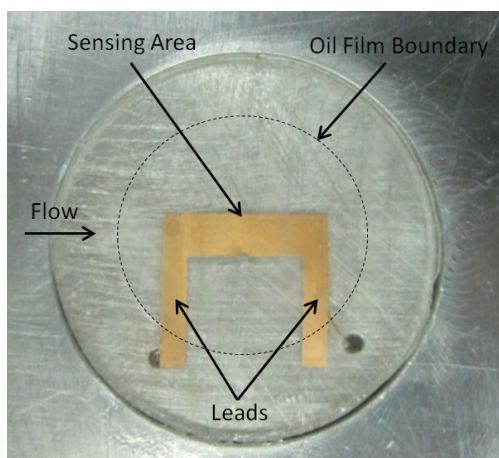
Figure 3.3: Sensor Design 2

The outer edge is glued to the sensor and the circular area in the middle of the sensor is free to move, floating on a thin film of oil. This version of the sensor was again tested extensively. More of the sensors tended to work, compared to the first version, and had better results overall. But, Design 2 still had a number of the same problems as Design 1, such as bumps at the lead connections. Another problem that was encountered was the way the sensors responded. Some of the sensors increased in resistance when strained, others decreased in resistance.

At this point, it was clear that something about the sensor mechanics was not understood. A computer model was needed in order to understand how the sensors worked. Since little was still known about the electrical properties, the piezoresistive coefficients specifically, a purely mechanical computer model was created. The strain results from this model showed how there is a tensile and a compressive side in the free floating area due to shear force displacing the center of this area. An example is shown in Figure 4.12b. If the side of the sensing area in the compressive strain is acting in opposition to the side of the sensing area in the tensile region, the two effects cancel leaving a zero net change in resistance over the entire length of the sensor. This could cause the sensors to not respond at all to the shear, but does not explain why some of the sensors did, in fact, work. It is possible that differences in symmetry between the tensile region and compressive region could lead to a response. This is further substantiated by the fact that some sensors increased in resistance and others decreased in resistance under the same load, caused by the symmetry being skewed in either the tensile or compressive direction. In order to create a sensor which worked reliably, one was needed that did not have a symmetric strain pattern across the sensing element.

One such attempt was the addition of a lead in the center of the sensing area. The idea was rather than alter the oil film geometry, use measurements that could be taken on either the tensile or compressive side of the sensing area. This sensor is shown in Figure 3.4. A solution to the lead bump issue was also attempted in this design. By cutting a section off of the puck and folding the skin over this corner, the leads could be attached and covered with an epoxy to eliminate the bump. These were a good ideas in theory, but a number of problems arose with this design.

The first problem was manufacturing these type of sensors. The additional steps required to attach and cover the leads increased building time and complexity, due to shaping the epoxy and ensuring a flat surface. The second issue, which was determined to also affect the Design 1 sensors, was corrosion. With this design, the gold infused side of the sensor skin was on the top surface of the sensor, exposed to the water flow. Due to this, the aluminum leads are also exposed. With the addition of the excitation current and water that is not pure, the leads began to corrode. It was noticed with these sensors that the leads became darker and the sensor response degraded over time. Figure 3.5 shows this effect on this sensor. It was, therefore, determined that future sensors would have the sensitive side of the sensor on the
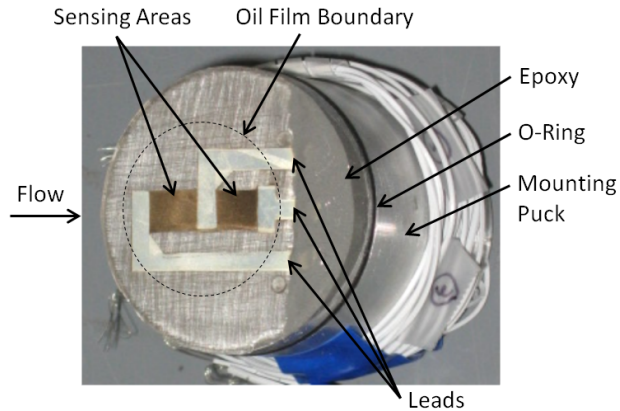
Figure 3.4: Sensor Design 2B

bottom of the skin. This decision was also shown, through the mechanical computer model, to have another positive effect, in that the strains are concentrated on the bottom surface of the skin, increasing the sensor's output.
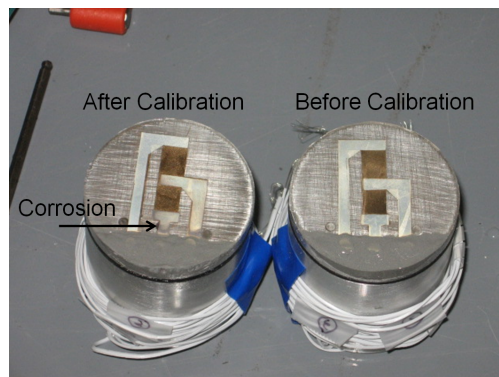
Figure 3.5: Corrosion on Sensor Design 2B

3.2 Current Sensor Configuration

Using the computer modeling software described in the next chapter, an improved design was found. This was done by observing the strain patterns on the different sensor designs. Knowing that the largest resistance changes are due to longitudinal strains on the sensing area, a pattern was created to take advantage of these strains. This lead to the current sensor design, labelled Design 3. The sensing area that was produced no longer spans the entire length of the oil film area, but returns after spanning half the oil film area, as can be seen in Figure 3.6. The response of this sensor is not only increased by eliminating the symmetry across the strain field, but also doubles the length of the sensing area in one side of either

the tensile or compressive region, depending on the mounting orientation. In addition to this, these sensors were scaled down in size from previous versions with a diameter of 19.05 mm, from the 44.45 mm of Designs 1 and 2. This reduces the sensor's measurement volume, moving closer to a point measurement. Another improvement over previous designs, was the use of copper foil for the leads. The copper foil was thinner than the wires previously used and was significantly easier to attach to the sensor skin, due to the larger contact surface area. This led to a decrease in the small bumps present near the lead attachment area and a decrease in the difficulty of manufacturing the sensor.

(a) Sensor Schematic, View from Underneath   (b) Sensor Design 3A
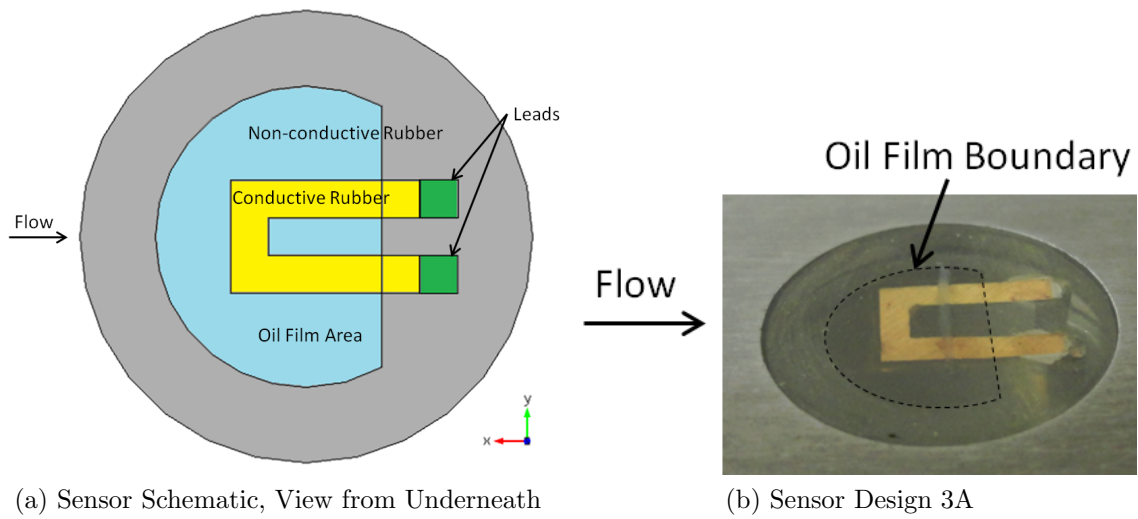
Figure 3.6: Sensor Design 3A, Single Loop Configuration

This sensor configuration can also be modified for higher output or lower shear force applications by increasing the amount of loops through the strained area. Figure 3.7 shows this idea. Since the desired shear strains to be measured are low, this sensor is more practical as it provides a larger output for the same flow conditions.

(a) Sensor Schematic, View from Underneath
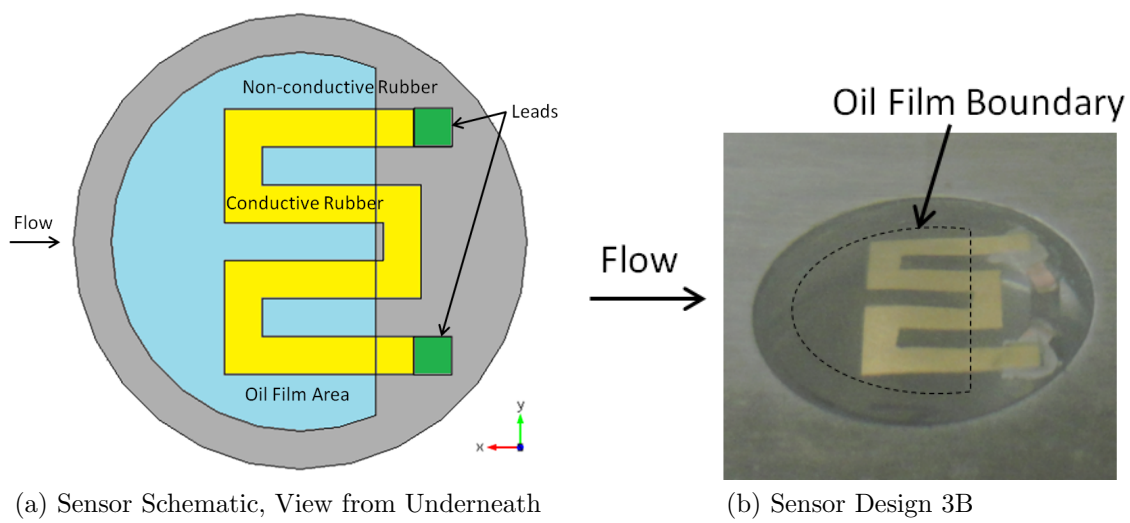
(b) Sensor Design 3B

Figure 3.7: Sensor Design 3B, Double Loop Configuration

Chapter 4

Finite Element Modeling of the Sensor

Computer Modeling of the Metal Rubber sensors involves two types of physics, the deformation of the sensor under a load and the electrical response of the material due to the deformation. The former requires an understanding of the mechanical properties, which are relatively simple to obtain and are given in Section 2.1. The latter requires an understanding of the material electrical properties, which requires more complicated testing to determine as given in Section 2.2. In order to model these two physics, software which can handle multiphysics is needed. Comsol Multiphysics®[27] is a finite element analysis software which supports mechanical-electrical coupled phenomena. In addition, Comsol includes a graphical interface which allows for user-generated equations for preprocessing and postprocessing. This is important due to the lack of a dedicated piezoresistivity module in both this software and most other commercial FEM analysis software. This permits the inclusion of the piezoresistivity equations in the electrical analysis of the material.

4.1   Model Configuration

In order to model the Metal Rubber, the variables in the program must be set up for the specific materials and physics being used in the simulation. Comsol lays out these items in a very linear fashion. The first step in creating a Comsol model is defining the geometry. This is accomplished similarly to most CAD programs, where a work plane is defined, the shape of a component is sketched on the 2-D plane, and the sketch is extruded to the specified height. Other more advanced features are available, but they are not needed for the models used in this study.

The next set of information provided to Comsol were the material properties. Four materials were needed for any model in this study: conductive rubber, non-conductive rubber, aluminum, and a resistor material. Both the conductive and non-conductive rubbers have all of the same properties except for their conductivity. Since these materials were only subjected to very small strains, the linear approximation for the Young's Modulus of 2 MPa was used. They also have a Poisson's ratio of 0.45 and a density of 950 $\frac{kg}{m^3}$. The conductive rubber has a zero load conductivity of 1300 $\frac{S}{m}$ and the non-conductive rubber's conductivity is similar to other insulators at $10^{-14}\frac{S}{m}$, where $S = \frac{1}{\Omega}$. The aluminum was used in this study as a conductor in the electrical circuit and was a built-in material in Comsol. Aluminum has a Young's Modulus of 70 GPa, a Poisson's ratio of 0.33, a density of 2700 $\frac{kg}{m^3}$, and a conductivity of $3.77 \times 10^7 \frac{S}{m}$. The resistor material was arbitrarily based on aluminum, but with a conductivity calculated to create a specific resistance using Equation 4.1.

$$\sigma = \frac{l}{RA} \tag{4.1}$$

where l is the length of the resistive material, R is the required resistance, and A is the cross-sectional area of the resistive material. Since this piece is always fixed in place and is not loaded, its properties, aside from the conductivity, are not relevant to the model. The aluminum and resistor were used as a simple way to determine the resistance of the sensing Metal Rubber, by creating a voltage divider circuit.

Once the material properties were determined and matched to their respective parts, the structural boundary conditions were created. The type of model used for the materials was specified here as linear elastic even though it is a flexible polymer as stated earlier, due to the small strains on the material. All parts of the model defaulted to the *Free* section, until a load or constraint was applied to the piece. *Initial Values*, in terms of displacement and velocity, were all set to zero for these studies. The *Fixed Constraint* is self-explanatory, used to keep a piece from displacing or deforming from its initial state. The *Roller* boundary condition acted as a frictionless wall, preventing the surface from moving in a normal direction, but allowing tangential motion. This was how the presence of the oil film under the sensor was modeled. The *Boundary Load* can be used to apply pressure and total forces in any direction on a surface. The last boundary condition is the *Prescribed Displacement*, which was used to model the tension tests to produce a known strain.

For the simulations requiring an electrical analysis, the electrical boundary conditions were imposed similarly to the structural boundary conditions. The first *Current Conservation* section defined the electrical properties of all of the materials except the conductive Metal Rubber. All parts defaulted to the *Electrical Insulation* section, until an electrical load or boundary condition was applied. There were only two of these boundary conditions needed in these studies. The first was an *Electrical Potential*, this had a value of 5 V and was applied to the top of the resistor. This was how the excitation voltage was modeled here. A *Ground* was applied to the opposite sensor lead and closed the circuit. A second *Current Conservation*

section was used to define the piezoresistive properties of the conductive Metal Rubber. This was done by specifying a user defined electrical conductivity. The user defined conductivity results from using the strains found in the structural analysis detailed above and Equations 4.2a through 4.2e.

$$\sigma_{11} = \frac{1}{\rho_0 + m_{11}\epsilon_{xx}\rho_0 + m_{12}\epsilon_{yy}\rho_0} \tag{4.2a}$$

$$\sigma_{22} = \frac{1}{\rho_0 + m_{21}\epsilon_{xx}\rho_0 + m_{22}\epsilon_{yy}\rho_0} \tag{4.2b}$$

$$\sigma_{33} = \frac{1}{\rho_0} \tag{4.2c}$$

$$m_{11} = m_{22} = 135.80 \tag{4.2d}$$

$$m_{12} = m_{21} = 68.85 \tag{4.2e}$$

The model was then meshed using the built-in physics-controlled meshing sequence. This mesh takes into account both the physics being used and the geometry of the model. The *Study* section of Comsol was used for defining parametric studies and the overall type of analysis being used, in this case a stationary solver was used since only static results were needed. The *Results* section was then used to view contour plots, calculate additional information, and for creating figures from these results.

4.2   Property and Mesh Verification Testing

In order to determine if the material properties were correct, the mesh was sufficient, and the modeling software was working correctly, a verification test was needed. A simple verification test for this application was to model the tensile test described in Section 2.1. This was accomplished by modeling the ASTM D638 dogbone geometry, shown in Figure 4.1. Since a portion of the dogbone was held in the clamps in the experiment, these portions of the dogbone were removed in the geometry in order to model the test more accurately. The motion of the tensile testing machine was modeled by fixing the left-most face of the geometry and displacing the right-most face in the x direction. The resistance of the Metal Rubber was determined by including a voltage divider in the model with a 50Ω resistor and measuring the voltage on the lead between the resistor and the Metal Rubber sample. This output voltage, V_o, was used with Equation 4.3 to determine the resistance of the Metal Rubber.

$$R = \frac{R_r V_o}{V_e - V_o} \tag{4.3}$$

where the resistor's resistance $R_r = 50\Omega$ and the excitation voltage $V_e = 5V$. Since the leads in the experiment were attached using a conductive epoxy, the leads were modeled to cover approximately the same amount of surface area on the modeled dogbone.

(a) Top View

(b) Isometric View
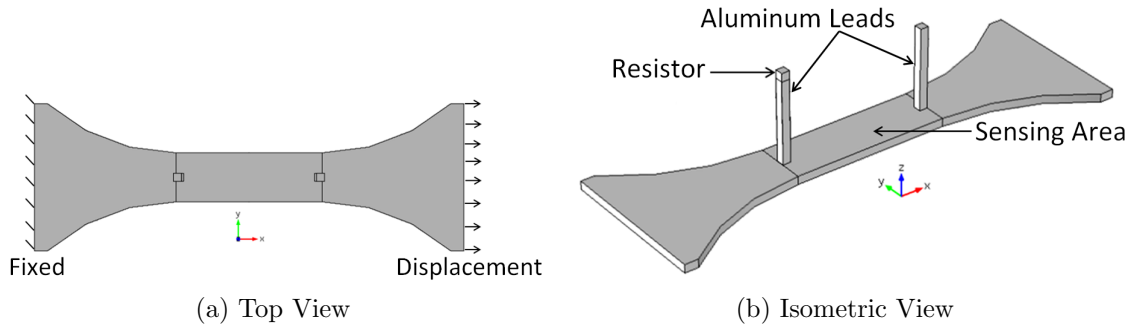
Figure 4.1: Tensile Test Verification Geometry
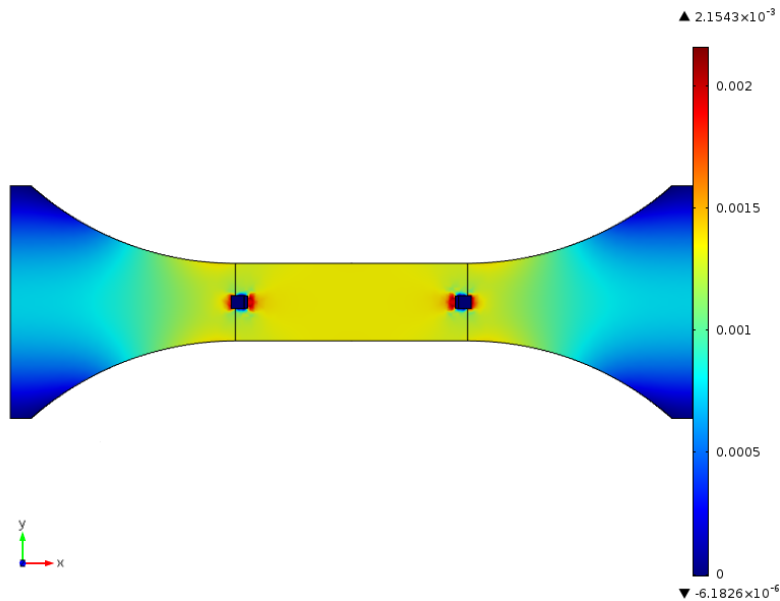
Figure 4.2: Tensile Test Verification X-Strain Contour

The model was run at a range of displacements similar to those used in the actual tensile test. In addition to the tensile displacements, the computer model can be run in compression, because buckling will not occur. The stress, strain, and voltage response of the material at each displacement level was then gathered. An example contour of the X strain on the dogbone is shown in Figure 4.2. This shows how the strain is concentrated and approximately constant in the thinnest width section, where the measurements are being taken. It is also

evident that the leads had an impact on the results by altering the strain pattern at the point where they attach to the Metal Rubber.
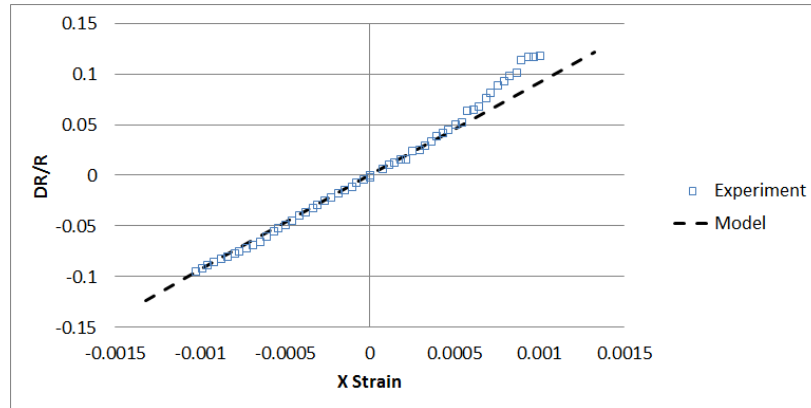
Figure 4.3: Tensile Test Verification Results

Once all of the data was gathered, the voltage response was converted into the normalized resistance change, and the results were plotted against the tensile test experiment. Figure 4.3 shows these results. The model matches well with the experimental results, only differing near the higher strains on the tensile side. This is expected, because the nonlinearities in the material were not modeled.

(a) Fine   (b) Medium   (c) Coarse
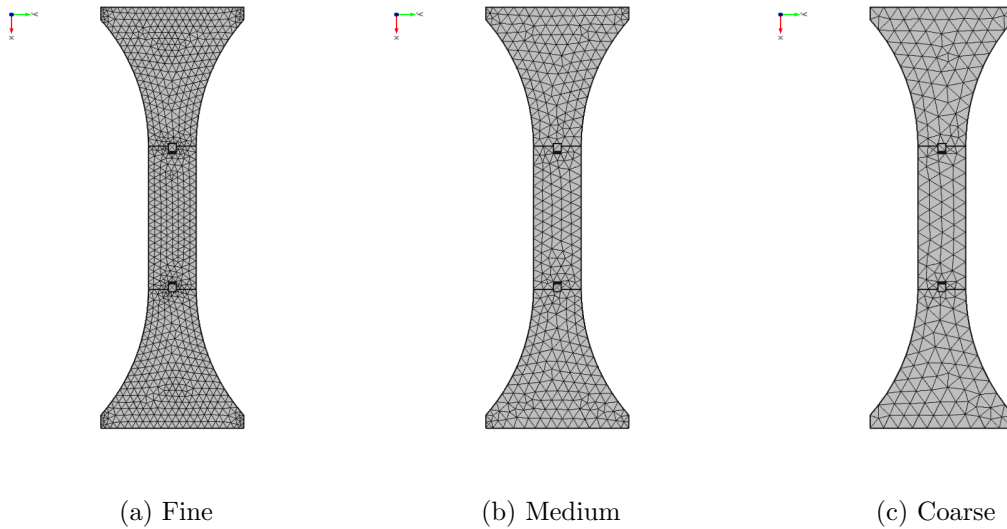
Figure 4.4: Grid Verification Mesh Size Comparison
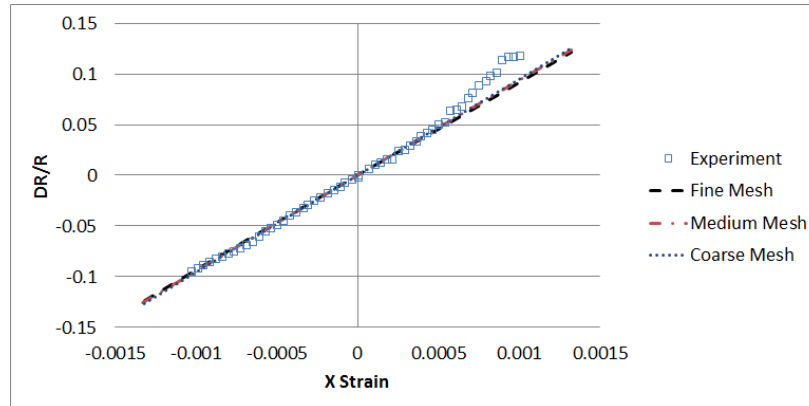
Figure 4.5: Grid Verification Test Results

To confirm that the built-in meshing sequence was adequate, these results were compared
to two additional grid results. The three grids can be seen in Figure 4.4, where the fine grid
was used in the previous analysis. Figure 4.5 shows the results from all three grids and the
experimental results. There is little difference between the three grids, with a 1.7% difference
between the slopes of the Fine and Medium grids and a 3.0% difference between the Fine
and Coarse grids. This shows that the grid sizing used in the analysis was sufficient in order
to provide accurate results.

4.3   Model Validation Testing

After it was determined that the model was working as expected, a test was needed to
determine if the model would be able to predict the behavior of more complicated sensor
configurations. This validation testing was performed using the same tensile testing appara-
tus as the material tests. The ASTM D638 dogbone sample shape was again used in these
tests, but the conductive area was patterned into a shape similar to that used in the latest
skin friction sensor configuration. Two different types of validation sensor were created, the
first, shown in Figure 4.6a, with the sensing area centered in the constant strain region and
the second, shown in Figure 4.6b with the sensing area located in a region with a strain
gradient. The dimensions of the sensing area in both types are the same and are shown in
Figure 4.7.

These two configurations were then modeled in Comsol, similarly to the tensile verification
model. Though, instead of having the conductive rubber assigned to the entire dogbone,
it was only assigned to the sensor section and the non-conductive rubber was assigned to
the rest of the dogbone geometry. Again, the model was displaced to the same extent as
the experiment and the strain and voltage response of the sensors were gathered. Figure

(a) Centered Sensor　　　　　(b) Offset Sensor
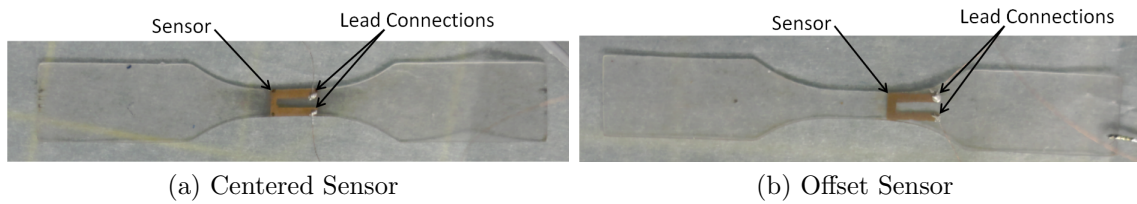
Figure 4.6: Validation Test Sensor Configurations
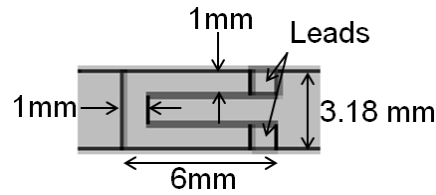
Figure 4.7: Validation Sensing Area Dimensions

4.8 shows the results of both the validation experiment and the model. It can be seen that the model predicts the response accurately up to a certain point. This point is where the nonlinearities of the material become significant.
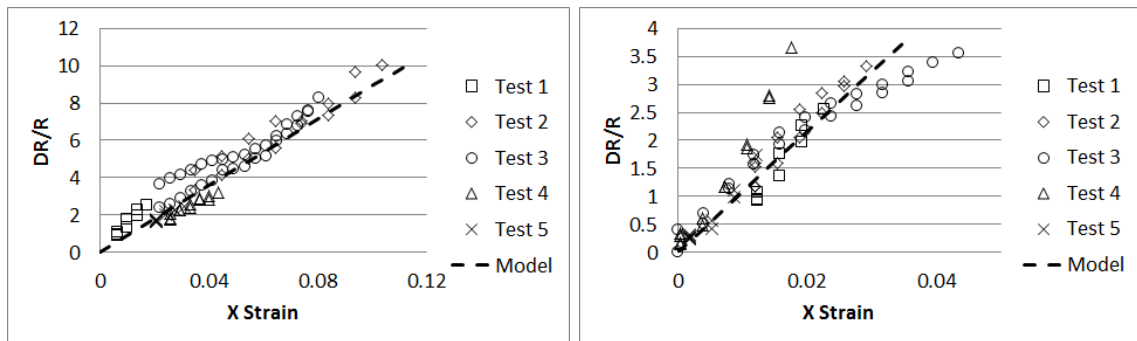
(a) Centered Sensor in Uniform Strain Area　　(b) Offset Sensor in Non-Uniform Strain Area

Figure 4.8: Validation Test Results

4.4　Skin Friction Sensor Model

Since both the verification and validation testing shows good agreement with experimental results, the skin friction sensors could then be modeled. First, the geometry of the sensor was created, an example of the single loop configuration is shown in Figure 4.9. The model's geometry consists of three main parts: the sensor skin, the oil film area, and the voltage divider circuit. The sensor skin is made up of two materials, the conductive and the

non-conductive rubber shown in yellow and grey, respectively. The conductive rubber was patterned to match the sensor being tested. The oil film area was represented only by an outline of the area, this area is highlighted in blue, as the roller boundary condition was used in place of directly modeling oil. The voltage divider circuit was again modeled using two aluminum leads, shown in green, with a resistor, in brown, attached to the top of one lead.
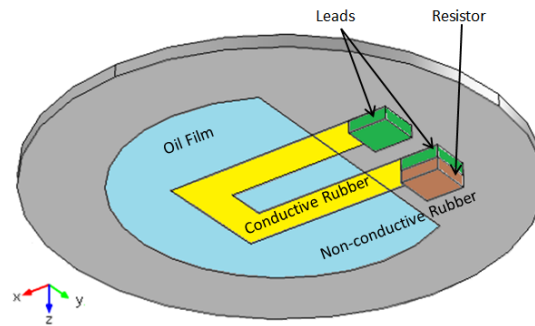
(a) Isometric View from Bottom
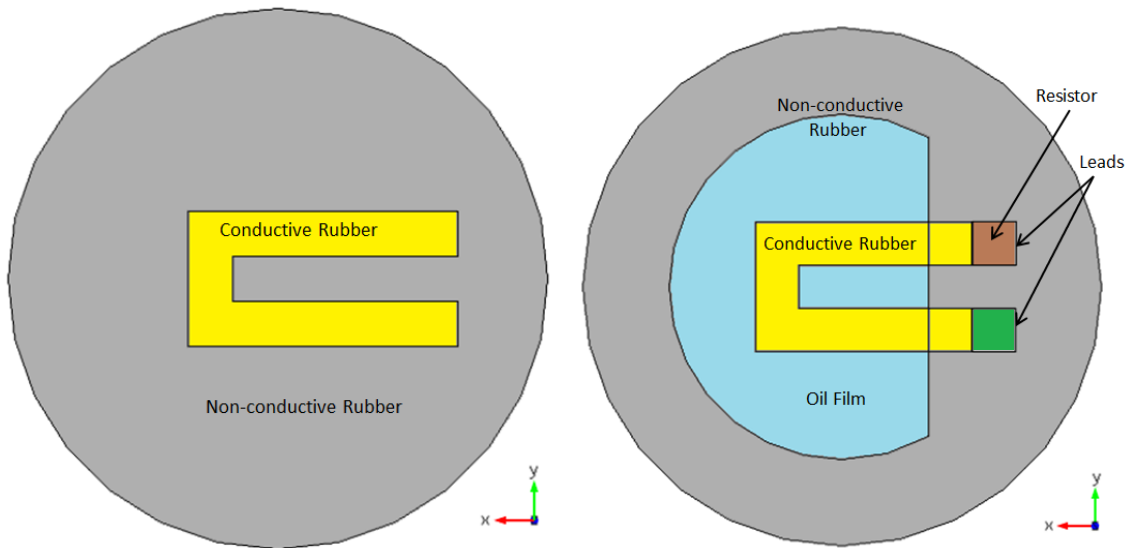
(b) Top View

(c) Bottom View

Figure 4.9: Design 3A, Single Loop Skin Friction Sensor Model

Once the geometry was created, it was meshed using the built-in physics-controlled meshing sequence. For this particular sensor, the mesh created consisted of 38193 elements and is shown in Figure 4.10. This choice was based on the mesh validation studies in Section 4.3.
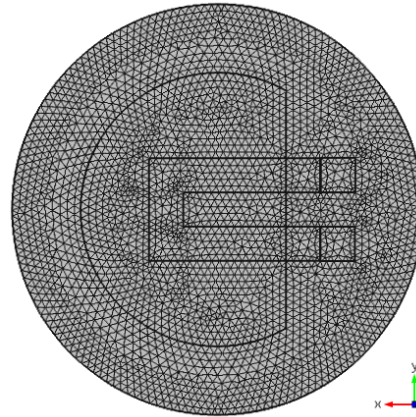
Figure 4.10: Design 3A, Single Loop Sensor Mesh
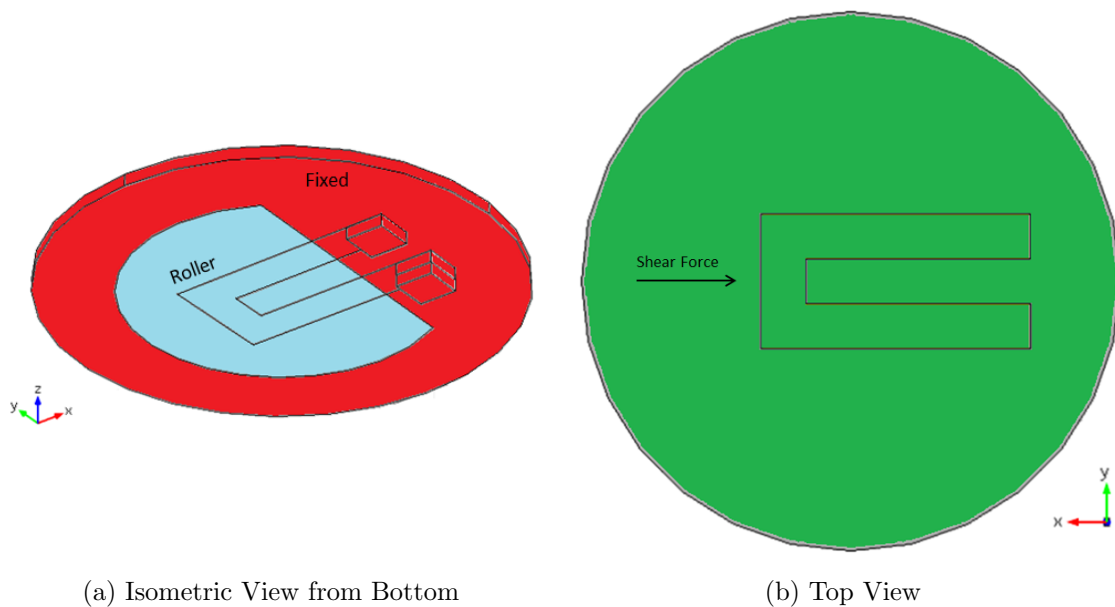
(a) Isometric View from Bottom

(b) Top View

Figure 4.11: Design 3A, Single Loop Skin Friction Sensor Model Boundary Conditions

Once the mesh was created, the boundary conditions were set. The boundary conditions for these sensors are fairly simple. Figure 4.11 shows the mechanical boundary conditions. The bottom of the sensor, except for the oil film area, and the sides of the sensor were fixed as indicated in red. A roller boundary was used on the oil film area, shown in blue, in order to model the reduced friction. A load, defined as force per unit area, was applied over the top surface, indicated in green, the direction of this force was in the negative X direction, since in the experimental set up the leads were always downstream. The electrical boundary

conditions consist only of an electric potential of $5V$ on the end of the resistor and a ground on the end of the opposing lead. With the boundary conditions set, the analysis could be run at any number of shear force settings.

(a) X-Strain Top

(b) X-Strain Bottom

(c) Y-Strain Top

(d) Y-Strain Bottom
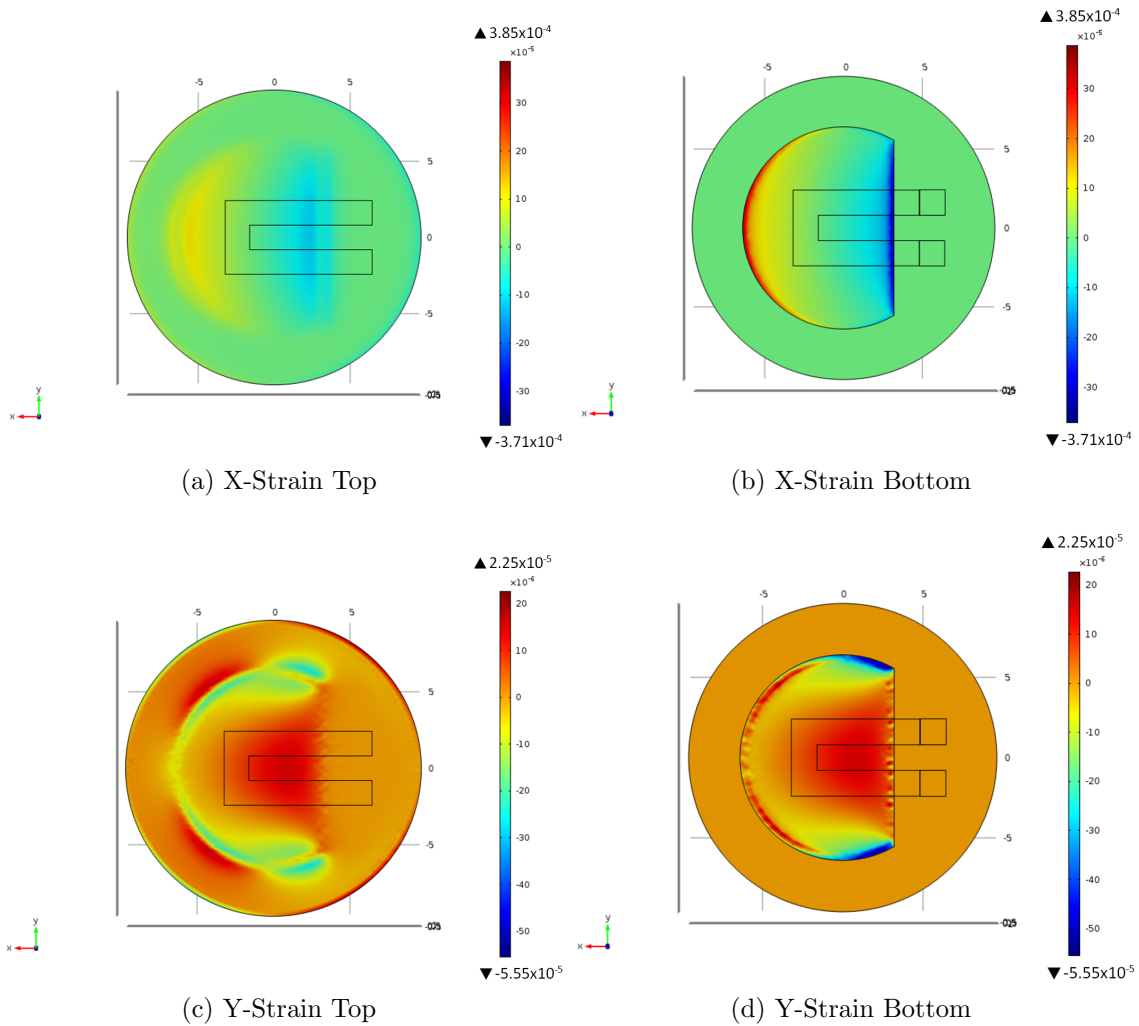
Figure 4.12: Design 3A, Single Loop Skin Friction Sensor Strain Results for a 40 Pa Shear Loading

As an example of the results produced by this model, the sensor was run at the maximum shear force that the water channel, described in the next section, can produce at around 40 Pa. This was also be a good indication as to the magnitude of the strains the sensor will experience at the end of the design range. After the analysis was run, a number of contour plots could be analysed. Figure 4.12 shows the ϵ_x and ϵ_y on the top and bottom surfaces. While the strains are fairly distributed on the top surface, they are concentrated

on the boundaries of the oil film area on the bottom surface. This shows the importance of patterning the sensor to be near or across this boundary and to have the sensitive area on the bottom of the sensor, in order to experience the highest strains. The other interesting feature is the symmetry between the tensile and compressive strains. In previous sensor designs, the sensor pattern went straight across both the compressive and tensile strains, essentially cancelling the effect of one or the other. The maximum and minimum strains on the sensor are shown above and below the legend respectively. This shows that the magnitude of strain on the sensors is on the order of 10^{-4} or less in the case of ϵ_y.

4.5   Sensor Iterative Design Study

In order to design the more optimal sensor, this computer model can be used to determine the sensor specifications needed for such a design. To do this, it is important to determine what variables affect the sensor response. The variables which affect these sensors are the material properties, both mechanical and electrical; the sensor geometry, both the oil film and sensing area configurations; the measurement circuit, including the resistor resistance and the excitation voltage; and the shear force the sensor is measuring. To determine which of these variables could be excluded from the iterative design of the sensor, each one was looked at in more detail.

The specific Metal Rubber material used for these sensors is only one of a myriad types of Metal Rubber materials that can be created. Both the mechanical and electrical properties can be manipulated in various ways, an example is the elastic modulus of the material which can be varied from the 2 MPa, used for these sensors, to greater than 100 MPa. Changing the elastic modulus also affects the piezoresistive properties of the material. Determining this effect would require the assembly of numerous Metal Rubber variations, which is not feasible for this project. Since there is no analytical way to relate these properties with the data currently available, the iterative design study was performed around the specific Metal Rubber that was created for this application.

The sensor geometry consists of many details. One of the driving factors in the design of the sensor is its overall size. The diameter of the sensor is limited by the testing apparatus. The water channel assembly was created to hold a sensor with a 19.05 mm diameter. However, the outer diameter of the sensor does not prohibit smaller sensing or oil film areas, so the outer diameter will be fixed at 19.05 mm. An optimal sensor is designed to measure shear forces at a single point in the flow, so the smaller the sensor the better. Two variables limit the size of the sensor. The first is the magnitude of strains on the sensor, which have to be large enough for the sensor to produce a meaningful output. The second is the size limit on the sensor pattern details. The smallest features that can currently be made are on the order of 1 mm. With these limits and the general Sensor Design 3A configura-

tion, a set of geometrical parameters could be found in order to create a better sensor design.

When modeling this sensor, a voltage divider was used to determine the resistance of the sensor. Two parameters were needed to perform this measurement, the resistor in series with the sensor and the excitation potential. To understand how these two parameters affect the output voltage, Equation 4.3 can be rearranged with general variables to:

$$V_o = \frac{R_s}{R_r + R_s} V_e \tag{4.4}$$

where V_o is the output voltage, R_s is the sensor resistance, R_r is the resistor resistance, and V_e is the excitation voltage. Since these variables have such a simple relationship, it was unnecessary to examine them in the design study.

The last variable that has an affect on the sensor response is the shear force that the sensor is attempting to measure. Experimentally, the sensor may not respond to the shear forces in a linear fashion after a point, due to the non-linearities in both the mechanical and electrical properties. The model, however, uses "small disturbance" assumptions in order to linearize these properties. A simple test, shown in Figure 4.13 using the default Sensor Design 3A configuration shows that the response was indeed linear through the maximum and minimum shear forces that the sensors would experience in this application.
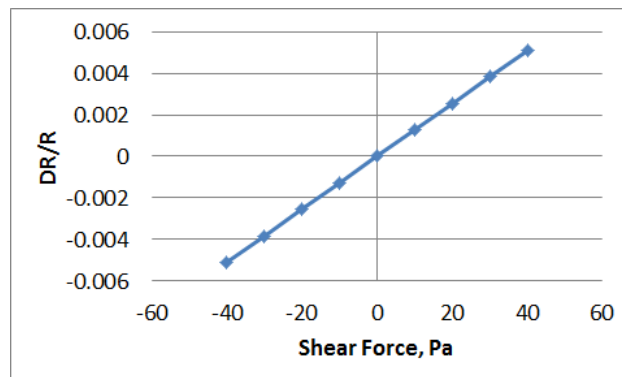
Figure 4.13: Default Design 3A, Single Loop Skin Friction Sensor Response

This left the geometry as the only parameter that needed to be studied to create a more optimal sensor. To limit the extent of the design study, the maximum and minimum values for each geometric parameter were decided. Figure 4.14 shows four main parameters that were addressed when looking at the Design 3A sensors. In order to make a better sensor, it should be as small as possible, but when the sensor size is reduced, specifically the oil film area radius, the strains are reduced on the sensitive area, reducing the overall sensor output. Since the sensor output to a given strain of 10 Pa will be used as a performance indicator,

the oil film area was left as its default size. The remaining three geometrical parameters are the leg length, the leg width, and the spacing between the two legs.
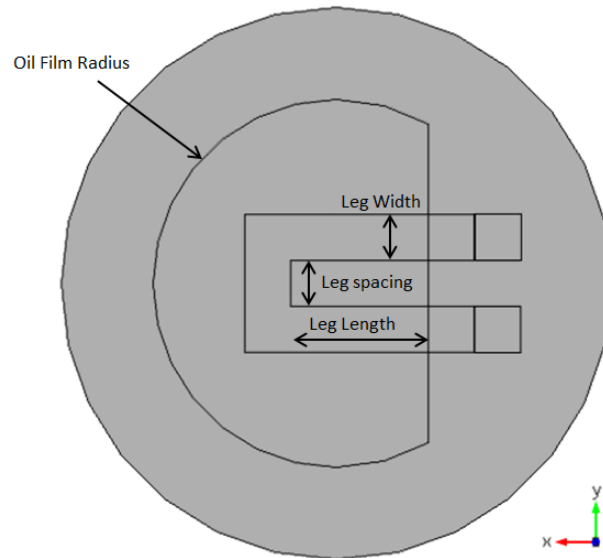
Figure 4.14: Geometrical Parameters for the Design 3A Sensor

Five different values for each parameter were used, in addition to the default design values. The default sensor had a leg length of 7.9375 mm. Since this length pushes past the center of the oil film area, which is known to be detrimental to the sensor output, this will be the maximum leg length, and the minimum leg length will be zero. Both the leg width and spacing between legs, which have a default value of 1.5875 mm, will have a maximum value of 3 mm and a minumum value of 1 mm, from the manufacturing limitations of the sensor.

To begin this design study, each variable was looked at individually, with the two remaining parameters set at their default values. This provided a good understanding of what types of values improve the design. The results from this test are shown in Figure 4.15.

From these results it can be seen that decreasing the leg length produces the most increase in response from the default configuration. This figure also shows that increasing the leg spacing has detrimental effects over the default configuration and changing the leg width has a minimal effect. Since these results are only produced by modifying a single parameter, a more optimum sensor could be created by modifying multiple parameters. Along with a few modifications based on the best results from the first iteration, the extreme cases were also attempted. Figure 4.16 shows the results from this second iteration.

Figure 4.16 shows a slightly modified form of the best sensor from the previous run with a leg length of 1.575 mm, a leg width of 1 mm, and a leg spacing of 1.5875 mm still had the
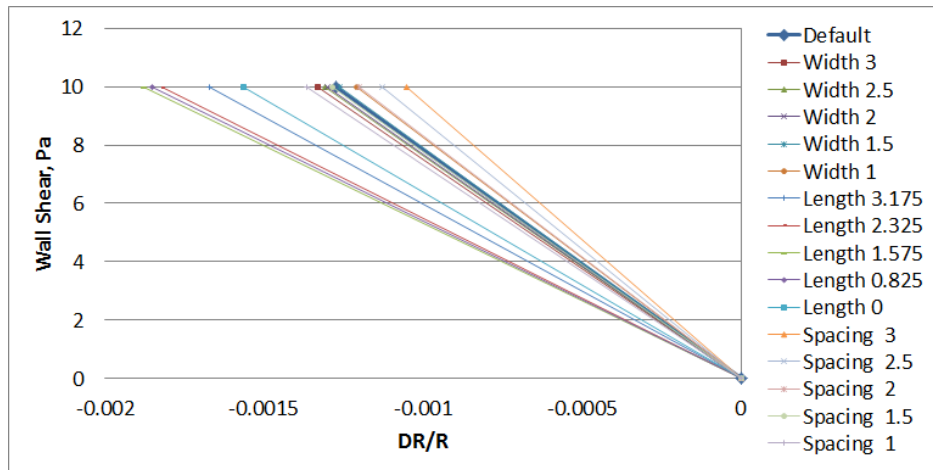
Figure 4.15: Design 3A, Individual Parameter Optimization Results
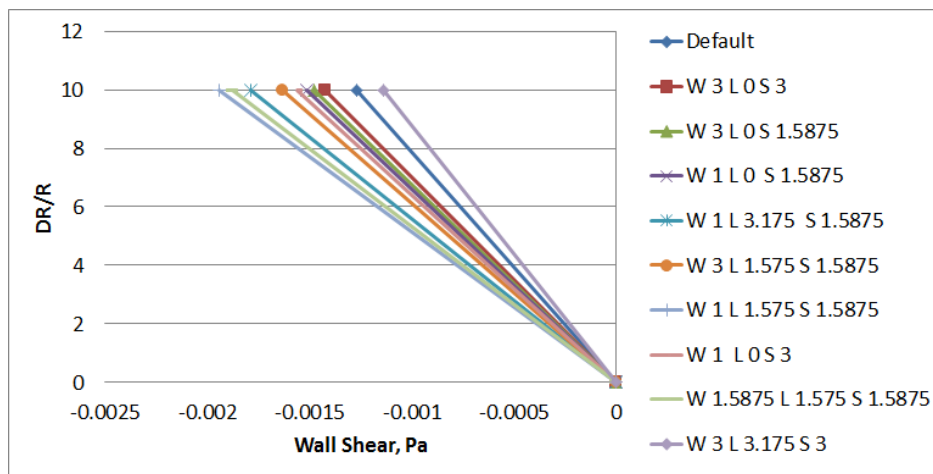
Figure 4.16: Design 3A, Multiple Parameter Optimization Results, W = Leg Width, L = Leg Length, S = Leg Spacing

best response. The schematic of this sensor is shown in Figure 4.17 along with the x-strain on the bottom surface of the sensor. This sensor has a 52.9% increased response over the default sensor design.

While this is a very simple iterative design study, it shows that the computer model can be used to take a general sensor design, and improve it to produce a much greater output for a given flow condition.

(a) Sensor Schematic, Bottom View

(b) X-Strain Bottom
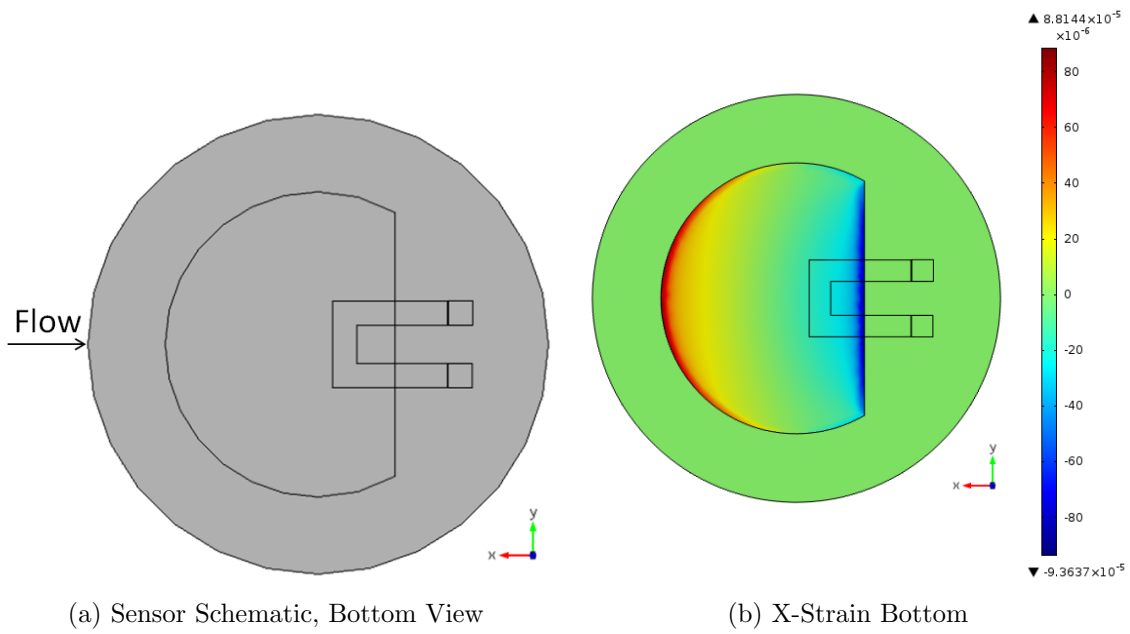
Figure 4.17: Design 3A, Single Loop Optimized Skin Friction Sensor

Chapter 5

Water Channel Studies
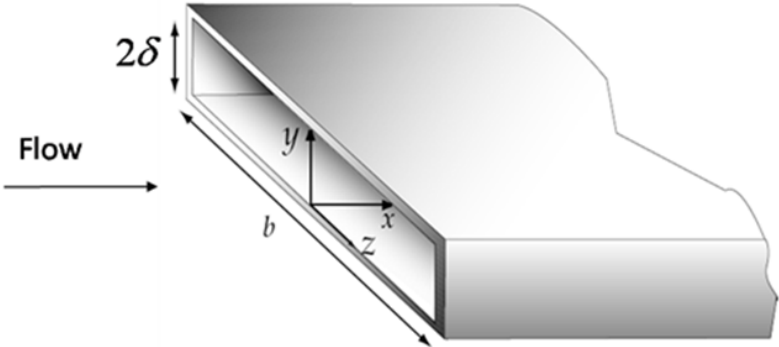
Figure 5.1: Rectangular Channel Layout. Adapted from Figure 7.1 of Pope[7]

In order to calibrate and test the skin friction sensors, a simple, repeatable, well-documented flow was needed. In this study a turbulent fully-developed channel flow was used. Water channels are a very extensively studied flow, due to the simplifications that can be applied to its analysis. Water channel flows also benefit from having direct numerical simulation (DNS) solutions at a large range of Reynolds numbers[28]. Additionally, when the water channel can be considered fully-developed, great simplifications can be included in the analysis. A fully-developed water channel is one where the boundary layers from the top and the bottom of the channel have merged and the velocity profile in the channel is no longer a function of the stream-wise direction (the x direction in Figure 5.1)[7]. This simplifies the continuity equation to:

$$\frac{dV}{dy} = 0 \tag{5.1}$$

where V is the y component of the mean velocity, which does not include the y component of the fluctuating velocity, v. Through integration of Equation 5.1 and using the no-slip

condition, which states that the $V = 0$ at the wall, the V velocity can be found to be zero everywhere. Since $V = 0$ everywhere, the y momentum equation can be simplified to:

$$-\frac{d\bar{v^2}}{dy} - \frac{1}{\rho}\frac{\partial p}{\partial y} = 0 \tag{5.2}$$

where $\bar{v^2}$ is the mean of the square of the fluctuating velocity in the y direction, p is the mean flow pressure, and ρ is the fluid density. Integrating Equation 9 results in:

$$\bar{v^2} + \frac{p}{\rho} = \frac{p_w}{\rho} \tag{5.3}$$

where p_w is the pressure at the wall. Considering that the stream-wise velocity profile does not change, taking the derivative of Equation 10 results in the equation:

$$\frac{dp}{dx} = \frac{dp_w}{dx} \tag{5.4}$$

showing that the pressure gradient in the stream-wise direction is equal to the wall pressure gradient in the stream-wise direction. Starting with the stream-wise momentum equation, a relationship between the shear and the pressure can be reached:

$$\frac{d\tau}{dy} = \frac{dp_w}{dx} \tag{5.5}$$

where $\tau = \mu\frac{dU}{dy} - \rho\bar{u}\bar{v}$. Both sides of this equation have to remain constant in order to be equal, and with the boundary conditions $\tau(0) = \tau_w$ and $\tau(\delta) = 0$ it can be seen that τ_w represents the shear stress on the wall at any point in the fully developed section of the channel. Equation 5.6 also shows the pressure varies linearly in the stream-wise direction. Integrating Equation 5.5 across the boundary layer, in this case the half-height of the channel, results in the relationship:

$$\tau_w = \frac{dp_w}{dx}h \tag{5.6}$$

where h is the half height of the channel.

In order to determine if the channel contains a fully-developed flow, the entrance length problem must be addressed. The entrance length is the distance between the start of the channel and the point at which fully developed flow begins. As shown by Anselmet[29], for a turbulent flow in a large aspect ratio rectangular duct, the entrance length can be estimated using:

$$\frac{L_e}{D_h} = 1.3Re^{1/4} \tag{5.7a}$$

$$\frac{L_e}{D_h} = 2.0Re^{1/4} \tag{5.7b}$$

where D_h is the hydraulic diameter of the pipe and Re is the Reynolds number based on the channel height and bulk velocity. The flow will become fully developed at a point between L_e due to Equation 5.7a and L_e due to Equation 5.7b. The hydraulic diameter is a term used to perform calculations in noncircular tubes and channels in a similar manner to calculations in circular tubes.

$$D_h = 4\frac{A}{P} \tag{5.8}$$

where A is the cross sectional area and P is the perimeter of the channel. With this knowledge, a water channel was designed and built for calibrating and testing the skin friction sensors.

5.1   Original Water Channel Layout

At the start of this study, a channel had already been built for previous skin friction sensor designs. This channel was originally designed by Michelle Wilson and had been used with glycerine by Magill[30] to test a cantilever beam skin friction sensor with a rubber top for damping. The original design was a "blow-down" type configuration, where a holding tank was drained through the channel and into a collection tank. The channel, shown in Figure 5.2b, was modified to use water and run continuously for the sensors in this study.

(a) Original Water Channel, from Magill[30]

(b) Modified Water Channel
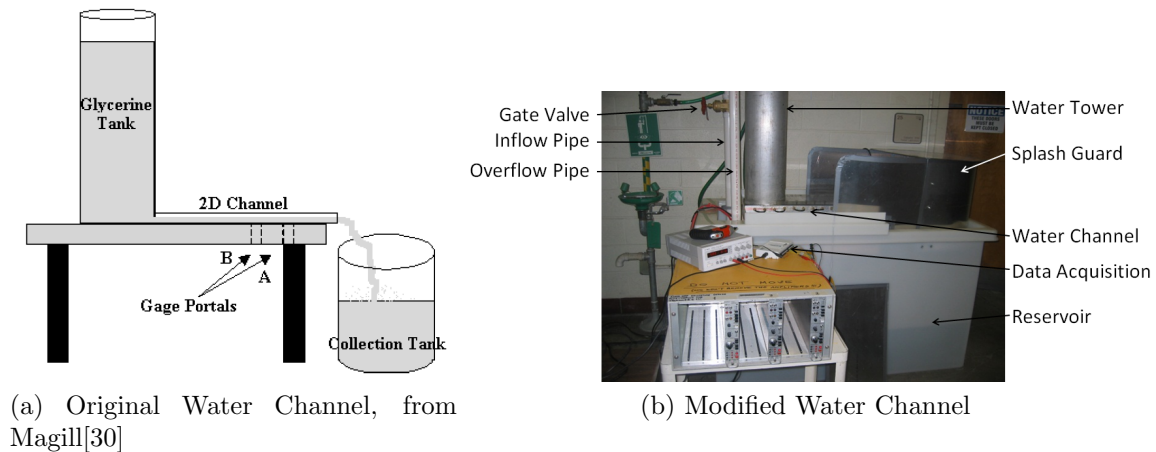
Figure 5.2: Original Water Channel

This water channel is fairly simple, using a Dayton 4/10 HP submersible water pump to move water from the reservoir to the top of the water tower. The water tower is 1.06 m tall and has an inside diameter of 210 mm. A 38.1 mm PVC overflow pipe is also connected to the top of the water tower. The channel extends from the base of the water tower and has a cross section of $6.35x127$ mm. The channel then drains back into the reservoir. The tubes

protruding from the side of the channel are part of a heating/cooling system. This allows the user to change the temperature of the channel, thus changing the fluid density, and was not used in this research. Flush diaphragm pressure transducers were mounted in three 19.05 mm holes on the bottom of the channel. The pressure transducer holes were spaced 76.2 mm apart and started 76.2 mm from the exit. A 44.45 mm hole on the top of the channel, located over the middle pressure transducer location, was used for the sensors.

This water channel was used extensively in the early sensor design phase, as both a test bed for initial sensor testing and as a calibration device for the better working sensors. Many issues with the channel design became apparent during the course of these tests. The first issue was the magnitude of the wall shear available with this channel design. Only wall shears in the range of 35-45 Pa were obtainable, limiting the range of calibration. Occasionally, siphoning into the overflow pipe would ruin test runs, drastically fluctuating the flow speed in the channel. Due to the channel being situated on top of the reservoir, it was very difficult to access. In addition, during initial Laser Doppler Velocimetry testing, optics became fogged due to the high humidity in the small space under the channel. As a result of these problems, a new water channel was designed to mitigate these issues.

5.2   Improved Water Channel Layout
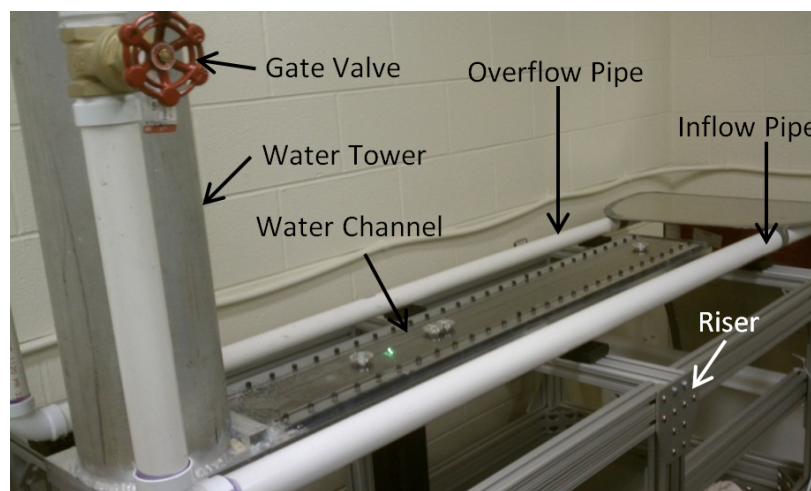
Figure 5.3: Current Water Channel Layout

The current channel being used in these studies, shown in Figure 5.3, is made of three parts: a reservoir, the water tower, and the channel. Water is pumped from the reservoir by a Dayton 4/10 HP submersible water pump through a 38.1 mm diameter PVC pipe to the top of the tower. The water tower is 1.06 m tall and has an inside diameter of 210 mm. An overflow

pipe, also a 38.1 mm PVC pipe, is also connected to the top of the water tower. This overflow pipe also contains a check valve to eliminate siphoning. The channel extends from the base of the tower with the first section having a cross section of $6.35x127$ mm. The first section extends 508 mm, at the end of which there is a backward facing step. The step doubles the height of the channel, giving it a new cross section of $12.7x127$ mm. The step increase in channel height serves two purposes. First, far downstream of the step, a new fully-developed flow has a lower shear, see Equation 5.6. Second, the flow near a backward-facing step is a complex flow that has been studied extensively. The second section extends 1016 mm, where the water exits the channel and flows back into the reservoir. In order to access the interior surfaces of the channel, the top is made of a single sheet of 12.7 mm polycarbonate. The polycarbonate top is fixed to rest of the channel by 28 screws down the length of each side. In order to allow skin friction and pressure sensors access to the channel flow, four 19.05 mm holes, one on the top surface in the center location and three on the lower surface of the channel, are located at both the upstream and downstream locations. In addition to these access points, there are two access holes in the bottom and top surfaces just downstream of the step. The entire channel sits on a 610 mm tall riser, which allows access underneath the channel. A drip pan is fixed to the riser in order to mitigate any water leaks. The riser and drip pan are mounted atop a 686 mm tall welded metal workbench bringing the channel to chest height.

(a) Top View

(b) Sectioned Side View
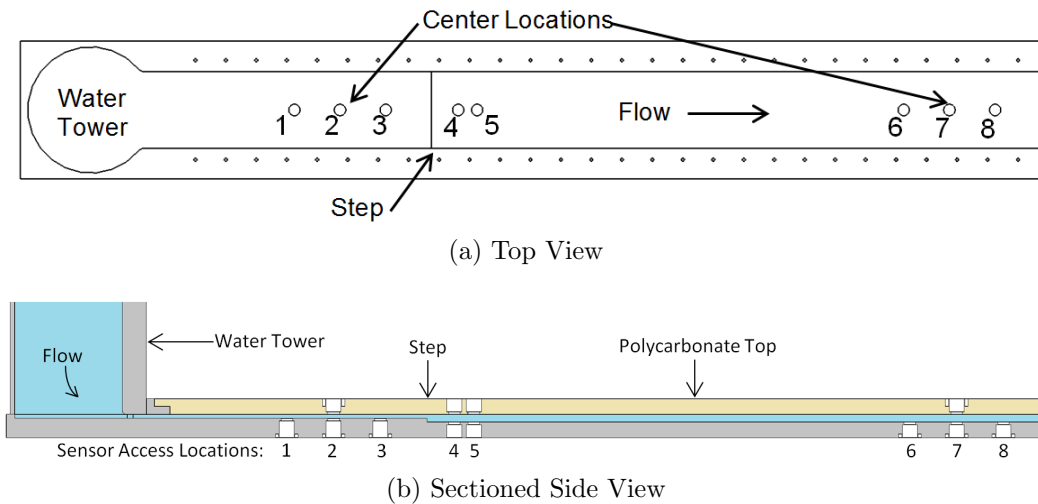
Figure 5.4: Water Channel Diagram Highlighting Sensor Access Locations

In order to determine if the upstream and downstream locations are truly fully-developed, the starting length must be determined. Using Equations 5.7a and 5.7b, it was found that the upstream location will have a starting length between 234 and 361 mm and the downstream will have a starting length between 526 and 810 mm, based off of the highest estimated channel velocity of around 4 m/s. Since this is based on the maximum channel velocity, calculated from the maximum water height in the tower, and not the bulk velocity, the starting

length will be shorter than this worst case scenario. This shows that Location 1 may not be in a fully-developed flow, but Locations 2, 3, 6, 7, and 8 will always be in a fully-developed flow.

5.3 Calibration

Sensor calibration is accomplished by recording the output of the skin friction sensor in the upstream and downstream locations at multiple flow speeds. The skin friction sensor is located above ports 2 and 7 in the upstream and downstream tests, respectively. Two methods are available for determining the wall shear at these points. The first is by taking pressure measurements in the fully developed flow and using Equation 5.6 to calculate the wall shear. The second is by using Laser Doppler Velocimetry to determine the velocity profile, from which the skin friction can be deduced. While the LDV measurements can produce accurate skin friction measurements, it is time consuming to collect the amount of data needed for the velocity profiles. In addition, due to deficiencies in repeatably setting the water flow gate valve, the measurements at each valve setting differ slightly from run to run, inducing higher uncertainties in the LDV results for a given calibration run. Pressure measurements, however, can be taken easily during each calibration run, reducing uncertainty in the calibration measurements.

Therefore, the wall shear was calculated using Equation 5.6 with the pressure gradient calculated from pressure measurements at ports 2, 3, 6, 7, and 8. Pressure port 1 was not used due to uncertainty in whether it is fully-developed flow at this point. Two pressure measurements are sufficient at this upstream location due to the higher shear force expected. Three pressure measurements at the lower shear level in the downstream location reduce the uncertainty in this value. The two locations provide a large variation in wall shear, on the order of 35 Pa and 10 Pa in the upstream and downstream locations, respectively. Adjusting the flow speed varies these shear stresses ± 5 Pa about these nominal values.

5.3.1 Pressure Measurements

In order to determine the type of pressure sensor required for the calibration, the magnitude of pressure in the channel must be understood. This is accomplished by determining the maximum pressure that will be seen in the channel. This maximum pressure is dictated by the height of the water column feeding the channel. With a maximum column height of around 1.06 m the maximum pressure will be about 10,000 Pa at the entrance of the channel. Since the measurements will take place near the end of each fully developed region, the pressures will be much less than 10,000 Pa. It is estimated that the pressures will be on

the order of 3450 Pa in the upstream section and 690 Pa in the downstream section. These pressures are low enough that the pressure transducers viable in this application, namely flush diaphragm type sensors, have poor uncertainty at these levels. A very cheap, accurate, and easily implemented alternative to a transducer is the water column manometer. Small pressure changes produce relatively large changes in the water column height in a manometer and since only static, steady state, measurements are needed, their low time-response rate is not an issue. Only the interface between the manometer and water channel needs to be engineered to produce the best results. This piece, shown in Figure 5.5, has a inlet hole with a diameter of 1.59 mm, which is small enough to be considered a point measurement in the flow, but large enough to prevent capillary forces from skewing the results. The inlet is then widened at an angle, rather than with a step, in order to prevent air from being trapped. The outlet has a standard NPT fitting to attach the pressure tubes.
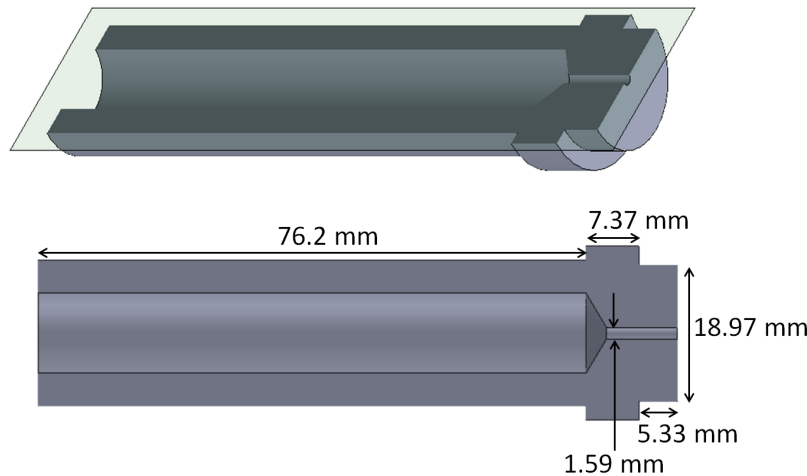
Figure 5.5: Manometer to Channel Interface Fitting

These fittings are attached to the water channel at the three bottom locations, either upstream or downstream, depending on the calibration taking place. Polyurethane tubing connects the fittings to the impact-resistant, clear, polycarbonate tubing that will act as the manometer. The three manometer tubes are situated in close proximity and the water height is measured using a ruler secured alongside the tubes. The entire assembly is shown in Figure 5.6.

Measurements during numerous calibration runs were collected and analysed to determine the accuracy of the manometer setup. It was found that the runs match very well, as can be seen in Figure 5.7. Since the upstream location is followed by a step and does not exit to atmospheric pressure, the locations closer to the step have negative pressures. The downstream location, however, does exit to atmospheric conditions, and the pressures trend towards zero at the exit as expected. The shear values, calculated using these pressure
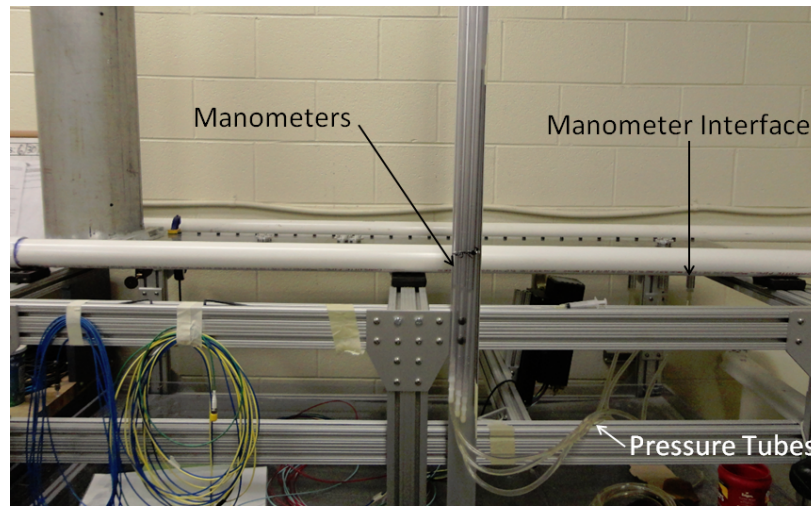
Figure 5.6: Manometer Assembly Attached to the Water Channel

measurements, at each level are shown in Figure 5.8. It should be noted that the while the water channel can be run at the lowest flow setting, the flow is not ideal. This is due to flow interference in the form of bubbles, which appear due to the recirculating water splashing into a lower water level in the water tower. Since these bubbles detrimentally affect the bulk flow, this setting was not used for sensor calibration.

(a) Upstream

(b) Downstream
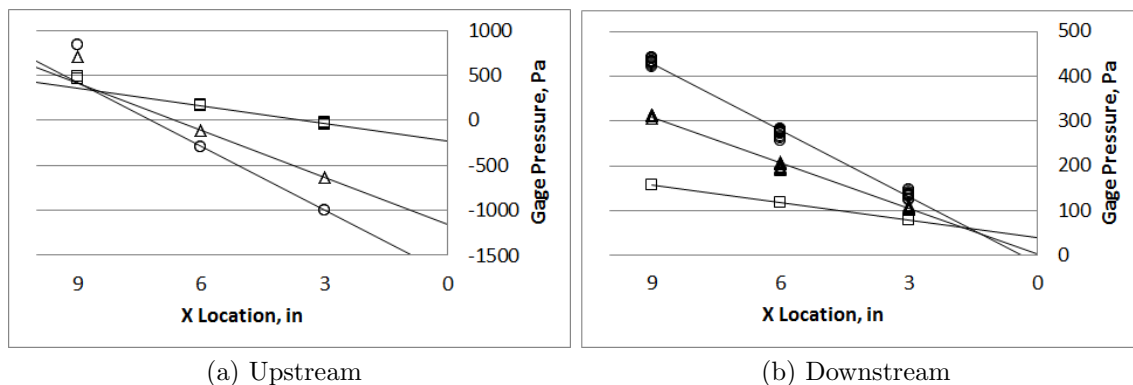
Figure 5.7: Gage Pressure versus Distance to Section End at Three Flow Levels

5.4   Laser Doppler Velocimetry

Laser Doppler Velocimetry (LDV) was used to document the flow in the water channel. This technique utilizes the interaction of lasers and particles in a flow to determine flow speed.

(a) Upstream   (b) Downstream
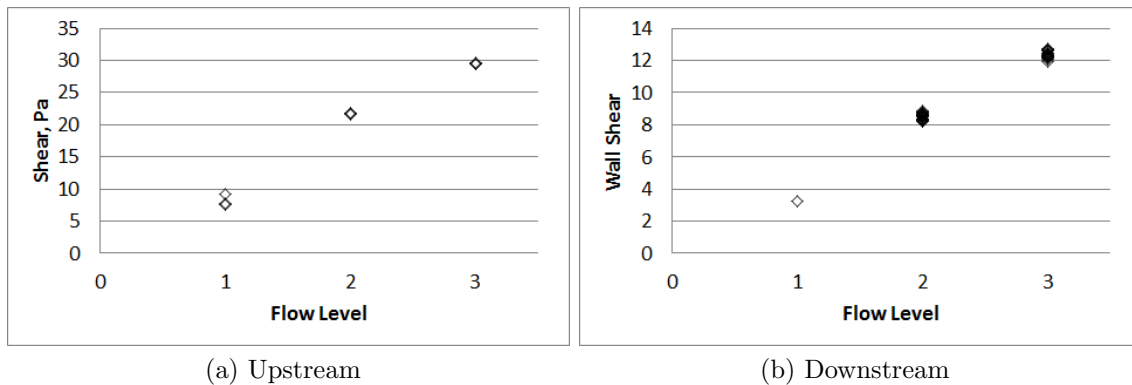
Figure 5.8: Calculated Wall Shear versus Flow Level

The LDV does this by crossing two or more beams of collimated, monochromatic, and coherent laser light at a point in a fluid flow. The beams interfere with one another at the point which they intersect, generating a set of fringes. As a particle passes through the fringes, it reflects light, which is collected and processed by a photodetector. This provides velocity measurements which are highly resolved in space, time, and velocity. This method is also non-intrusive to the flow, provided the particles being used are small enough. In order to produce velocity data from the LDV, only knowledge of the laser wavelengths and angle of intersection are needed.

The LDV sensor works on the principles of the Doppler shift. As the particles pass through a laser beam, the reflected light is shifted based on the laser beams relative propagation vector and the particles relative velocity vector. Unfortunately, the magnitude of shift in frequency of the reflected light is so low that there are no detectors that can pick up this change directly. This is why two beams are used, creating the fringe pattern of bright and dim light as seen in Figure 5.9. As particles pass through the fringe space, they create modulating intensity signals. The distance between two fringes can be calculated using the dual beam Doppler equation:

$$d = \frac{\lambda}{2Sin(\theta)} \tag{5.9}$$

where λ is the laser beam wavelength and θ is the half-angle of intersection between the two beams.

In order to further understand how to use an LDV sensor and understand the data produced by an LDV sensor, a two-component, span-wise and stream-wise, LDV was used. Created by Dr. Lowe at Virginia Tech, this LDV utilizes a Coherent Verdi V6 frequency-doubled $Nd : YVO_4$ diode-pumped solid state laser. To determine the fringe spacing the angles of intersection of the three beams are needed. This was done by measuring the locations of
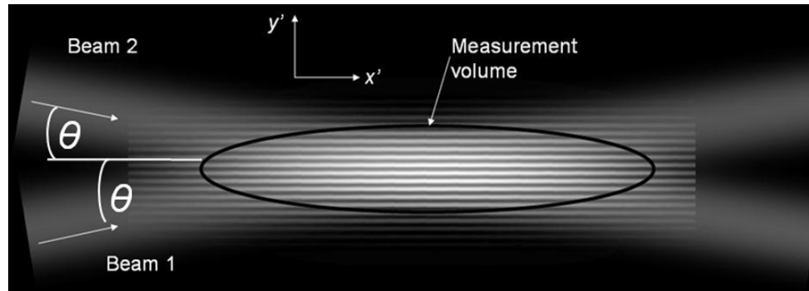
Figure 5.9: LDV measurement volume showing the fringe spacing created by the interference of the two laser beams. Lowe [8]

the beams at a fixed distance, traversing a set distance and measuring the beam locations a second time, as shown in Figure 5.10. This LDV has a wavelength $\lambda = 532nm$ and a
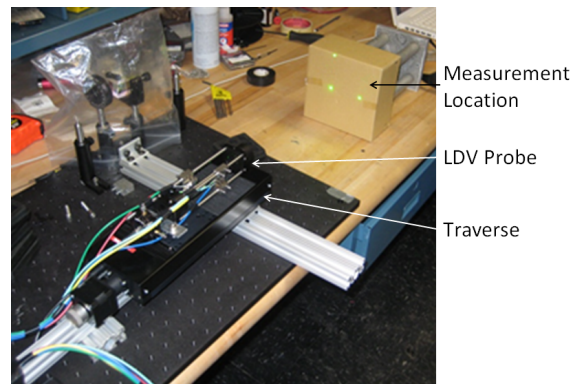
Figure 5.10: Beam Angle of Intersecting Analysis

half angle of intersection $\theta = 6.9\,\mathrm{deg}$, yielding a fringe spacing $d = 2.2\mu m$. The particles used for reflecting the laser light were monodisperse polystyrene latex spheres of $2\mu m$ in diameter. A photomultiplier is used to measure the light intensity fluctuations received from the scattering particles, and the current signal from the anode is converted to voltage using a low noise amplifier with 50 Ohm impedance. The voltage signal is digitized using an 8-bit analog-to-digital converter capable of acquiring up to 250 million samples per second. The photonics probe is mounted on a single-axis automated stage with $100mm$ of travel. The traverse is driven and controlled via a LabVIEW-enabled stepper motor controller with positioning precision less than $0.5\mu m$.

Since the average velocity values that are found using the LDV are calculated from the instantaneous velocity values measured by the LDV, the uncertainty in these calculations are estimated based on the number of samples acquired. It has been found, Lowe and Simpson[31], that the uncertainty in LDV measurements is usually not limited by the instrument uncertainties, but by the statistics of the turbulent fluctuations in the flow. The

statistical standard error of these mean values can be calculated using the equation:

$$\partial U = \frac{\sigma(U)}{\sqrt{N}} \tag{5.10}$$

where ∂U is the standard error in the estimate of the mean value U, $\sigma(U)$ is the standard deviation of the sampled quantity U, and N is the number of samples acquired. Equation 5.10 can be extended to higher order statistics, such as the mean-square shown in Equation 5.11a, since they are simply mean values of other sample moments.

$$\partial \bar{u^2} = \frac{\sigma(u^2)}{\sqrt{N}} \tag{5.11a}$$

$$where \; \sigma(u^2) = \frac{[\sum_{k=1}^{N}(u_k^2 - \bar{u^2})^2]^{1/2}}{\sqrt{N}} = \sqrt{\bar{u^4} - (\bar{u^2})^2} \tag{5.11b}$$

Typical values for 95% confidence uncertainties are $\frac{\partial U}{u} = \pm0.12$ and $\partial\frac{\sqrt{\bar{u^2}}}{u} = \pm0.34$, while extreme values near the wall are $\frac{\partial U}{u} = \pm0.25$ and $\partial\frac{\sqrt{\bar{u^2}}}{u} = \pm0.69$.

Once all of the data has been collected from the water channel, it must be reduced and analyzed. The LDV system used gives three different sets of values. The first set of values is the entire set of U velocities measured at each point in the flow, the second set is all of the V velocities measured at each point in the flow, and the last set is the magnitude of the velocity at a 45 degree angle between the U and V directions. The last set of data is a redundant set, allowing the user to check or compare the individual results. In order to get mean flow velocities, the data at each point is examined. There are three groups of points acquired by the LDV probe. There is a relatively compact set of points and two sets of outliers in both the x and y directions away from the central group. These outliers are data points due to flare from the optical lenses and are discarded. Once this is completed the mean and fluctuating velocities can be calculated and scaled appropriately.

5.4.1   LDV Water Channel Results

For the fully-developed sections of the flow, the velocity can be scaled on the friction velocity $u_\tau = \sqrt{\frac{\tau_w}{\rho}}$ to give $U^+ = \frac{U}{u_\tau}$ and the length y can be made dimensionless similar to a Reynolds number by $y^+ = \frac{yu}{\nu}$ where ν is the kinematic viscosity. When scaled on these wall variables, the mean velocity profiles should collapse to the log wall equation given by Equation 5.12.

$$U^+ = \frac{1}{\kappa}\ln(y^+) + B \tag{5.12}$$

where $\kappa = 0.41$ is the von-Karman constant and $B = 5.2$ is another empirical constant. At $y^+ < 20$ the profile will diverge from the log law following a curve that is described by Spalding [9] that blends between this log region and the linear region. The linear region then becomes dominant at around $y^+ < 6$ and is described by $U^+ = y^+$.

Once the friction velocity is known, along with all the previous information gathered from the velocity profiles, a number of useful parameters can be calculated. Two Reynolds numbers can be garnered from this analysis, the first based on the centerline velocity U_0 and the second on the friction velocity u_τ, both utilize the boundary layer thickness, the channel half-height in this application, as a length scale. Using the definition of the friction velocity, the wall shear can be calculated. In addition, the skin friction coefficient can be calculated using the following relationship:

$$\frac{u_\tau}{U_0} = \sqrt{\frac{C_f}{2}} \tag{5.13}$$

A compilation of these values for the upstream and downstream locations at each speed setting can be found in Tables 5.1 and 5.2, as well as a color code for all subsequent plots.

Table 5.1: Flow parameters for the three upstream locations

Location	Flow Level	U_0, m/s	τ_w, Pa	u_τ, m/s	Re_0	Re_τ	C_f	Plot color
1	3	4.2774	47.00	0.217	13530	148685	0.005147	Blue
2	3	3.8834	38.73	0.197	12284	122540	0.005147	Green
3	3	3.8817	37.95	0.195	12278	120065	0.005047	Red
1	2	3.7503	37.56	0.194	11863	118837	0.005352	Cyan
2	2	3.6719	34.16	0.185	11615	108066	0.005077	Magenta
3	2	3.5803	33.42	0.183	11325	105742	0.005225	Yellow

Table 5.2: Flow parameters for the three downstream locations

Location	Valve setting	U_0, m/s	τ_w, Pa	u_τ, m/s	Re_0	Re_τ	C_f	Plot color
6	3	2.2873	12.52	0.112	7235	39608	0.004795	Blue
7	3	2.3033	12.74	0.113	7285	40318	0.004814	Green
8	3	2.3164	12.74	0.113	7327	40318	0.004759	Red
6	2	1.9036	9.199	0.096	6021	29099	0.005087	Cyan
7	2	1.9013	9.103	0.096	6014	28797	0.005046	Magenta
8	2	1.9112	9.008	0.095	6045	28496	0.004942	Yellow

As can be seen in Figures 5.11a and 5.11b, all of the velocity profiles follow the log law well. Figures 5.11a and 5.11b also show that the flow is highly two-dimensional, with the

(a) Upstream   (b) Downstream
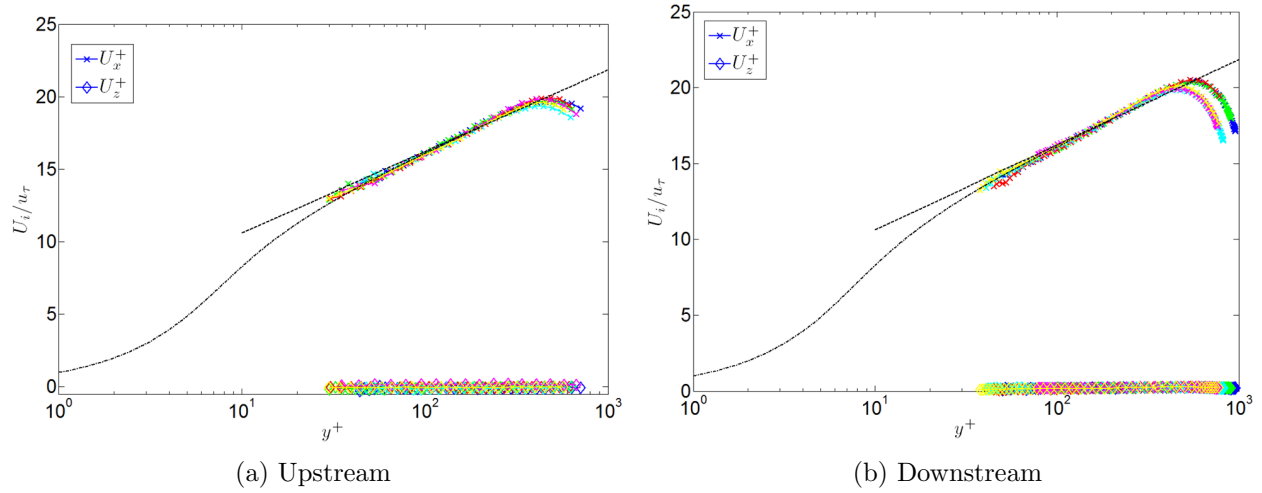
Figure 5.11: Mean velocity versus height from channel floor, scaled on wall variables dashed line: log law, dash dot line: Spaldings blend[9]

span-wise flow velocities within the statistical uncertainties of being zero.

Moving in the channel to the two locations following the backward facing step, a few different procedures are needed to analyze the flow. The mean velocity profiles cannot be scaled on the wall variables. Instead, the law of the backflow is used, which is shown below:

$$\frac{U}{U_N} = A(\frac{y}{N} - \ln|\frac{y}{N}| - 1) - 1 \tag{5.14}$$

where $A = 0.3$ is an empirical constant, U_N is the maximum negative mean velocity, and N is the y location of the maximum negative mean velocity. Table 2 shows the values for these variables for each location and speed. Location 5 uses the same scale factors as Location 6 for each speed respectively for comparison purposes, since this location is just downstream of the reattachment location and there are no negative mean velocities. The mean velocity

Table 5.3: Flow parameters for the two locations after the back-step

Location	Flow Level	U_0, m/s	U_n, m/s	N, mm	Re_0	Plot Color
4	3	3.8417	-0.3106	0.132	24304.38	Blue
5	3	2.8231	-0.3106	0.132	17860.24	Green
4	2	3.2324	-0.2655	0.132	20449.67	Red
5	2	2.4216	-0.2655	0.132	15320.17	Cyan

profiles for these two locations scaled on the backflow variables can be found in Figure 5.12.

Velocities across the entire channel were measured, since these profiles will not be symmetrical from the top and bottom walls. It can be seen from this figure that the location with backflow collapses to the law of the backflow. This area is also very two dimensional, with very low span-wise velocities.
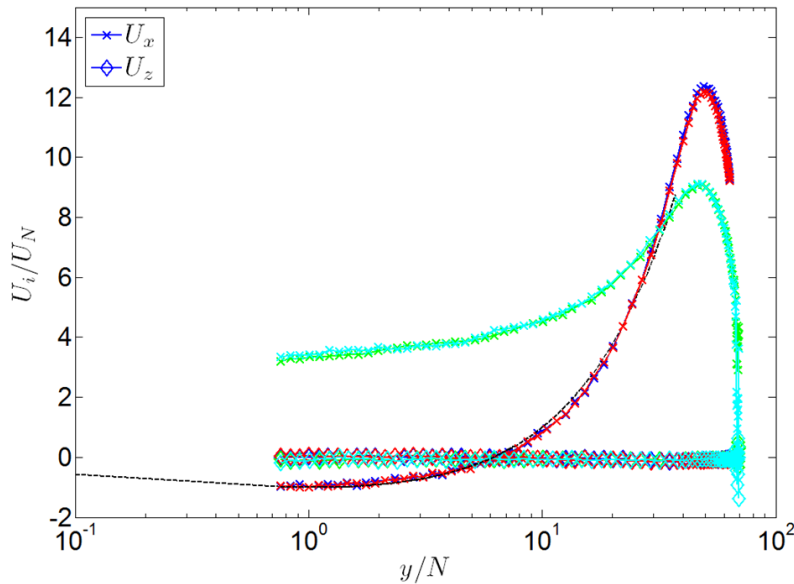
Figure 5.12: Mean velocity versus height from channel floor, scaled on backflow variables dashed line: Law of the Backflow Simpson [10]

5.5   Computational Fluid Dynamics

In order to get a better understanding of the flow in the channel, especially near the step, more information is needed than can be provided by LDV results alone. A Computational Fluid Dynamics (CFD) simulation can be used to determine what is happening in places that the LDV sensor cannot reach. What the LDV data does provide, is a comparison for the CFD results, allowing validation of the CFD results and vice versa. Since the LDV results have already shown that the channel is sufficiently two-dimensional, a CFD analysis can be greatly simplified. The ANSYS 13.0 software was used in this anaylsis, due to its inclusion of the Fluent CFD module[32]. ANSYS Fluent is a broad fluids dynamics simulator that can be used to model turbulence, heat transfer, and even reactions. Due to limitations in the grid generation software in ANSYS, a program called Gridgen was used. Gridgen is a complete meshing toolkit, with numerous options that allow for generation of very complicated, high quality meshes[33].

5.5.1 Geometry and Meshing

Since CFD simulations can be processing intensive, it is a good practice to simplify the geometry as much as possible while still maintaining the integrity of the problem. The first simplification is the use of a two-dimensional representation of the water channel, since the LDV results have already shown that there is negligible spanwise flow. The water channel is made up of a myriad of parts, but the majority of these parts are immaterial to the problem being analysed. The only pieces that need to be modeled are the water tower and the channel itself. The water tower, however, can be simplified further by assuming the flow speed is essentially zero. In place of the full tower, only the section closest to the inlet of the water channel was modeled. Figure 5.13 shows the water channel as modeled for the CFD simulation, using the ANSYS geometry tool.
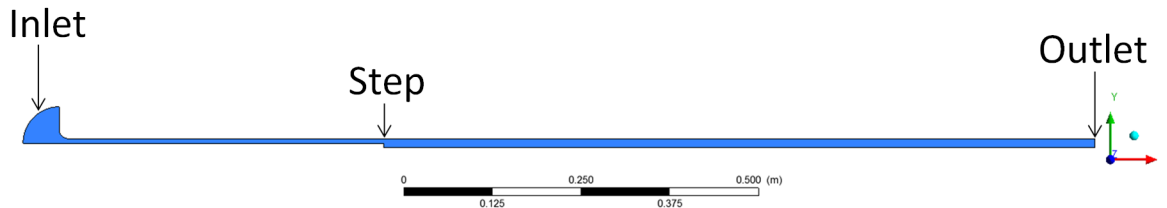
Figure 5.13: Water Channel CFD Geometry

With the outer geometry created, it is now necessary to divide the interior volume into a mesh. Unlike most FEM modeling,which can be used easily with unstructured meshes, CFD analyses require a more uniform type of mesh. The uniformity helps to reduce the propagation of discretization error through the control volume. Additionally, there is a large variety of scales acting in fluid motion, especially in turbulent flow problems. Since the smaller scales are most important near the wall, this is where the mesh needs to be the smallest. In order to resolve these small scales, the mesh size perpendicular to the wall (y direction) should have a size of $y^+ \leq 1$. This also constrains the mesh size parallel to the wall (x direction), since the aspect ratio of each cell should not be too large. The mesh in the center of the channel do not have to be as small as at the wall. So, to minimize the number of cells, the cell size in the y direction was inflated from the bottom wall to the center and deflated from the center to the top wall, using a hyperbolic tangent distribution. This distribution is also used to decrease the mesh size in the x direction approaching the step location and expanding the mesh moving downstream from the step. This is needed in order to resolve the scales on the vertical wall that defines the step.

In order to determine if the mesh resolution is sufficient to capture all of the flow details, three meshes were used. Using the CFD meshing software Gridgen, three meshes were created so they are systematically refined by a factor of two. The finest mesh has a mesh size of g. The second mesh has a mesh which is $2g$ and the coarsest mesh is $4g$. This refinement

can be used not only to determine whether the mesh is fine enough, but can be used to verify the order of accuracy of the code being used. Figure 5.14 shows the comparison between these three meshes around the step location.

(a) h4   (b) h2   (c) h1
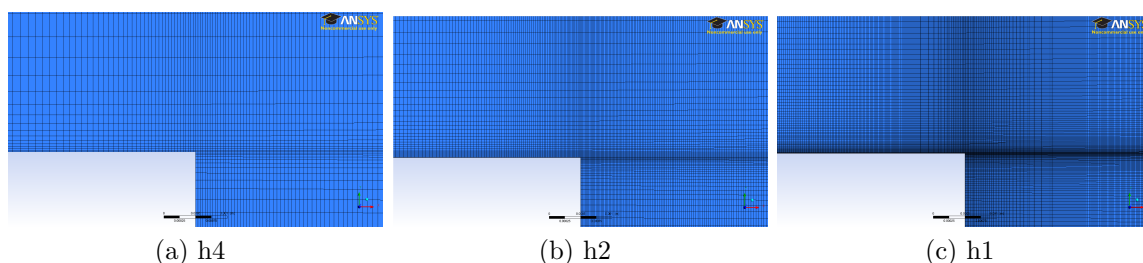
Figure 5.14: Water Channel Mesh Size Comparison

5.5.2 Discretization Method, Turbulence Model, and Boundary Conditions

ANSYS Fluent allows for a large range of discretization methods to be used, since this is largely dependent on the flow type. Since this application is with water at relatively low flow speeds, a pressure-based solver was used. Even though the flow around the step is a transient phenomenon, due to its turbulent nature, a steady state solution will suffice in determining the bulk flow properties in this area and greatly simplifies the analysis. A second-order upwind method was used for all spatial discretization and the pressure-velocity coupling was performed using the SIMPLE scheme. In order to provide more accurate results, the calculations were performed using double precision. The relaxation factors were kept at Fluent's default values. The entire problem was initialized from the inlet using a standard initialization relative to the cell zone.

The turbulence model used was the Menter's shear stress transport (SST) model. This is a two-equation model which combines the k-omega model, which is used in the inner boundary layer, and the k-epsilon model, which is used in the outer region and outside the boundary layer. A few problems are known about using Menter's SST model. The first is that it will over-predict the shear stress in an adverse pressure gradient if the length scales are not small enough. The second is that a low-Reynolds-number modification is needed for near wall calculations. With proper meshing and the addition of the low-Reynolds-number corrections, which is available in Fluent, both of these problems are mitigated.

The boundary conditions for this CFD model are fairly simple. All of the walls were defined as stationary, with a no-slip condition. The wall roughness was left at its default values,

with a roughness height of zero meters and a roughness constant of 0.5. The only additional variable needed was the thermal conditions of the wall, which the wall temperature was set to 300 K with zero heat generation. The outflow boundary was set as a pressure outlet, since the exit of the channel vents to atmospheric conditions. The gage pressure at the outlet was thus set to zero Pa. The turbulence and temperature of the backflow must also be specified at this boundary. The turbulence was specified using the intensity and length scale at 0.2 and 0.0001 m respectively. The temperature of the backflow was set to 300 K. Since there should be no backflow at the channel exit, these values are irrelevant. The last boundary that needs to be considered is the inflow. This, similar to the outflow, was defined as a pressure inlet. Since the true inlet pressure was not known in the experimental set up, there is no way of directly matching a specific flow speed. In order to estimate what this value should be, the pressure was calculated based on the height of the water tower. This gives an inlet gage total pressure of 10,000 Pa. The initial gage pressure was set to zero and a direction specification method of normal to the boundary is used. One again the turbulence intensity and length scale are specified at 0.1 and 0.0001 m and the total temperature of the fluid is set to 300 K.

5.5.3   CFD Results

After the analysis was set up, it was run until convergence. The three meshes were run until all normalized residuals were at or below 10^{-12}. The residuals are normalized on residuals from using the initial conditions. Once the analysis was run to convergence, the solutions were analysed. In order to determine the accuracy of these solutions, the results were compared to both the pressure and the LDV measurements in the channel. While they did not match exactly, due to the inlet pressure conditions not matching, they were close enough to get an understanding of the flow.

The two main pieces of information that can be compared are the pressure and shear forces on the wall. Figures 5.15 and 5.16 show these two values for the upper and lower channel wall boundaries for all three mesh levels.

Figure 5.16 shows that two distinct sections of constant wall shear form in the locations expected. The large jump in pressure and wall shear signifies the location of the step. It can be seen that the section after the step matches well for all three mesh sizes, but there are some discrepancies in the results upstream of the step. The bulk of these discrepancies are seen in the coarsest grid, $g4$. This is due to the mesh not being small enough to resolve the smaller scales.

The pressure and wall shear measurements for the three grids can then be compared to the two experimental analyses.

(a) Top Wall (b) Bottom Wall
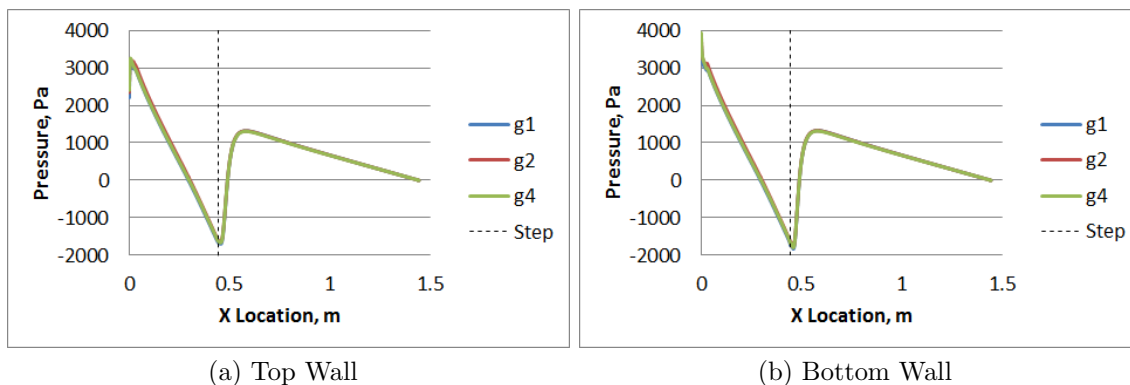
Figure 5.15: CFD Wall Pressure Results

(a) Top Wall (b) Bottom Wall
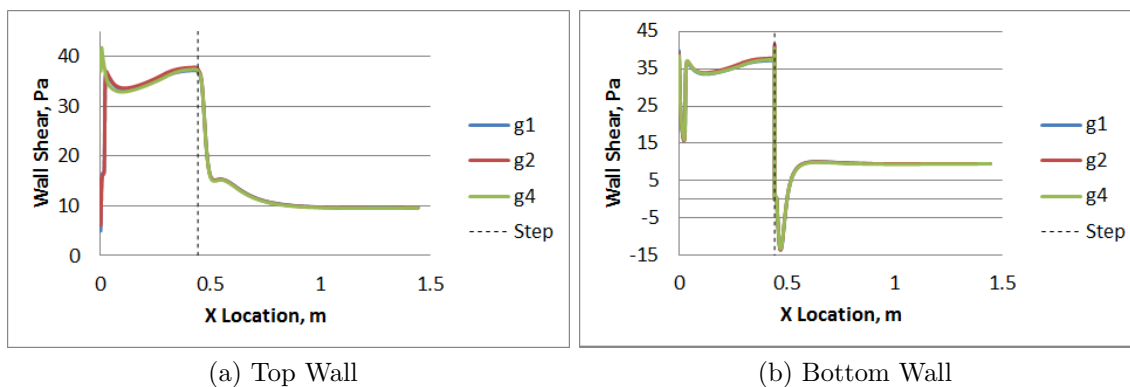
Figure 5.16: CFD Wall Shear Results
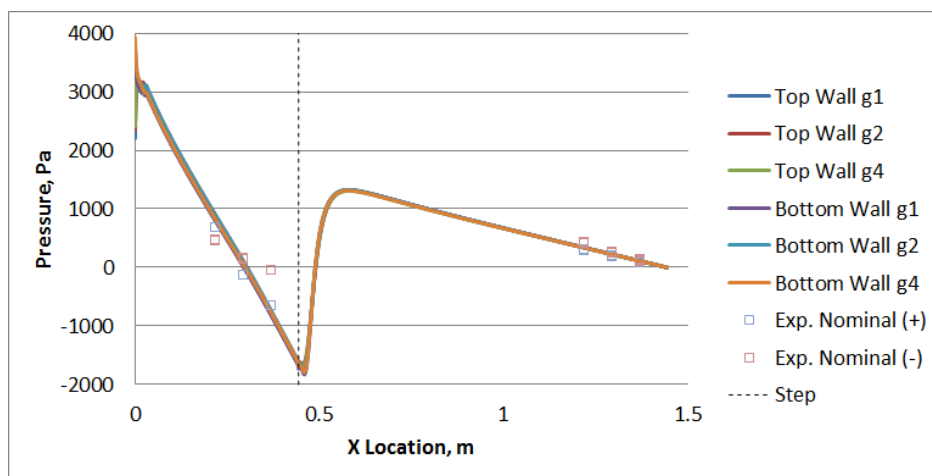
Figure 5.17: CFD Pressure Results Compared to Manometer Measurements
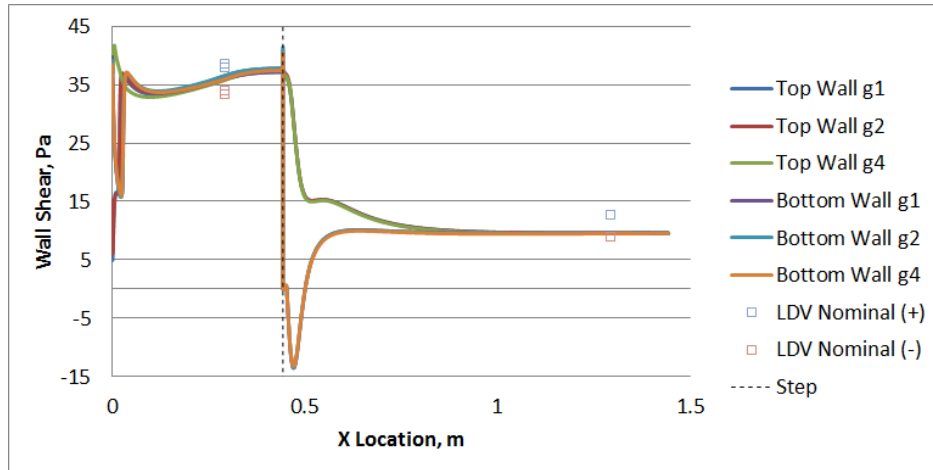
Figure 5.18: CFD Wall Shear Results Compared to LDV Measurements

Figure 5.17 combines the upper and lower surface results and adds the pressure measurements made using the manometers as a comparison. Figure 5.18 also combines the upper and lower surface results and adds the shear calculations made using the LDV results. It can be seen that the nominal flow from the CFD analysis is somewhere between the two settings that are used in the water channel experiments. Since the results match well with the experimental data, we can draw some conclusions from the CFD results. One important result is the shear level just downstream of the step at the two measurement locations. The magnitude of the wall shear can be found to be -6.52 and 5.25 Pa at Locations 4 and 5, respectively, from the $g1$ grid. In order to get a better look at the flow, Figure 5.19 shows the velocity contour plot of the flow near the step.

Looking closely at the tabular data from the finest grid results, the reattachment point can be found to be 57.25 mm downstream of the step. One common way to represent this reattachment is normalized against the step height, which gives a $\frac{X_R}{h} = 9.02$. This is consistent with the findings of Papadopoulos [11], shown in Figure 5.20, which shows a $\frac{X_R}{h}$ of approximately 8.9 at an aspect ratio of 20 and a Re of 26200.

(a) X Velocity
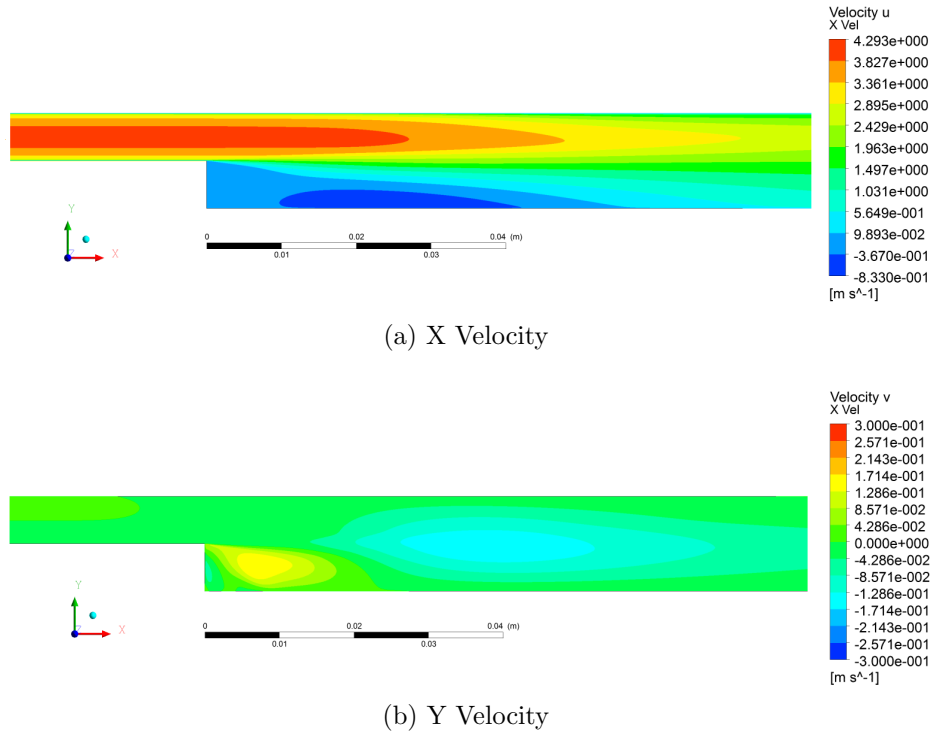
(b) Y Velocity

Figure 5.19: CFD Velocity Results near the Step
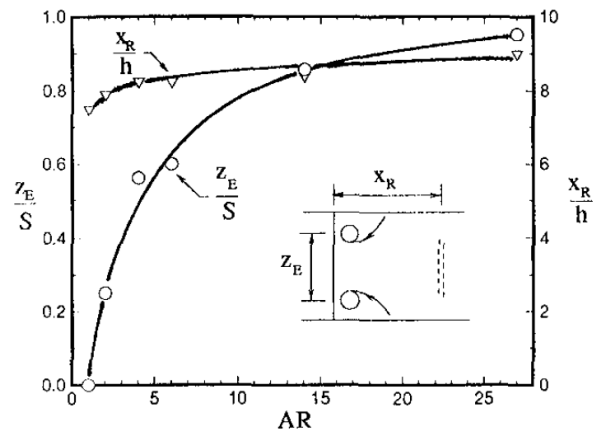
Figure 5.20: Aspect Ratio Dependence of Reattachment Length and Primary Eddy Separation Distance, Papadopoulos [11]

Chapter 6

Experimental Sensor Results

6.1   Overview

Two sensors were created in the double loop configuration of the latest sensor design, see Figures 3.7 and 6.3. These sensors were made for low shear, 1-10 Pa applications, utilizing the additional loop to increase the sensor's output. The sensors were put through a series of tests to determine how effective they were at measuring wall shear forces.

The sensors were first calibrated using the low shear section of the water channel. The calibration run sequence consists of an initial startup of the water channel, which takes approximately a minute, followed by two to four minutes at each flow level and a minute between each flow level to allow stabilization of the water level in the water tower. The channel is then stopped and the water tower is left to drain for an additional minute until the flow stops. This test is repeated three additional times, with around a minute down time between runs. The whole sequence is visualized for a typical water channel calibration run in Figure 6.1. From this time response data, a few details are immediately obvious. The first is the decrease in resistance of the sensor. This is due to the orientation of the sensor in the water channel. The sensors are arranged so that they are in compression. This is done to prevent the leads from interfering with the flow, putting them downstream of the sensing area. It is also done because there have been debonding problems at the lead locations when the leads are upstream of the sensing area. Having the leads downstream resolves both of these issues. It can also be seen that the sensor does not return to the initial resistance at the end of each run. Additionally, there is a slight drift in the resistance between each run.

The sensors were then tested in the NASA 20x28 inch Shear Flow Control Tunnel, shown in Figure 6.2. This tunnel is an open-circuit, low-speed (150 ft/sec max) atmospheric facility with low free stream turbulence due to a series of screens and large contraction ratio settling
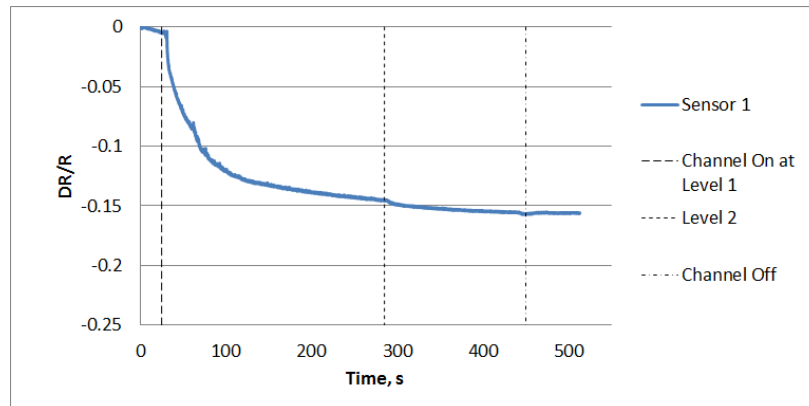
Figure 6.1: Typical Sensor Design 3B, Water Channel Calibration Time Variation

chamber. The test section is 15 feet long and has a cross section 20 inches high by 28 inches wide with an adjustable upper wall to control the pressure gradient over the long test section. These runs were conducted similarly to the calibration runs. After the tunnel was switched on, the sensor was allowed to dwell at each flow velocity level for approximately two minutes. Between each flow velocity level, the tunnel took around 45 seconds to stabilize at the next setting.
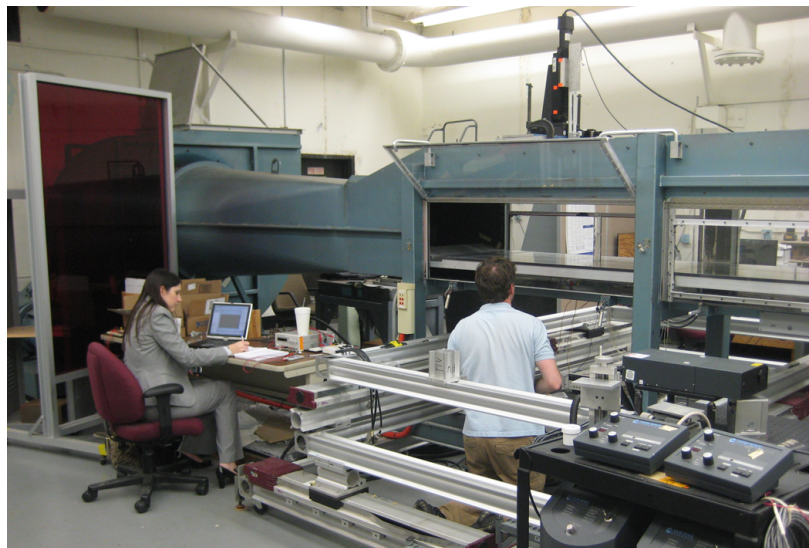
Figure 6.2: NASA LaRC 20 x 28 Inch Shear Flow Control Tunnel

After these tests were completed, the sensors were modified to reduce the bump in the oil film area due to slight overfilling. The sensors were then recalibrated in the low shear section of the water channel and tested in the backflow and reattachment locations behind the water channel step. These results are then compared to the sensor response predictions calculated

using the Comsol model.

6.2 Wind Tunnel Results

The first calibration was accomplished with sensors that had a bump of about 0.5 mm tall in the center of the oil film area. This bump can be seen in Figure 6.3. This bump causes the sensor to respond not only to wall shear forces, but to pressures acting parallel to the wall. These additional forces increase the response of the sensor at a given shear level. Figure 6.4
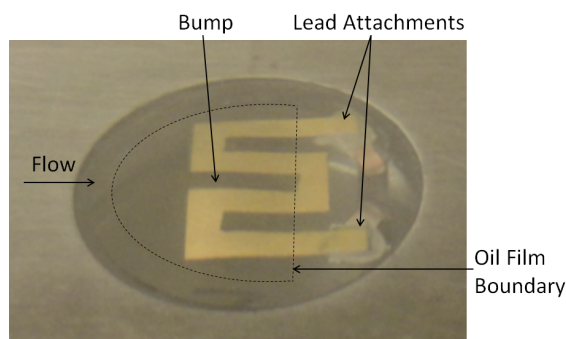
Figure 6.3: Design 3B Skin Friction Sensor, Showing Oil Film Area Bump

shows the time response of the sensors during the calibration tests. Once again, the sensors do not return to their true zero resistance and drift over the course of the four tests. It has been observed from all previous testing that the sensors will eventually return to the true zero resistance, but this requires a long period of time. It is, therefore, assumed that the starting resistance of the first test is the true zero shear resistance. Every subsequent test will be compared to this initial resistance value when calculating $\frac{\Delta R}{R}$. A drift in the sensor response occurs during each test and in the downtime between tests, seen as the difference in end values between tests. This drift was quantified using the difference in the end values between the first test and each subsequent test. This value was then subtracted from the entire relevant test. Since each test has the same duration, this results in the sensor response for each run collapsing onto the first run. The end result of this process can be seen in Figure 6.4b.

In order to produce a calibration curve for the sensors, the sensor's response at each shear level must be calculated. This was done using the average $\frac{\Delta R}{R}$ value at each shear level, which are then plotted. It can be seen that the sensors did not behave in a linear manner. This was due to the bump in the oil film area. At low shear levels, the sensor area is compressed. As the shear level increases, the material buckles slightly, causing a decrease in the compressive strain, reducing the sensor response. This buckling occurs at the higher shear level, thus the higher shear level calibration point is ignored. A least-square fit approximation through the

(a) Without Drift Correction   (b) With Drift Correction
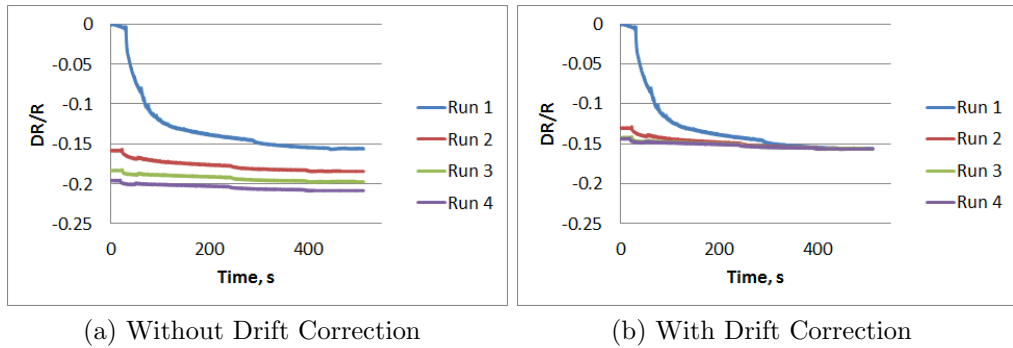
Figure 6.4: Calibration Results for the Sensors with the Bump

remaining low shear data provides the calibration curve for the sensor. Having more data points at the very low shear levels would make this calibration more accurate, but the sensors were modified to fix the bump before additional calibration testing could be completed.

(a) Sensor 1 Response   (b) Sensor 2 Response

(c) Sensor 1 Calibration Curve   (d) Sensor 2 Calibration Curve
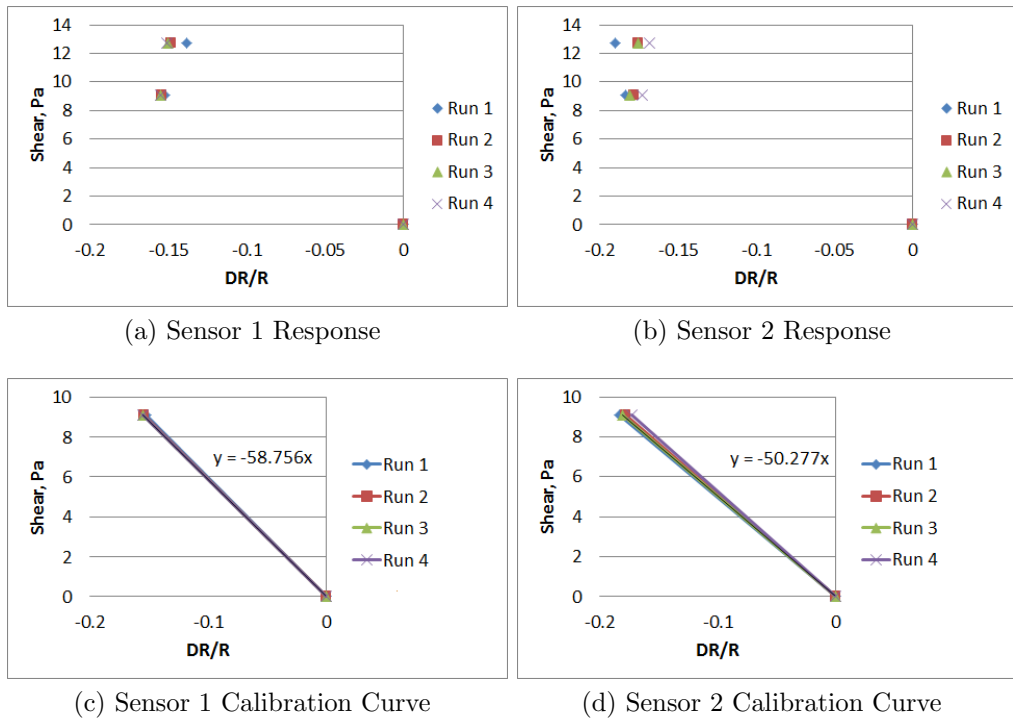
Figure 6.5: Calibration Results for the Sensors with the Bump

With the calibration curve for the sensors, they could then be used to measure the wall shear in the NASA 20x28 inch Shear Flow Control Tunnel. The sensors were mounted on the floor of the test section as seen in Figure 6.6. Four sensors were tested, with the two furthest

away from the camera in the Design 3B configuration.
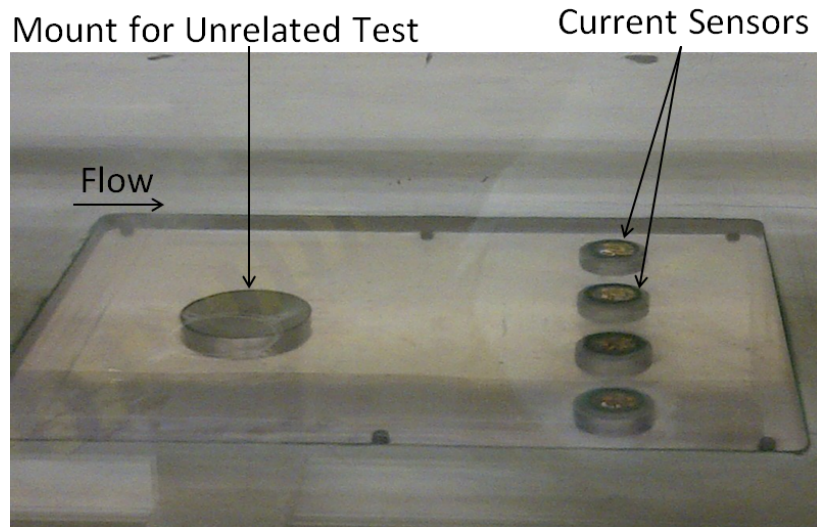
Figure 6.6: NASA 20x28 inch Shear Flow Control Tunnel Test Section, showing Sensors Mounted in the Floor Plate

Two tests were run with the sensors, but unfortunately technical problems prevented the second test data from being recorded. The time response of the sensors plotted along with the tunnel flow velocity is shown in Figure 6.7. From this figure it can be seen, from the
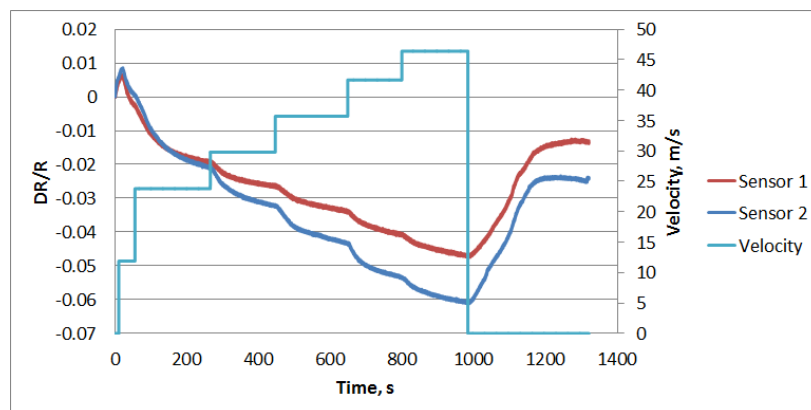
Figure 6.7: Sensor Response and Tunnel Velocity vs Time

decrease in resistance with increasing velocity, that the sensor is once again arranged such that the sensing area is being compressed. This also shows that the sensors exhibit a strange behavior at the beginning of the test. The initial rise in resistance of the sensor is most likely due to loads releasing that were applied to the sensor during the mounting process. Another observation from this data, and the calibration data, relates to the time response

of the sensors. The sensors responded quickly to each flow velocity change, but the settling time to reach a steady state was rather long. The sensor response was, thus, averaged over each velocity level near the end of each flow velocity setting. These values were then used in combination with the calibration curve to determine the shear forces in the tunnel at each velocity level. In order to determine if these measurements were accurate, a separate test was conducted in the tunnel using a proven method, in this case a Preston tube, as a comparison. Figure 6.8 shows how the two sensors compare with the Preston tube measurements.
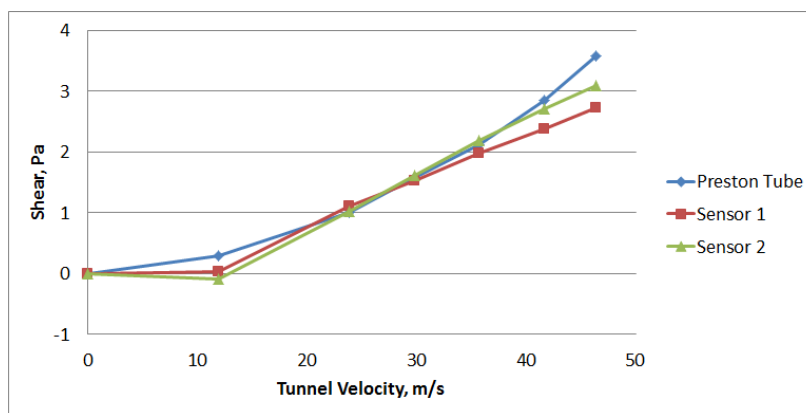
Figure 6.8: Comparison between the Sensor Results and the Preston Tube Measurements

This shows very good agreement between the sensor measurements and the Preston tube measurements. These results could be improved with more calibration settings at the lower shear levels and with longer dwell times at each flow velocity setting during the wind tunnel test.

6.3 Water Channel Step Flow Results

After the NASA wind tunnel test was completed, the sensors were modified to eliminate the bump in the oil film area. This was done using a hypodermic needle to remove a small amount of oil, the hole left by the needle was closed using a solvent which reacts with the Metal Rubber polymer and closes the hole. The resulting sensors can be seen in Figure 6.9. Since this procedure altered the sensor, a new calibration had to be conducted in order to determine the sensors' sensitivity to shear. Once again, this calibration was performed using the low shear section of the water channel.

Figure 6.10 shows the time response of the sensors during the calibration runs. The same data reduction techniques were used on this data as was used to reduce the results from the previous calibration. In order to produce a calibration curve, the sensor response at each shear level is calculated from this time response. As seen in Figure 6.11, the sensors show a
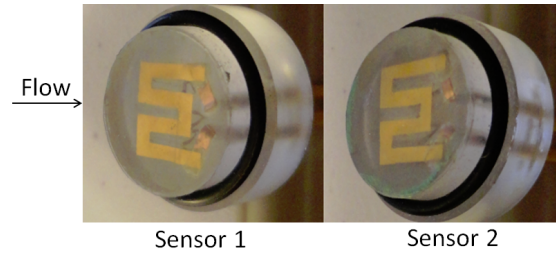
Figure 6.9: Sensors After Bump Reduction Procedure

slightly non-linear behavior. The sensors do respond in a more predictable way, increasing with increasing shear, unlike the unmodified sensors with the surface bump. The calibration curve through this data can then be used to predict the shear in another application.
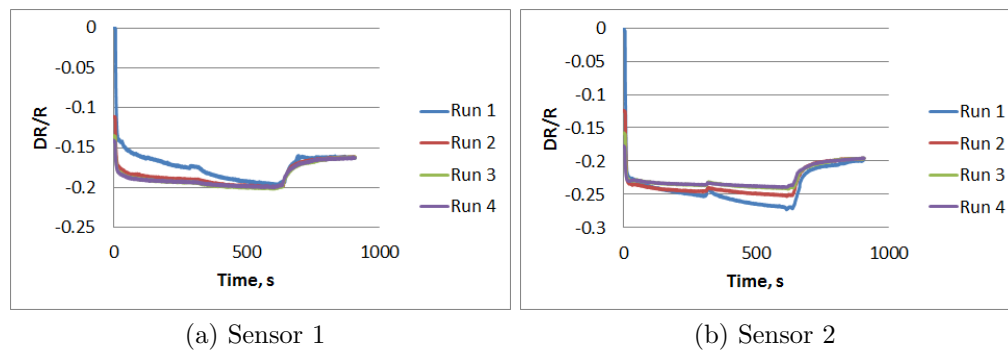
(a) Sensor 1

(b) Sensor 2

Figure 6.10: Calibration Time Response for the Sensors without the Bump

The sensors were tested in both Locations 4 and 5 in the water channel, shown in Figure 5.2 in the complex flow region just downstream of the step. From the LDV and CFD results it was found that there should be recirculation at Location 4 and the flow is just passed the reattachment point at Location 5. The sensors were tested using the same methods that were used in the calibration runs, arranged with the leads downstream of the sensing area. This means that backflow in the recirculation area will lead to a positive change in resistance. The time response of the sensors in these two locations are shown in Figures 6.12 and 6.13. It is immediately obvious, from the increased noise, that the flow at these two points is more turbulent than in the calibration location. It is also apparent that the flow at Location 4 shows backflow, as expected. Three of the four test points at Location 5 show the flow is reattached, with Sensor 1 showing slight backflow at the second flow level.

The response at each flow level was then calculated, using the average $\frac{\Delta R}{R}$ at each flow level. These response levels could then be used to determine the wall shear at each flow level using the calibration curves. The results of this analysis are shown in Figure 6.14 plotted against

(a) Sensor 1 Response

(b) Sensor 2 Response

(c) Sensor 1 Calibration Curve

(d) Sensor 2 Calibration Curve
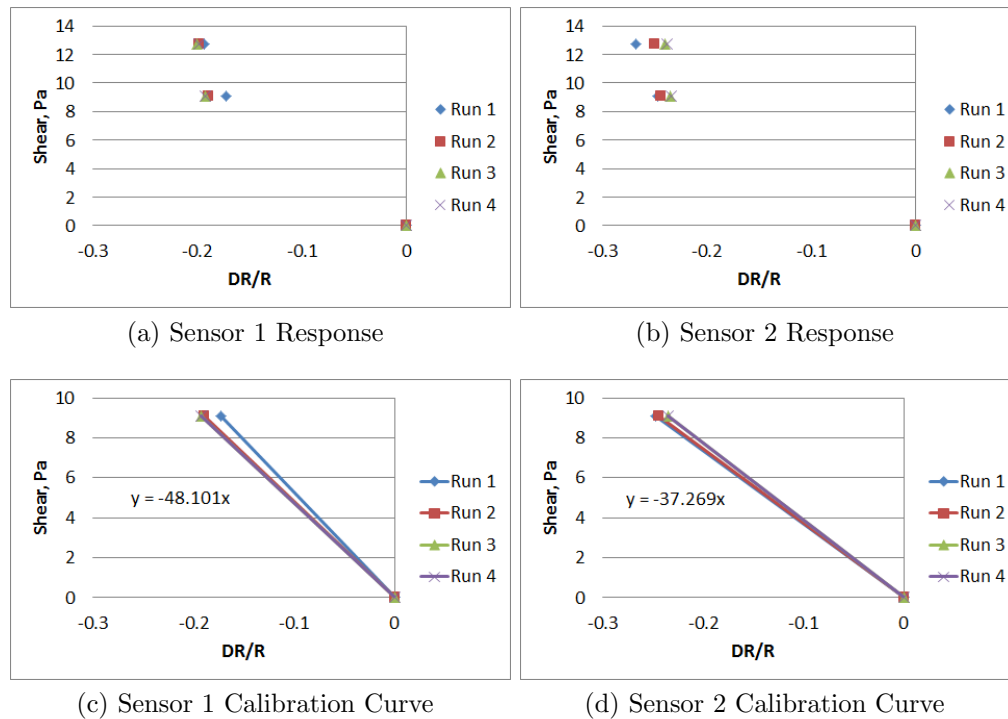
Figure 6.11: Calibration Results for the Sensors without the Bump
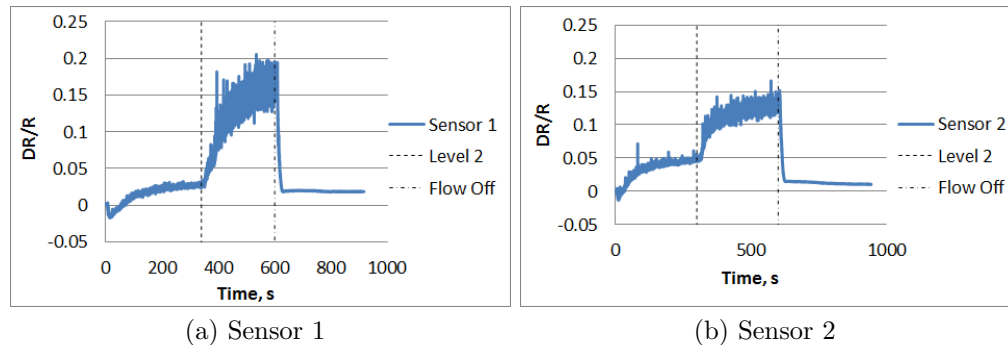
(a) Sensor 1

(b) Sensor 2

Figure 6.12: Water Channel Location 4 Time Response

the CFD estimated shear levels downstream of the step. This comparison shows that, while the sensors do not match up exactly with the CFD predicted levels, they are close and correctly predict the flow directionality. The differences between the sensor results and CFD results could be due to a number of factors.One of the largest factors is that downstream of the step, there is a fairly strong pressure gradient. This pressure gradient can not only have adverse affects on the CFD results, but it will also be shown in the next section to have a detrimental affect on the sensor behavior. Another factor is the relatively large sensor size compared with the characteristic flow scales in the turbulent flow. The sensor effectively

averages these scales over the sensing area.

(a) Sensor 1　　　　　　　　　　　(b) Sensor 2
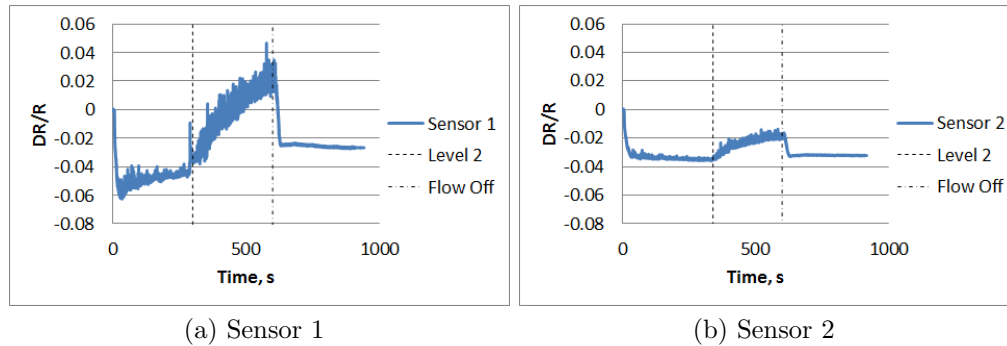
Figure 6.13: Water Channel Location 5 Time Response
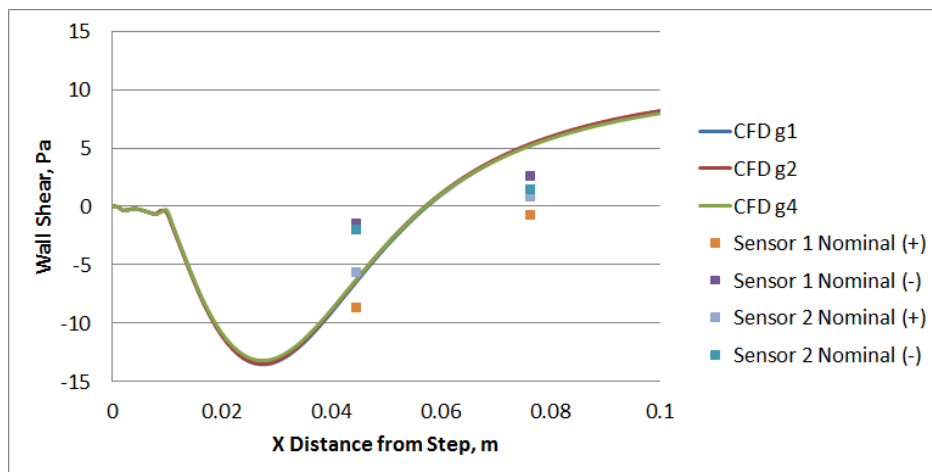
Figure 6.14: Water Channel Step Sensor Results Compared to the CFD Flow Results

6.4 Modeling Results

In addition to experimental results completed for the Design 3A Double Loop Sensors, a model of this sensor was also created. This sensor model used all of the same settings and geometry, except for the sensor pattern, which is just modified to match the experimental sensors. One slight change that was made in the model was the small gap between the oil film area and the section between the two loops, as seen in Figure 6.15, which was made to eliminate an error that occurred when the two lines were coincident. The mesh was again created using the built-in physics-controlled meshing sequence. Due to the increased complexity of this design, the mesh consisted of 42251 cells, an increase from the Design 3A

Single Loop configuration.

(a) Top   (b) Bottom
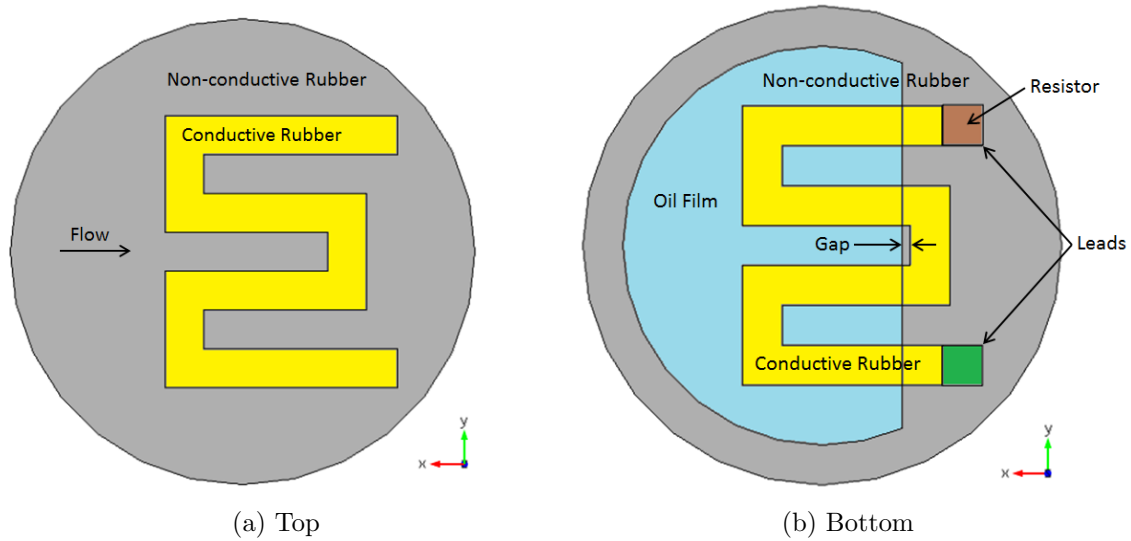
Figure 6.15: Sensor Design 3B Double Loop Model Geometry
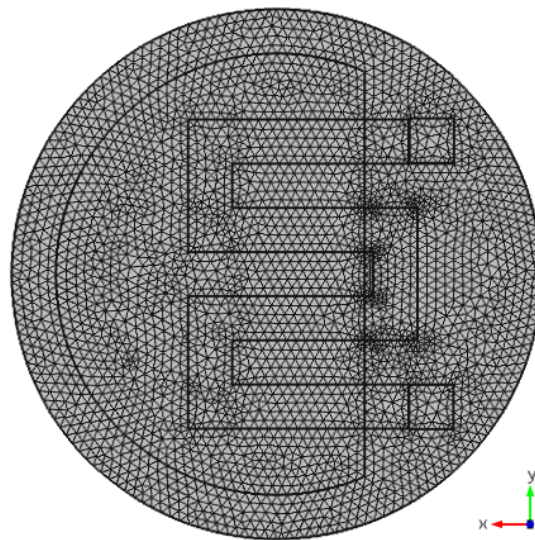
Figure 6.16: Sensor Design 3B Double Loop Model Mesh

The loads applied to this model were varied from $0\ Pa$ to $14\ Pa$, slightly higher than the maximum shear used in the calibration experiments. The output of the sensor was then converted into the normalized resistance change and compared to the results from the sensors without the bump. These results are shown in Figure 6.17. This shows that the model

predicts the general sensor response, but by a factor of 100 less. This factor is very large, taking into consideration that the tensile test validation experiments, seen in Section 4.3, matched extremely well at the strain levels that should be present on the sensors in these experiments. The added complexity of the flow over the sensor, and the fact that only a shear over the sensor was modeled, is the most likely cause for this discrepancy.
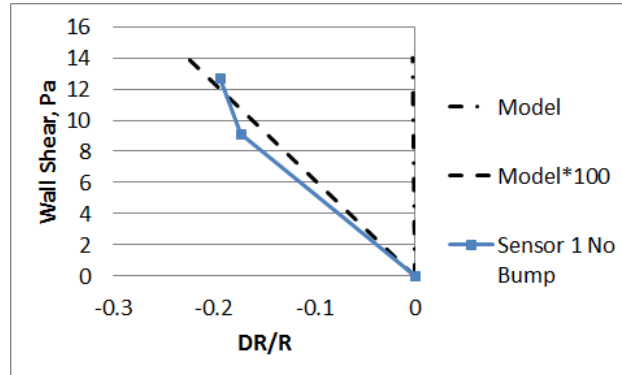
Figure 6.17: Sensor Design 3B Double Loop Model Results Compared with Experimental Results

One factor that may come into play is the normal pressure loading on the surface of the sensor. In order to test this, the same model was run, but with an added 250 Pa normal pressure. The resulting change in response was minimal, with only a $0.38\% FS$ shift in the response of the model. There is not only a normal pressure on the sensor in the experiment, but a pressure gradient as well. Since the normal pressure alone had little effect on the response, it may be the pressure gradient that causes the difference. The pressure gradient at the downstream fully-developed section of the water channel is about $2000 \frac{Pa}{m}$ with an average normal pressure magnitude, again, around 250 Pa. A comparison with the pressure gradient, normal pressure, and original results are shown in Figure 6.18. This shows that the pressure gradient does indeed have a non-negligible affect on the sensor output, a $5.3\% FS$ shift in the response, where this effect decreases the output of the sensor at a given shear level.

The only other explanation for the discrepancy in the modeled and water channel experimental sensor response is a non-trivial interaction between the flow and the sensor. The most likely explanation is that some small distortion of the sensor surface over the oil film remained, even at the low shear levels. This distortion is not taken into account in the computer model and would require a coupled fluid-structure boundary condition on the top surface of the sensor to model this interaction. Streamwise pressure due to surface irregularities are much larger than viscous shear at high Reynolds number conditions. Due to this, the streamwise pressure is used in many indirect methods, like the sublayer fence, to measure skin friction. In fact, this type of sensor was attempted in a parallel Metal Rubber
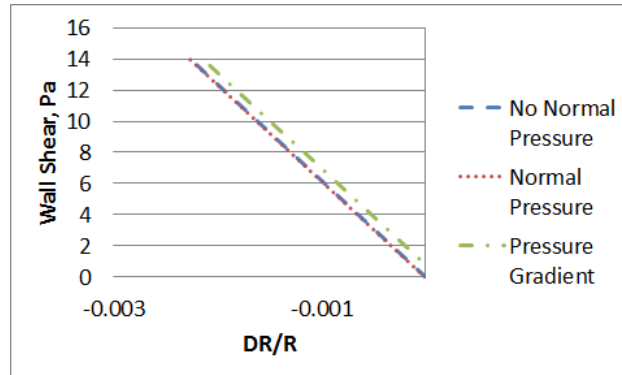
Figure 6.18: Sensor Design 3 Double Loop Model Pressure Effects

sensor design, with moderate success. For this study it is preferred that the sensors not have this perturbance, in order to prevent flow disturbance.

There are a number of possibilities for why the model does not predict the sensor response, as this is an idealized computer model attempting to model a non-ideal sensor. Even though the model does not fully predict the response of the as-built sensors, it is a good tool for determining the effects of different factors on the sensor response.

6.5   Application of Sensor Computer Model

In order to show the effectiveness of the computer model for use in determining the effects of interfering factors, the model was used to predict how the sensor would respond to the flow over an airfoil. The particular airfoil used for this analysis was the NACA 4412, shown in Figure 6.19, with a chord length $c = 1m$ for simplicity. Since one of the limiting factors for skin friction sensors is a strong pressure gradient, this airfoil was tested at an angle of attack of 8.5 degrees, which is just prior to stall. A flow speed of 30 $\frac{m}{s}$, at sea level conditions, was used in order to ensure turbulent flow over the majority of the airfoil. The computer model was used to test the sensor design at two locations, Location A at an $\frac{x}{c} = 0.25$ and Location B at $\frac{x}{c} = 0.75$.

The Reynolds numbers, based on the x location, for these two locations are $Re_x = 478000$ and $Re_x = 1430000$ for Location A and B, respectively. In order to determine the skin friction and pressure over the surface of the airfoil at these conditions, three numerical methods were used. The Vortex Panel method was used in order to determine the inviscid flow velocity and pressure coefficient around the airfoil at a specified angle of attack. This velocity profile was then used with the Thwaites-Walz method until turbulent transition and Moses' Method after transition to determine the boundary layer and thus the skin friction on the airfoil surface[4]. The results from this analysis for the NACA 4412 airfoil are shown in
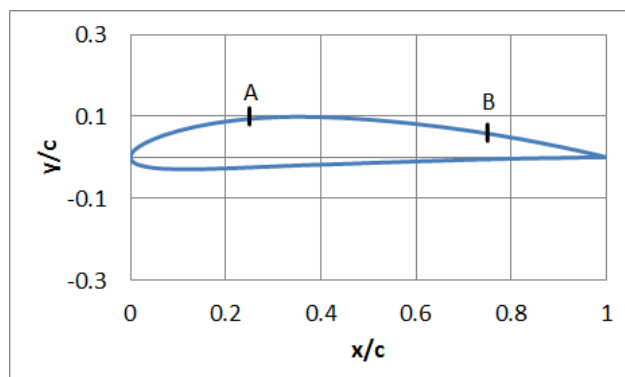
Figure 6.19: NACA 4412 Airfoil Shape, Showing Test Locations

Figure 6.20. The pressure gradient and shear values at the two test locations were $1524\frac{Pa}{m}$
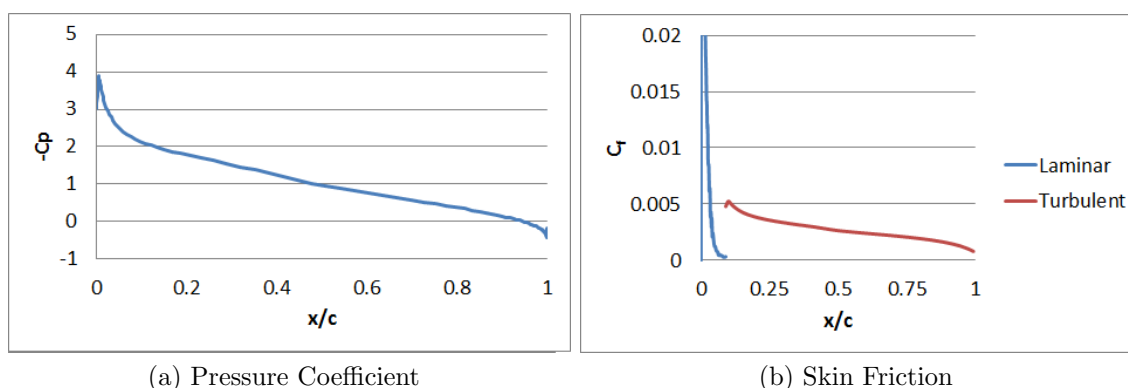
(a) Pressure Coefficient

(b) Skin Friction

Figure 6.20: NACA 4412 Pressure Coefficient and Skin Friction Over the Top Surface

and $5.5Pa$ at Location A and $1085\frac{Pa}{m}$ and $1.8Pa$ at Location B. The simulation was also run without the surface pressure, in order to determine how this pressure affects the sensor response. Figure 6.21 shows the sensor response for these four conditions. It can be seen that there is a non-negligible difference between the response with a pressure gradient and without a pressure gradient. At Location A, there is a 14.1% difference between the two conditions and at Location B, there is a 25.7% difference between the two conditions. This shows that the sensor is sensitive to large pressure gradients. Some thoughts on how to deal with this effect are discussed in Section 8.

This study demonstrates the utility of having a computer simulation. Various conditions, which may not be possible experimentally, can be tested easily to determine how each condition affects the sensor.
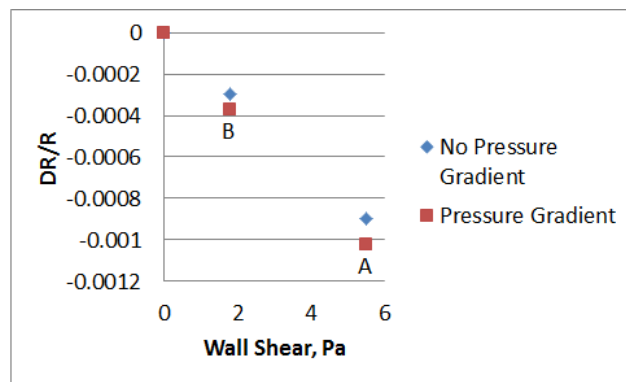
Figure 6.21: NACA 4412 Computer Model Sensor Response

Chapter 7

Conclusions

The overarching goal of this research was to conceive, model, design, build, and test a skin friction sensor using a nanoparticle infused thin film for low skin friction level applications. In doing so, the thin film material Metal Rubber, created by Nanosonic, Inc. was mechanically and electrically characterized to understand its usage in a skin friction sensor. It was found that this material not only had the mechanical properties required for use in a flexible thin film sensor, but was also piezoresistive, due to the polymer being infused with gold nanoparticles. This allows the material to measure its own strain field, when patterned correctly.

At first, this pattern was designed using a trial and error type method, which did not produce many working sensors. The majority of these early sensors were built so that any positive resistance change was negated along the sensing area with a negative resistance change. In order to determine why these sensors were not responding well, a computer model of the material was needed. The material was modeled in the multiphysics program Comsol. This model not only provided the mechanical response of the material, but the electrical response as well. This model was verified against tensile test experimental results to confirm it was working as it should. It was then validated against two additional tensile tests, where a sensor shaped conductive area was patterned in either the constant strain area or in a variable strain area of the dogbone shaped specimen. These tests again confirmed that the model was able to predict the response of the material to a carefully controlled strain load. This model allowed for a skin friction sensor design patterned to respond to the strains that produce the greatest response. The resulting sensor design was built and calibrated in a fully-developed water channel.

Two calibration water channels were used over the course of this research. The original water channel only allowed for wall shear forces on the order of 35 Pa to 45 Pa and only accepted sensors that were 44.45 mm in diameter, which is large for a skin friction sensor. The water

channel was modified not only to accept smaller sensors, with a 19.05 mm diameter, but to have two fully-developed regions. The first region retained the wall shear forces on the order of 40 Pa; the second region was designed to have wall shear forces on the order of 10 Pa. This allowed for sensors to be calibrated in either regime. The updated calibration rig also included a sudden step between the two regions, allowing for wall shear measurements in a complex, well-studied flow. The water channel was characterized using a number of methods. To understand the overall flow behavior in the channel, LDV measurements were made at both calibration locations and just downstream of the step. A CFD model of the channel was also developed, compared against the LDV results, and used to characterize the step flow behavior. Pressure measurements were made during each calibration run to determine the wall shear at each flow level during sensor calibration.

Two sensors were calibrated in the lower shear region of the water channel and later tested in the NASA 20x28 inch Shear Flow Control Tunnel. The results from the sensors were found to match well with independently measured wall shear in this facility. There was one problem with these two sensors, which was the presence of a small bump in the oil film area, due to too much oil being injected during the manufacturing process. This extra oil was manually removed and the sensors were recalibrated in the water channel. The recalibrated sensors were then tested in the step flow of the water channel. The results from this test were compared with CFD wall shear predictions. The results matched well at one point and were slightly lower than the predicted shear at the other. The discrepancy between the measured shear and the predicted shear is most likely due to limitations of the CFD model and the sensors in a pressure gradient.

The measured sensor response in the calibration rig was also compared to the computer model predicted response and was found to be off by a factor of 100. This discrepancy is due to the complex interaction of the sensor with the flow, which the model is not built to handle. In particular, it is suspected that small surface irregularities remained after the excess oil was removed. While it does not provide a good estimate of the absolute response, the computer model is a useful tool for determining the sensor sensitivity to different sources of error. It was found, in the fully-developed water channel, that a normal pressure has little effect on the sensor response, but a pressure gradient can cause errors of around 5%. The sensor computer model was also applied to an airfoil near stall to see the effect of larger pressure gradients on the sensor response. The computer model showed that the sensor is more sensitive to these larger pressure gradients.

Utilizing the thin, flexible, piezoresistive material Metal Rubber, multiple sensors were designed, manufactured, and tested successfully in both the calibration flows and in useful flow applications with wall shear forces up to 15 Pa. This clearly demonstrates the potential of this material for skin friction sensors. Further work is needed in the sensor modeling, design, and fabrication in order to produce sensors for routine use.

Chapter 8

Recommendations for Future Work

While this research has provided the base for the design and application of nanoparticle infused thin film skin friction sensors, there is still plenty of work that can and should be done in order to further improve the design. The sensors tested in this research are based mostly on the mechanical model results and have not been optimized fully using the sensor computer model. It would be worthwhile to build a sensor using an optimized design from the modeling tool created in this research. In addition, the computer model itself could be updated to include more of the sensor physics, such as viscoelastic effects. Introducing some of the non-linearities in the material properties would allow for more accurate simulations at higher shear levels. With additional material testing, fewer assumptions in the electrical properties could be made, which would also increase the accuracy of this model.

In order to make the sensors more accurate, the calibration water channel needs additional modifications. It was seen in this research that while the updated water channel can provide more shear levels in the two fully-developed regions, these are not enough to fully calibrate the sensors. There is a gap in the low shear range, between 0 Pa and 9 Pa, where no measurements can be made due to bubbles forming in the channel. Modification of the water tower to reduce the splashing of the recirculating water should eliminate the presence of these bubbles, possibly making these lower shear levels attainable. These levels would only require verification that the flow is fully-developed in order to use them.

The sensors made in this research are for testing in very controlled environments. Using this sensor in a real world application, on an aircraft wing or on the hull of a boat, would require a more robust sensor. Improved fabrication methods are needed to produce sensors that do not have the lead and oil film area issues of the current sensors. These sensors were also made with mostly one-dimensional measurements in mind, which are usually not present in real world applications. By patterning two sensors perpendicular, or three with 120° between each sensor on the same oil film area, similar to some strain gage designs, it would be able

to measure directionality. The other main issue that would appear in these applications is temperature fluctuations. These sensors are fairly sensitive to temperature variations, but with the addition of an additional sensor pattern which only experiences the thermal loads, these effects could be cancelled with the correct circuit.

One other major factor that needs to be improved is the time response of the sensors. They not only have a long settling time, but also have a slight creep. The settling time prevents these sensors from being used in unsteady flows, since it would not be able to adjust to the fluctuating flow. The creep adds uncertainty to the results, since it is a path dependent phenomenon. One way to deal with the settling time involves modeling the time response and calculating a time constant for the sensor response. This would allow the user to determine the steady state response from unsettled response data. Another method to reduce the time constant of the sensor response is to reduce the Metal Rubber Young's modulus. However, manufacturing difficulties arise when the modulus is reduced, as the material loses durability.

From the computer model, it was determined that the sensor is sensitive to pressure gradient effects. This can be mitigated in a couple ways. The first is the inclusion of static pressure sensors in upstream and downstream of the sensing area to measure the pressure gradient. This information could be used with the computer model to compensate for the effect. Using the fully-developed water channel, the sensor could also be calibrated for this effect. The last option is to design a sensor that is not as sensitive to the pressure gradient effects.

These modifications to the sensor model, the calibration channel, and the sensor itself would make for a more viable sensor design for use in real world applications. Since the groundwork for this type of skin friction sensor has been laid out, this research is being prepared for publication in open literature.

Appendix A

Error and Uncertainty Analysis

In order to determine how well these sensors will perform in different applications, it is important to determine the errors and uncertainties prone to the sensor. Some of the major uncertainties associated with skin friction sensors include manufacturing and geometry uncertainty, calibration uncertainty, alignment uncertainty, thermal uncertainty and random errors during data acquisition. This section looks to break down these individual error sources and document their effects on the sensor response.

A.1   Material Properties Uncertainty

In order to understand the accuracy of the Metal Rubber material properties, the uncertainties in the tensile test results were analysed. For both the modulus and piezoresistance tensile tests, a linear best fit line was used to determine the slope of the corresponding data. Since this is an approximation of the data, an R-squared value is given to determine how closely the data matches the data.

For the Young's Modulus calculation, the best fit line approximates the data with greater than 98% confidence. This shows that, at the strain levels expected in this analysis, a linear approximation of the stress-strain data in the linear elastic region is valid. The linear regression used in the two resistance tensile tests show 98% and 78% confidence in the X-Resistance and Y-Resistance tests, respectively. There is more uncertainty in the Y-Resistance test results due to the increased difficulty of this test, which produced data that was more scattered on the smaller strain scales seen in this analysis. Using a jitter method, the overall uncertainty in the piezoresistive coefficients are $\pm 2.64\%$ and $\pm 4.82\%$ for the m_{11} and m_{12} coefficients, respectively.

A.2   Sensor Manufacturing and Geometry Uncertainty

One source of uncertainty in these sensors relates to the sensor geometry and manufacturing process. Due to the complexity of the material chemical make-up, each batch of Metal Rubber is slightly different. Two sensors made from different batches of material will respond differently. The only way to account for this is to calibrate each sensor. In addition to the manufacturing of the material itself, fabricating the sensor provides additional uncertainties. Alignment of the sensor pattern with the oil film area can contribute to sensor alignment problems when installing the sensor. The outside edge of the sensor can be rough, due to difficulty in cutting the sensor shape from the bulk Metal Rubber sheet. One of the biggest sources of uncertainty in the sensors deals with the filling of the oil film area. Too little oil and the sensing area will rub on the mount and have a convex shape, but too much oil and a bump will form. This will induce a non-linear response from the sensor at the higher shear levels. Figure A.1 shows the difference in response of Sensors 1 and 2 with and without an overfilled oil film area. The magnitude of this difference in the linear low-shear level is almost 30%. This difference does not directly translate into error in the results, due to the calibration process.

(a) Sensor 1   (b) Sensor 2
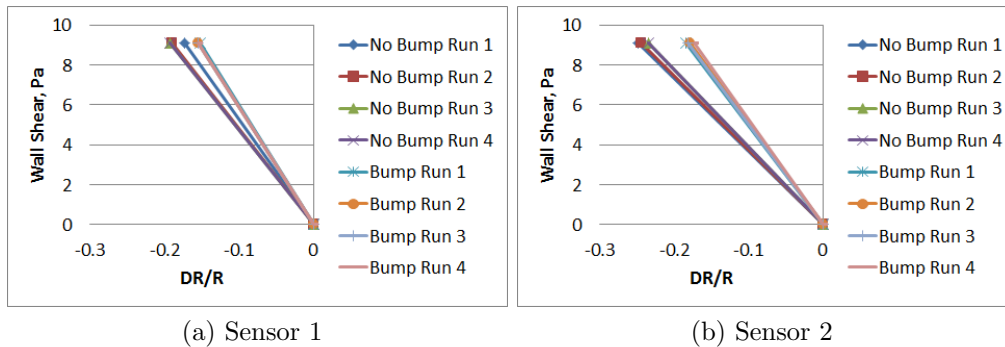
Figure A.1: Sensor Calibration Results Comparison for the Sensors With and Without an Overfilled Oil Film Area

A.3   Calibration Uncertainty

During the calibration process there are a few sources of uncertainty. The first is the alignment of the sensor in the water channel. Since the sensors do not have a tab for "perfect" alignment, though even this would still suffer from uncertainty in the manufacturing process, the sensors are aligned visually. There are a number of straight surfaces that act as cues for this alignment, so it is possible for the sensor to be misaligned, conservatively, by up to $\pm 5°$. This leads to the sensor seeing a 0.5% decrease in the shear force parallel to the measurement direction.

Another form of uncertainty in the calibration procedure stems from the wall shear calculations made from the pressure measurements in the fully-developed flow. This uncertainty can be directly calculated using the individual measurement uncertainties and Equation 5.6. This is done by taking the partial derivative of Equation 5.6 with respect to each term and taking the root mean square of the results. This results in Equation A.1:

$$\tau_w \, Uncertainty = \sqrt{(\delta dp \frac{h}{dx})^2 + (\delta dx \frac{hdp}{dx^2})^2 + (\delta h \frac{dp}{dx})^2} \qquad (A.1)$$

where $\delta()$ is the uncertainty of the variable, dp pressure difference, dx is the distance between pressure sensors, and h is the half height of the channel. Using this equation, the uncertainty in the wall shear calculations made from the pressure measurements is $\pm 2.4\%$.

The last form of uncertainty in the calibration procedure, and in general when making measurements with the sensor, is bias error due to the data acquisition system. This uncertainty is eliminated by utilizing the same data acquisition system during both calibration and testing, since this error will be the same in both tests.

A.4   Thermal Uncertainty

During all of the testing in this research, there has been almost no problem with thermal loads on the sensor. This is due, mainly, to the use of a water calibration channel. Water is exceedingly good at maintaining its temperature, due to its high specific heat capacity. This means that over the course of the tests, there is little to no thermal load on the sensor, except if the sensor was heated or cooled prior to the testing. This difference in temperature is quickly negated after even a single calibration test, which is one reason why up to four calibration tests are run per sensor.

In order to determine what the effect of a thermal load on the sensor would be, a simple test was conducted. This test consisted of a single Metal Rubber sample, with the dimensions 5mm x 30mm, subjected to know temperature variations. A 4-wire resistance measurement method was used to avoid errors caused by wire resistance. Figure A.2 shows the sensor configuration.

The thermal chamber on the TA.XTplus was used to provide the temperature control, with a range of $-60°C$ to $200°C$ $\pm 0.05°C$. The test was conducted so that the material was subject to each temperature level for 15 minutes, to allow it to stabilize. The results from this experiment are shown in Figure A.3. From this data, the uncertainty of the sensor response can be found to be $0.15 \frac{\%}{°C}$
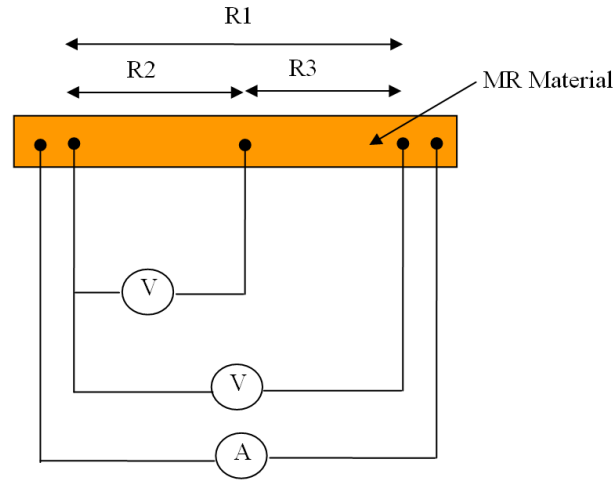
Figure A.2: Metal Rubber Temperature Dependence Measurement Method
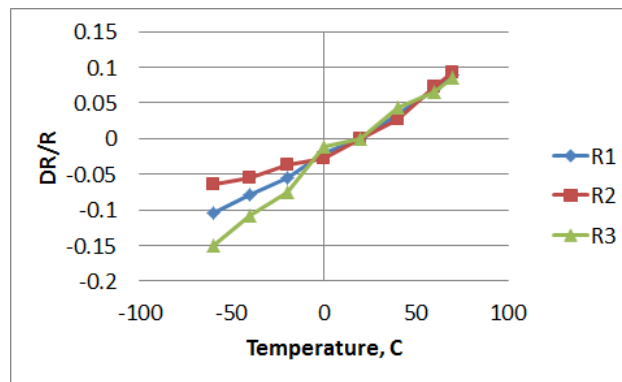
Figure A.3: Metal Rubber Temperature Dependence Measurement Results

A.5 Uncertainty Overview

It can be seen from this uncertainty analysis that the biggest contribution to the uncertainty of the sensor response comes from uncertainties in the manufacturing process. slight changes in the sensor geometry can have large effects on the output. These uncertainties are somewhat mitigated through the calibration process, but can still prove to be problematic. The other major source of uncertainty in the sensor response can come from thermal effects. A few degrees of thermal load on the sensor can begin to have a large effect on the response, this effect can be accounted for, however, if the the temperature of the sensor is monitored. The best example of the overall uncertainty in these sensors was shown in the NASA wind tunnel tests. It was seen that the sensors had an error of 23.5% at the highest shear flow velocity level, but was within 10% at almost every other flow velocity setting.

Appendix B

Bibliography

[1] W. Froude. Experiments on the surface-friction experienced by a plane moving through water. *42nd British Association Report*, 42:118–125, 1872.

[2] W. Nitsche, C. Haberland, and R. Thunker. Comparative investigations of the friction drag measuring techniques in experimental aerodynamics. *ICAS*, 84-2.4.1(14th ICAS Congress), 1984.

[3] K. G. Winter. An outline of the techniques available for the measurement of skin friction in turbulent boundary layers. *Progress in Aerospace Science*, 18:1–57, 1977.

[4] J.A. Schetz. *Boundary Layer Analysis*. Prentice Hall, Englewood Cliffs, NJ, 1993.

[5] C. Brucker, J. Spatz, and W. Schroder. Feasability study of wall shear stress imaging using microstructured surfaces with flexible micropillars. *Experiments in Fluids*, 39:464–474, 2005.

[6] A. Omid and J. Soria. A film-based wall shear stress sensor for wall-bounded turbulent flows. *Experimental Fluids*, 41:137–147, 2011.

[7] S.B. Pope. *Turbulent Flows*. Cambridge University Press, Cambridge, U.K., 2000.

[8] K.T. Lowe. *Design and application of a novel Laser-Doppler Velocimeter for turbulence structural measurements in turbulent boundary layers*. Dissertation in partial fulfillment for the degree of doctor of philosophy in aerospace engineering, Virginia Polytechnic Institute and State University, Blacksburg, VA, September 2006.

[9] D.B. Spalding. A single formula for the law of the wall. In ASME, editor, *Conference on Iternational Developement in Heat Transfer*, number 2, pages 439–446, Boulder, Co., 1961.

[10] R.L. Simpson. Aspects of turbulent boundary-layer separation. *Progress in Aerospace Sciences*, 32(5):457–521, 1996.

[11] G. Papadopoulos, M.V. Otugen, and G.C. Vradis. The three-dimensional separated flow structure in a variable aspect ratio sudden expansion duct. *AIAA*, 31, 1993.

[12] J. J. Bertin. *Aerodynamics for Engineers*. Prentice Hall, Upper Saddle River, NJ, 4th edition, 2002.

[13] J.A. Schetz. Direct measurement of skin friction in complex flows (invited). *AIAA*, (2010-0044), 2010.

[14] J. A. Schetz. Skin friction measurements in complex turbulent flows using direct methods. *Engineering Turbulence Modelling and Experiments*, 6:421–430, 2005.

[15] J. W. Naughton and M. Sheplak. Modern developements in shear-stress measurement. *Progress in Aerospace Sciences*, 38:515–570, 2002.

[16] N. I. Konstantinov and G. L. Dragnysh. The measurement of friction stress on a surface. *Energomashinostroenie*, pages 191–200, 1955.

[17] F. H. Clauser. Turbulent boundary, layers in adverse pressure gradients. *Journal of Aeronautical Science*, 2(21):91–108, 1954.

[18] H.E. Albracht, M. Borys, N. Damaschke, and C. Tropea. Laser doppler and phase doppler measurement techniques. 2003.

[19] L.H. Tanner and L.G. Blows. A study of the motion of oil films on surfaces in air flow, with application to the measurement of skin friction. *Journal of Physics E: Scientific Instruments*, 9:194–202, 1976.

[20] E. Klein and A. Margozzi. Exploratory investigation on the measurement of skin friction by means of liquid crystals. In *11th Israel Annual Conf. On Aviation and Astronautics*, Tel Aviv, March 1969.

[21] S. Dhawan. Direct measurements of skin friction. *NACA Report*, (1121), 1951.

[22] J. M. Allen. Systematic study of error sources in supersonic skin-friction balance measurements. Technical Report NASA-TN-D-8291, NASA, 1976.

[23] M. Raffel, C. E. Willert, S. T. Wereley, and J. Kompenhans. *Particle Image Velocimetry*. Springer-Verlag Berlin Heidelberg, 2nd edition, 2007.

[24] Inc. Nanosonic. Metal rubber™, http://www.nanosonic.com.

[25] Texture Technologies Corp. Ta.xtplus texture analyzer, http://texturetechnologies.com.

[26] E. O. Doebelin. *Measurement Systems: Application and Design*. The McGraw-Hill Companies, Inc., 5th edition, 2004.

[27] COMSOL. Comsol multiphysics, http://www.comsol.com/.

[28] H. Abe and H. Kawamura. Direct numerical simulation of fully developed turbulent channel flow with respect to the reynolds number dependence. *Journal of Fluids Engineering*, 123, June 2001.

[29] F. Anselmet and et al. Axial development of the mean flow in the entrance region of turbulent pipe and duct flows. *C.R. Mecanique*, 337:573–584, 2009.

[30] S. A. Magill. Study of a direct measuring skin friction gage with rubber compounds for damping. Thesis in partial fulfillment for the degree of master of science in aerospace engineering, Virginia Polytechnic and State University, Blacksburg, VA, 1999.

[31] K.T. Lowe and R.L. Simpson. An advanced laser-doppler velocimeter for full-vector particle position and velocity measurements. *Measurement Science and Technology*, 20:1–16, 2009.

[32] ANSYS Inc. Ansys 13.0, http://www.ansys.com.

[33] Pointwise Inc. Gridgen, http://www.pointwise.com.

[34] Thorlabs. Nrt100, http://thorlabs.com.

[35] Hamamatsu Corporation. Pmt r4124, http://sales.hamamatsu.com.

[36] A.V. Boiko and V.I. Kornilov. *Hot-wire anemometer measurement of local skin friction coefficient*. PhD thesis, Khristianovich Institute of Theoretical and Applied Mechanics SB RAS, Novosibirsk, Russia, December 2009.

[37] R. D. Bowersox and et al. Technique for direct measurement of skin friction in high enthalpy impulsive scramjet flowfields. *AIAA*, 33(7), July 1995.

[38] P. Bradshaw and N. Gregory. The determination of local turbulent skin friction from observations in the viscous sublayer. *Aeronautical Research Council Reports and Memoranda*, (3202), 1959.

[39] O. Desgeorges and et al. Multiple hot-film sensor array calibration and skin friction measurement. *Experiments in Fluids*, 32:37–43, 2002.

[40] D.J. DeTurris. *A Technique for Direct Measurement of Skin Friction in Supersonic Combustion Flow*. PhD thesis, Virginia Polytechnic Institute and State University, Blacksburg, VA, November 1992.

[41] H.H. Fernholz and et al. New developments and applications of skin-friction measuring techniques. *Measurement Science Technology*, 7(1396), 1996.

[42] J. H. Haritonidis. The measurement of wall shear stress. *Advanced Fluid Mechanics*, 1989.

[43] F. Haselbach and W. Nitsche. Calibration of single-surface hot films and in-line hot-film arrays in laminar or turbulent flows. *Measurement Science Technology*, 7(1428), 1996.

[44] M.R. Head and I. Rechenberg. The preston tube as a means of measuring skin friction. *Journal of Fluid Mechanics*, 14, March 1862.

[45] Y. Li. *Side-Implanted Piezoresistive Shear Stress Sensor for Turbulent Boundary Layer Measurement*. Dissertation in partial fulfillment for the degree of doctor of philosophy in aerospace engineering, University of Florida, 2008.

[46] M. Novean. *Direct Measurement of Skin Friction in Complex Supersonic Flows*. Dissertation in partial fulfillment for the degree of doctor of philosophy in aerospace engineering, Virginia Polytechnic and State University, Blacksburg, VA, March 1996.

[47] M. W. Orr. *Design, Analysis, and Initial Testing of a Fiber-Optic Shear Gage for 3D, High-Temperature Flows*. Dissertation in partial fulfillment for the degree of doctor of philosophy in aerospace engineering, Virginia Polytechnic and State University, Blacksburg, VA, November 2004.

[48] W.J. Pulliam. *Development of Fiber Optic Aerodynamic Sensors for High Reynolds Number Supersonic Flows*. Dissertation in partial fulfillment for the degree of doctor of philosophy in aerospace engineering, Virginia Polytechnic and State University, Blacksburg, VA, November 2000.

[49] D.C. Reda and M.C. Wilder. Shear-sensitive liquid crystal coating method applied through transparent test surfaces. *Journal of Fluid Mechanics*, 39(1):195–197, 2001.

[50] M.M. Reischman and W.G. Tiederman. Laser-doppler anemometer measurements in drag-reducing channel flows. *Journal of Fluid Mechanics*, 70(2):369–392, 2975.

[51] A. Remington. A study of non-fluid damped skin friction measurements for transonic flight. Thesis in partial fulfillment for the degree of master of science in aerospace engineering, Virginia Polytechnic and State University, Blacksburg, VA, July 1999.

[52] A.J. Rolling. *Design of Gages for Direct Skin Friction Measurements in Complex Turbulent Flows with Shock Impingement Compensation*. Dissertation in partial fulfillment for the degree of doctor of philosophy in aerospace engineering, Virginia Polytechnic and State University, Blacksburg, VA, July 2007.

[53] A.K. Sang, A.J. Rolling, and J.A. Schetz. A novel skin friction sensor for hypersonic flow. *AIAA*, (2006-3837), 2006.

[54] T. B. Smith. *Development and Ground Testing of Direct Measuring Skin Friction Gages for High Enthalpy Supersonic Flight Tests*. Dissertation in partial fulfillment for the degree of doctor of philosophy in aerospace engineering, Virginia Polytechnic and State University, Blacksburg, VA, September 2001.

[55] D.B. DeGraaff and J.K. Eaton. Reynolds-number scaling of the flat-plate turbulent boundary layer. *Journal of Fluid Mechanics*, 2000.

[56] F. Durst, H. Kikura, I. Lekakis, J. Jovanovic, and Q. Ye. Wall shear stress determination from near-wall mean velocity data in turbulent pipe and channel flows. *Experiments in Fluids*, 20:417–428, 1996.